Lehrstuhl für Verfahrenstechnik des industriellen Umweltschutzes

Doctoral Thesis

The Influence of Nitrogen on Catalytic Methanation

Ana Roza Medved, univ.dipl.inž.kem.inž

December 2020

MONTANUNIVERSITÄT LEOBEN
www.unileoben.ac.at

EIDESSTATTLICHE ERKLÄRUNG

I declare on oath that I wrote this thesis independently, did not use other than the specified sources and aids, and did not otherwise use any unauthorized aids.

I declare that I have read, understood, and complied with the guidelines of the senate of the Montanuniversität Leoben for "Good Scientific Practice".

Furthermore, I declare that the electronic and printed version of the submitted thesis are identical, both, formally and with regard to content.

Datum 02.12.2020

Signature Author
Ana Roza Medved

Vorgelegt von:

Ana Roza Medved

m01620685

ACKNOWLEDGEMENTS

There have been many people over the past years that supported me and contributed to this work, to whom I would like to express my gratitude.

The biggest thank you goes to Univ.Prof.Dipl-Ing.Dr.-Ing Markus Lehner, for the opportunity to join his research team, for guidance, all of the constructive discussions and astoundingly knowledgeable feedback and ideas over the past years. Last but not least, for the much-needed motivation, patience and providing a pleasant working environment, such that I believe is not that easy to find anywhere else. Thank you!

To my colleague companion at the beginning of the journey, DI Dr. mont. Philipp Biegger. Without your introduction to methanation, experimental test plant, patient counselling and all the “baschteln” times, this work would not have been possible.

Over the years expanding “Team Methan“ group, for the knowledge exchange and helpful scientific and non-scientific discussions, along with the resulting solutions: DI Andreas Krammer, DI Martin Peham, DI Katrin Salbrechter and DI Philipp Wolf-Zöllner as well as all the students that have contributed with their work, either through their practical work or master´s and bachelor´s theses.

The great time at the “Lehrstuhl für Verfahrenstechnik des industriellen Umweltschutzes” is attributed to all my colleagues. I am grateful for all the work- and non-work-related times, reliability and willingness to help. Special thanks go to Mark Read for all the help and indulgence, in the context of within or in front of the “Technikum” debates.

The research project “RenewableSteelGases” funded by the Austrian research funding agency FFG, was the basis of the present thesis. To all project partners from the companies voestalpine Stahl GmbH; voestalpine Stahl Donawitz GmbH; K1-MET GmbH; TU Wien, Institut für Verfahrenstechnik, Umwelttechnik und Technische Biowissenschaften (ICEBE) and Energieinstitut at JKU Linz, thank you for the good cooperation.

Finally, to my family back home as well as my Graz family for the unconditional support and love over the years. Thank you Mama for your guidance and Ata for all the helpful advice and strength (and for finally accepting that I am not a chemist). Thank you to my sisters Meta and Mia as well as Oma and Deda for all the cheers! Thank you to all my friends for great times and much needed distractions during this period.

And my Tom, without you I would not have made it.

Thank you! Vielen Dank! Hvala!

Abstract

The Influence of Nitrogen on Catalytic Methanation

Steel production is largely carried out via blast furnace/basic oxygen route (integrated steel plant), where the by-product gases from the different production units are one of the largest CO_2 contributors to the global GHG emissions. In order to achieve the climate goals set in the Paris agreement, the integration of renewable energies and reduction of the CO_2 emissions is one of the key points that have to be implemented in the existing steel production infrastructure. Blast furnace gas (BFG) and basic oxygen furnace gas (BOFG) are, due to their high CO, CO_2 and N_2 content and poor heating value, showing great potential as a carbon source for the implementation of Power-to-Gas (PtG) technology.

In the present thesis, the behaviour of the methanation of BFG and BOFG gas at different operating conditions was investigated. The influence of N_2 on the methanation process was determined, as well as GHSV, pressure and the H_2-surplus variations to achieve the complete conversion of carbon oxides were carried out. The parameter variations and the N_2 influence were explored on a complementary basis using the simulation tool Aspen Plus®. The simulation results are compared with experimental data.

Experimental tests have shown that the complete conversion of the CO and CO_2 in BFG and BOFG is achieved with and without the presence of N_2 in the feed gas, with already upwards of 5% H_2 surplus for both process gases, with three-stage methanation. High pressures resulted in higher CO_x conversion, whereas the increase of the GHSV inhibited the conversion on account of the residence time. The N_2 in the feed gas therefore only has a significant influence on the higher heating value of the CH_4-rich product gas, resulting in the case of BFG in 19.2–19.8 MJ m^{-3} (ratio H_2/CO_x 1.09–1), and for BOFG in 26.7–28.8 MJ m^{-3} (ratio H_2/CO_x 1.09–1). However, the enriched BFG and BOFG, when utilised in the integrated steel plant as lean gases, contribute to a decrease in natural gas and electrical energy demand.

Simulation results were obtained in Aspen Plus®, with application of kinetic reactors as well as Gibbs reactors, and compared with the experimental data. From the three chosen kinetic models from the open literature, the kinetic model from Rönsch predicted the trend of the conversions and yields correctly, with and without present N_2 as well as over a wide temperature range between 250-650°C. The slight deviations of the CO_2 concentration between the Rönsch kinetic model and experimental data led to the assumption of thermodynamic limitations in the three reactors, connected in series. The assumption was confirmed by the application of Gibbs reactors. It is shown that an equilibrium based on the reactor outlet temperature described the experimental data well, thus confirming the thermodynamically dominated reactions in the used polytropic reactors.

Kurzfassung

Der Einfluss von Stickstoff auf die katalytische Methanisierung

Die Stahlproduktion erfolgt größtenteils über die Hochofen/Konverter Route (integriertes Hüttenwerk), in der die Nebenproduktgase aus den verschiedenen Produktionseinheiten einen der größten CO_2-Beiträge zu den globalen Treibhausgasemissionen leisten. Für die Erreichung der im Pariser Abkommen festgelegten Klimaziele, ist die Integration erneuerbarer Energien und die Reduzierung der CO_2-Emissionen in der bestehenden Stahlproduktionsinfrastruktur ein notwendiger Aspekt. Gichtgas (GG) und Tiegelgas (TG) weisen aufgrund ihres hohen CO-, CO_2- und N_2-Gehalts und geringen Heizwerts ein großes Potenzial als Kohlenstoffquelle für die Implementierung der Power-to-Gas Technologie (PtG) auf.

In der vorliegenden Arbeit wurde das Verhalten der Methanisierung von GG und TG unter verschiedenen Betriebsbedingungen untersucht. Der Einfluss von N_2 auf den Methanisierungsprozess wurde erforscht. Weiters wurden Raumgeschwindigkeit (GHSV)-, Druck- und H_2-Überschuss-Variationen durchgeführt, um einen vollständigen Umsatz von CO_x zu erreichen. Die Parametervariationen und der N_2-Einfluss wurden komplementär mit dem Simulationsprogramm Aspen Plus® untersucht und die Simulationsergebnisse mit experimentellen Daten verglichen.

Experimentelle Ergebnisse haben gezeigt, dass die vollständige Umwandlung von CO und CO_2 in GG und TG mit und ohne N_2 im Eduktgas erreicht wird. Beide Prozessgase konnten bei einem H_2-Überschuss bis zu 5% in einer dreistufigen Methanisierung umgesetzt werden. Hohe Drücke führten zu einer höheren CO_x-Umwandlung, während der Anstieg der GHSV die Umwandlung aufgrund einer kürzeren Verweilzeit hemmte. Daher hat N_2 im Eduktgas nur einen signifikanten Einfluss auf den Brennwert des CH_4-reichen Produktgases, was im Fall von GG zu 19,2–19,8 MJ m^{-3} (Verhältnis H_2/CO_x 1,09–1) und für TG in 26,7–28,8 MJ m^{-3} (Verhältnis H_2/CO_x 1,09–1) führt. Angereicherte GG und TG verringern, bei einer Verwendung als Schwachgase im integrierten Hüttenwerk jedoch den Bedarf an Erdgas und elektrischer Energie.

Die Simulationsergebnisse wurden in Aspen Plus® unter Anwendung von kinetischen Reaktoren sowie Gibbs-Reaktoren generiert und mit den experimentellen Daten verglichen. Von den drei ausgewählten kinetischen Modellen aus der Literatur prognostizierte das kinetische Modell von Rönsch den Trend der Umwandlungen und Ausbeuten korrekt, mit und ohne vorhandenem N_2, sowie über einen weiten Temperaturbereich zwischen 250-650°C. Die geringfügigen Abweichungen der CO_2-Konzentration zwischen dem kinetischen Modell und experimentellen Daten führten zur Annahme thermodynamischer Limitierungen in den drei in Reihe geschalteten Reaktoren. Diese Annahme wurde durch die Anwendung von

Gibbs-Reaktoren bestätigt. Es wird gezeigt, dass ein Gleichgewicht basierend auf der Reaktoraustrittstemperatur die experimentellen Daten korrekt darstellte und somit die thermodynamisch dominierten Reaktionen in den verwendeten polytropen Reaktoren bestätigte.

Contents

Page

1 Introduction

Climate protection and the necessity of reducing man-made greenhouse gas (GHG) emission is one of the greatest challenges that mankind is currently facing and will have to tackle in the decades to come. The average earth´s temperature rise, linked to the emitted GHG emission is shown in a preponderance of evidence among scientists. In the Paris Agreement of December 2015, 197 countries committed to keeping the global temperature rise below 2°C above the pre-industrial level and to make an effort to limit the temperature rise to 1.5°C [1]. In 2016, carbon dioxide (CO_2) represented 74.4% of the world´s GHG, followed by the 17.3% of methane (CH_4), 6.2% nitrous oxide (N_2O) and a smaller amount of fluorinated gases, summing to 49.36 billion tons emissions of CO_2 equivalent (CO_{2eq}) [2].

For industrialised countries, the solution is largely seen as a combination of energy efficiency and abandoning the use of fossil fuels while increasing renewable energy sources. In 2018, the European Commission presented a long-term strategy to reduce GHG emissions with several scenarios to achieve the set goals of 45% GHG emission reduction by 2030 and move towards net-zero GHG emissions by 2050 [3]. Achieving the set goals is only possible as a combination of different approaches; therefore, a set of seven strategic building blocks was proposed:

- maximisation of energy efficiency,
- deployment of renewable energies (with the target of 32% by 2030 by means of electricity or e-fuels such as hydrogen and Power-to-X)
- clean mobility,
- competitive industry and circular economy (recycling of materials),
- development of a smart network infrastructure,
- bio-economy with afforestation and
- tackling the remaining CO_2 -emissions with Carbon Capture and Storage (CCS) [3]

Carbon Capture and Storage or Sequestration (CCS) on depleted oil and gas fields as a proposed technology for the removal of the remaining CO_2 emissions is one option. The CCS consists of three main steps: separation or capture of the CO_2 from the flue gas, followed by its transportation and geological storage. For the separation of CO_2, a number of different physico-chemical based technologies are being developed: some of them already reached a commercial technology readiness level (TRL). These include chemical or physical absorption (e.g. amine scrubbers), adsorption on different materials (e.g. zeolites, activated carbon), gas solid reactions (e.g. carbonate looping with CaO or MgO), cryogenic process, and membrane technology as well as the natural integration of CO_2 (e.g. through photosynthesis with microorganisms, such as algae). [4]

Nevertheless, the problem occurs with the CCS last step, the storage of the CO_2, which has not been accepted in all European countries. The safety concerns and especially strong opposition by the communities towards CO_2 transport pipelines or sequestration basins is

hindering the technology implementation [5,6]. For example, in Austria, geological storage is allowed for research purposes only [7].

In 2018, CO_2 represented 84.5% of the whole of GHG in Austria summing to 79 million tonnes of CO_{2eq}, where the sector energy and industry accounted for 43.4% of the GHG. Although the emissions levels decreased from the year before for 3.7% (3.1 million tonnes of CO_{2eq}), one of the main reasons for the reported change of course was the maintenance and therefore a shut-down of one of the blast furnace in the steel making industry. Despite the overall downward trend recorded after 2005, when Kyoto Protocol entered into force, the increase in its fossil fuel consumption as well as of steel production, due to economic growth and its demands, makes the steel industry one of Austria´s largest GHG emitters. In 2018, it accounted for a total of 14.2% of the GHG emissions. [8,9]

When considering the second strategic block of the European Commission (the deployment of renewable energies), wind and solar energy sources already play an important role in electric power generation. Although the share of the latter compared to the world´s total power generation was low (4.8% for wind and 2.2% for solar power in 2018), there has been an average growth of 22% per annum for wind and 46% per annum for solar energy over the last ten years [10,11]. However, both energy sources are fluctuating and intermittent and have to be balanced to meet the demand at any time. Energy storage of the surplus is one option, by means of transformation of electrical energy into chemical energy by means of gas (Power-to-Gas), liquid fuels (Power-to-Liquid) or chemicals (Power-to-Chemicals) through the utilisation of the residual CO_2 [11].

Primary crude steel production in Europe, but especially in Austria is largely carried out via a blast furnace/basic oxygen (BF/BOF) route, a so-called integrated steel plant. An integrated steel plant is a well established, complex production unit, where interdependent material and energy streams connect various production units. Blast furnace gas (BFG), basic oxygen furnace gas (BOFG) and coke oven gas (COG) with typical gas compositions (Table 1-1) are the by-products of production units.

Table 1-1: Typical gas composition of the three main steel gases [12]

		BFG	COG	BOFG
Parameter	**Unit**			Mean
CO	vol-%	19–27	3.4–5.8	60.9
H_2	vol-%	1–8	36.1–61.7	4.3
CO_2	vol-%	16–26	1.0–5.4	17.2
N_2	vol-%	44–58	1.5–6	15.5
CH_4	vol-%	-	15.7–27	0.1
C_xH_y	vol-%	-	1.4–2.4	
Lower heating value	MJ $m^{-3}_{(STP)}$	2.6–4.0	9.0–19	8.18
Higher heating value*	MJ $m^{-3}_{(STP)}$	2.6–4.4	11–21	8.26

*calculated

They are mainly utilised as energy carriers within the integrated steel plant and cover up to 40% of the energy demand [13], where the remaining part is balanced with electrical power and natural gas. Since the integrated route is a highly developed process, any further optimisations of the existing operating condition for achieving a greater reduction of GHG emission are almost impossible [12].

Nevertheless, the high concentrations of CO_2 and carbon monoxide (CO), but low heating values of BFG and BOFG, due to the high concentration of the present nitrogen (N_2), show great potential for integration of the Power-to-Gas (PtG) technology in an integrated steel plant. Although new technologies for the environmentally friendlier steel production are on the rise (for example direct reduction of the iron ore), the blast furnace/basic oxygen route is a well established process, and the realisation of the new technologies is still a matter of development. Furthermore, the implementation of the new developing technologies requires specific infrastructure and this results in significant investment costs. [14]

2 Motivation

2.1 Purpose of the Research

The economic viability of an overall process can be improved with the avoidance of the intermediate steps, for example, gas separation of the target component for further application. The carbon source for the methanation in the PtG process chain is usually provided by a separation process, which extracts CO_2 from industrial exhaust gases, air etc. Although the CO_2 separation technologies are state-of-the-art, the separation techniques available on the market (even if they provide a high purity of product gas) are highly energy-intensive and therefore costly. [15,16]

To explore the possibility of avoiding the intermediate step of the CO_2 separation from the steel gases (Table 1-1), the main focus in the present work was to determine the influence of the inert components, such as N_2, on the catalytic methanation process. Furthermore, the avoidance of the separation step would also provide an additional carbon source in the form of CO present in the steel gases. As an outcome, the resulting enriched product gas after the methanation, the lean gas, would therefore have the potential to be used directly in the steel production.

2.2 Methodology

The influence of the N_2 as well as varying CO and CO_2 concentrations in the feed gas on the catalytic methanation was explored on a complementary basis using the Aspen Plus® simulation program together with experiments conducted in a laboratory methanation plant.

The experimental work was carried out on a laboratory test plant for catalytic methanation with three fixed-bed reactors connected in series, using a commercial nickel-based bulk catalyst. In varying the test parameters, the focus lay on obtaining the data on the optimal operating conditions, such as exploring the influence of the N_2 on the reaction as well as the flow rate of the feed gas, pressure and variation of the H_2 surplus to achieve a complete conversion of the CO and CO_2 species. The experimental setup with multi-thermocouples in each reactor gave a new understanding of the axial temperature profile of the catalyst bed, important also for the following simulation of the process.

The obtained experimental data were afterwards compared with the simulation results, modelled with the simulation program Aspen Plus® V9. The program allows the variation of different reactor types as well as implementation of kinetic models. Three different kinetic models from the literature were chosen, corresponding to the process parameters used for methanation experimental tests of steel gases.

3 Theoretical and technological background

The transition of the energy sector towards renewable energies, being more environmentally friendly, affordable and reliable is being driven by climate change, supply security and industrial competitiveness. The share of renewable energy sources such as solar, wind, hydro, geothermal and all forms of biomass has been increasing steadily, and progress towards the European Union set goal of obtaining at least 32% of the final gross consumption from renewable sources by 2030 seems promising. [17]

However, transition to the renewable energy system brings its challenges with it. As already mentioned, as wind and solar power fluctuate strongly over time, a steady energy supply has to be assured. To meet the demand at any time, energy storage systems play an important role, either in the form of electrical, electromagnetic, electrochemical, mechanical or thermal storage potential. As shown Figure 3-1 from Sterner et al. [18], chemical energy storage is preferable when it comes to high storage capacity and long discharge duration. Only chemical storage is of the same order of magnitude as the energy stored in fossil fuel such as natural gas and coal.

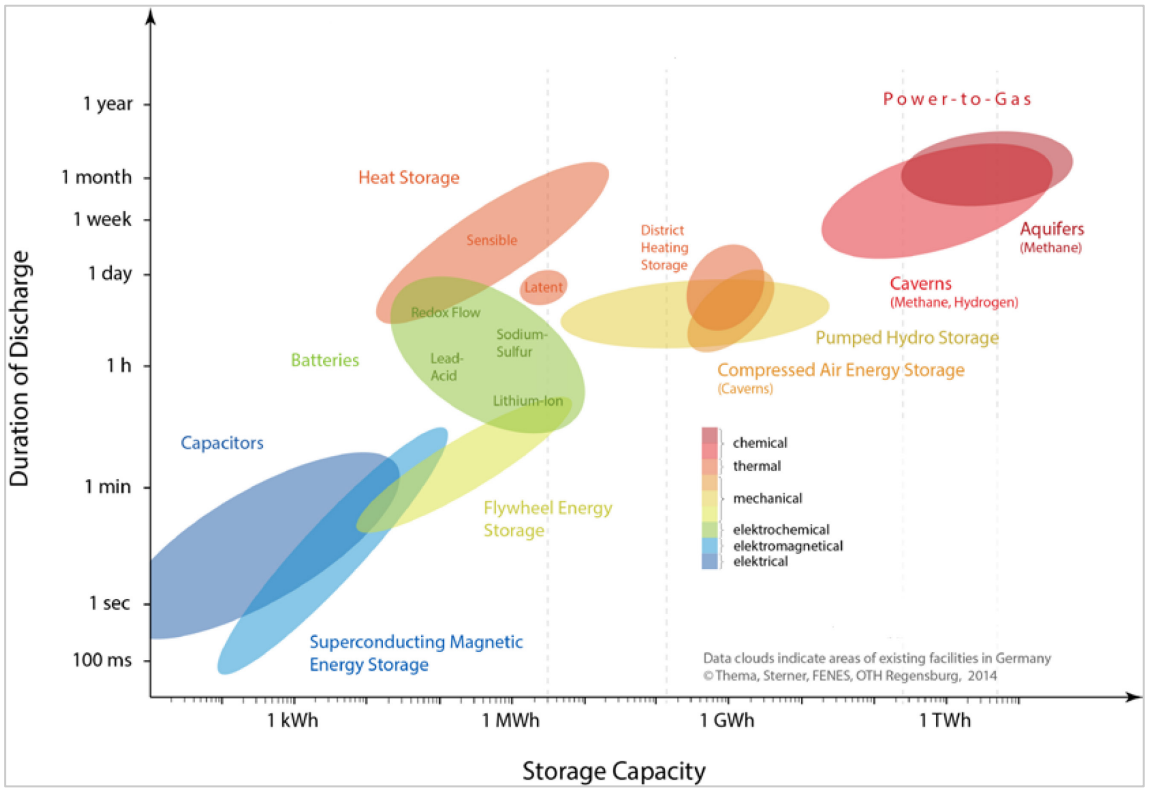

Figure 3-1: Storage capacity of different energy storage systems, taken from [18]

Power-to-Gas (PtG) as a concept can be subordinated under Power-to-X (PtX). PtX (Figure 3-2) describes the conversion of electricity as primary energy and a carbon source into an energy source such as heat, cooling, product, fuel or a raw material. It is a collective name for PtG, Power-to-Liquid (PtL) and Power-to-Chemicals as well as Power-to-Heat, although it does not involve the use of CO_2 or CO.

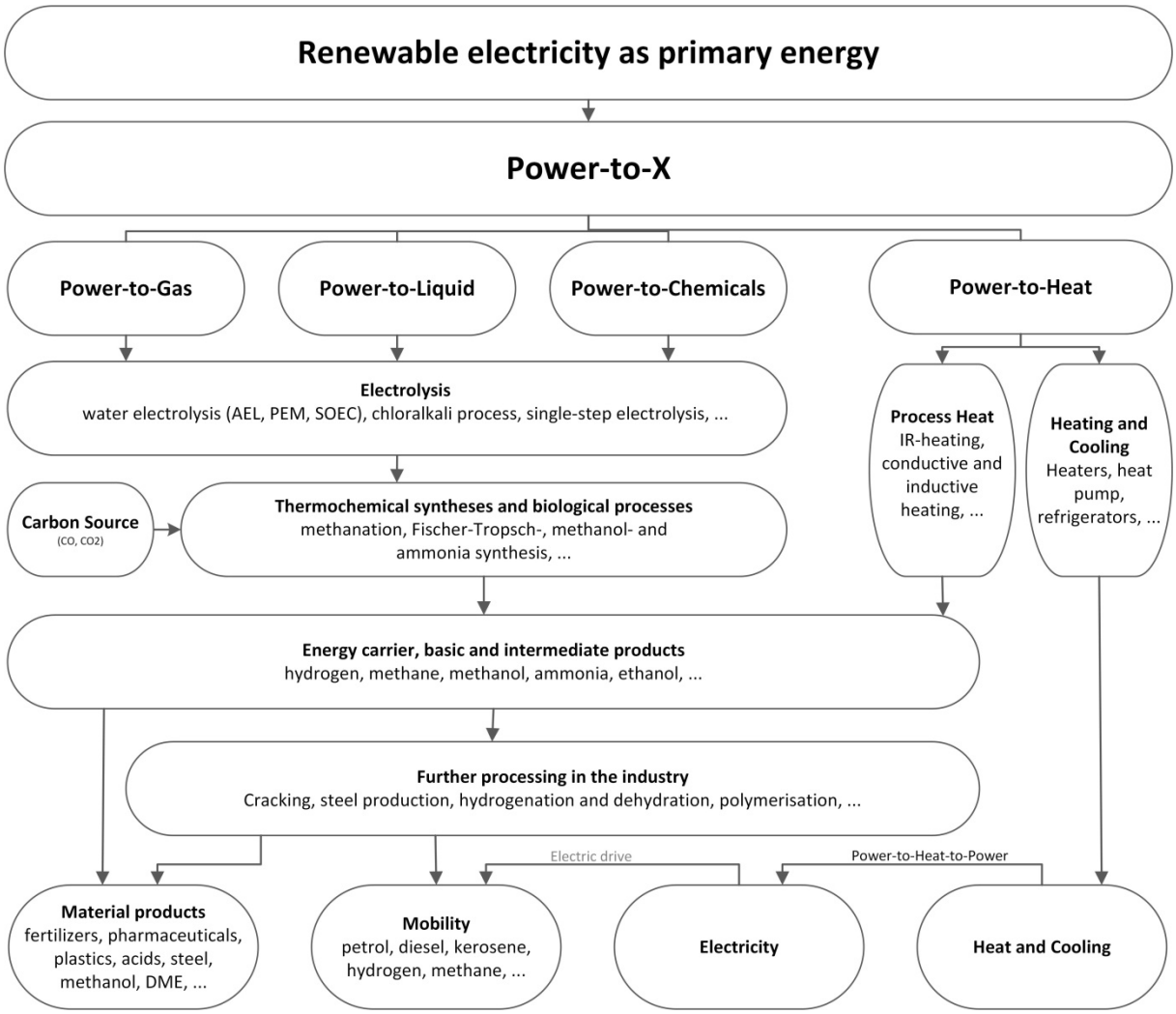

Figure 3-2: Overview of possible energy storage technologies as Power-to-X with added carbon source (adapted from [15])

The separation and long-term storage of the CO_2 emissions in any form (storage or with subsequent usage) can make an important contribution to reducing the carbon footprint. Here the CCU technology stands for Carbon Capture and Utilisation or Usage. The entire process chain consists of CO_2 capture, potential compression for different applications and its subsequent usage as a feedstock for synthesis of different products. [19]

Nevertheless, the necessary carbon source for different energy storage technologies can have different origins and, therefore, different gas compositions. Europe and especially Germany has the highest proportion of PtG projects, with demonstration plants of catalytic as well biological methanation for different carbon sources. As reported in the latest extensive PtG and methanation reviews from Thema et.al [20] and Wulf et.al [21], the majority of the recent research projects deals with either biogas or synthetic composition of biogas or sewage gas from the waste water treatment plants. Since both gases consist of high CO_2 concentrations (30-50 vol-% of CO_2 and 70-50 vol-% of CH_4) with Europe´s annual biogas production of 18,429 million m^3 (in 2015), its utilisation potential has been considered as raw biogas or pure CO_2 with subsequent conversion to bio-methane [22]. Off-gases from

conventional industrial plants, thermal power plants (up to 14 vol-% CO_2) and the iron and steel industry (20–27 vol-% CO_2 in steel gases), as well as the cement industry (14–33 vol-% CO_2), are another potential carbon source [23]. In addition to biogenic CO_2 sources, the iron and steel industry (160 million tonnes CO_{2eq} in 2016 for EU-28 [24]), as well the cement industry (112 million tonnes CO_{2eq} in 2016 for EU-28 [24]), show the greatest potential as a carbon source as they emit high amounts of CO_2. Nevertheless, it has to be mentioned that despite the high emitted amount of CO_2 in coal-based thermal power plants, the electricity sector is moving faster towards the complete decarbonisation, as in the case of the iron and steel industry. A change in the reliance on the fossil energy source is not foreseeable in the short term, as with thermal power plants [25]. Finally, the carbon source can be provided by the direct air capture (DAC) of CO_2 with the current 410.8 ppm CO_2 (July 2020) [26].

The main advantages of the PtG as opposed to other storage technologies (CH_4 being the product mainly considered here) is the utilisation of the already existing infrastructure of the natural gas grid; therefore, the following subchapter will focus on this technology.

3.1 Power-to-Gas

Power-to-Gas (PtG also P2G) describes a concept where renewable electricity is used for the electrolysis of water for the production of hydrogen (H_2) and oxygen (O_2). The H_2 can either be used directly (Power-to-Hydrogen) or is further converted to methane (CH_4) via methanation reaction with a suitable carbon source Figure 3-3.

First proposed by Koji Hashimoto in 1994 as a CO_2 recycling possibility [27], with the increasing interest in renewable energy such as wind and solar power (especially in Europe), the PtG concept has been receiving more attention over the last decade, and an overview of the concept development with resulting projects has been published in several comprehensive reviews [20,28–31].

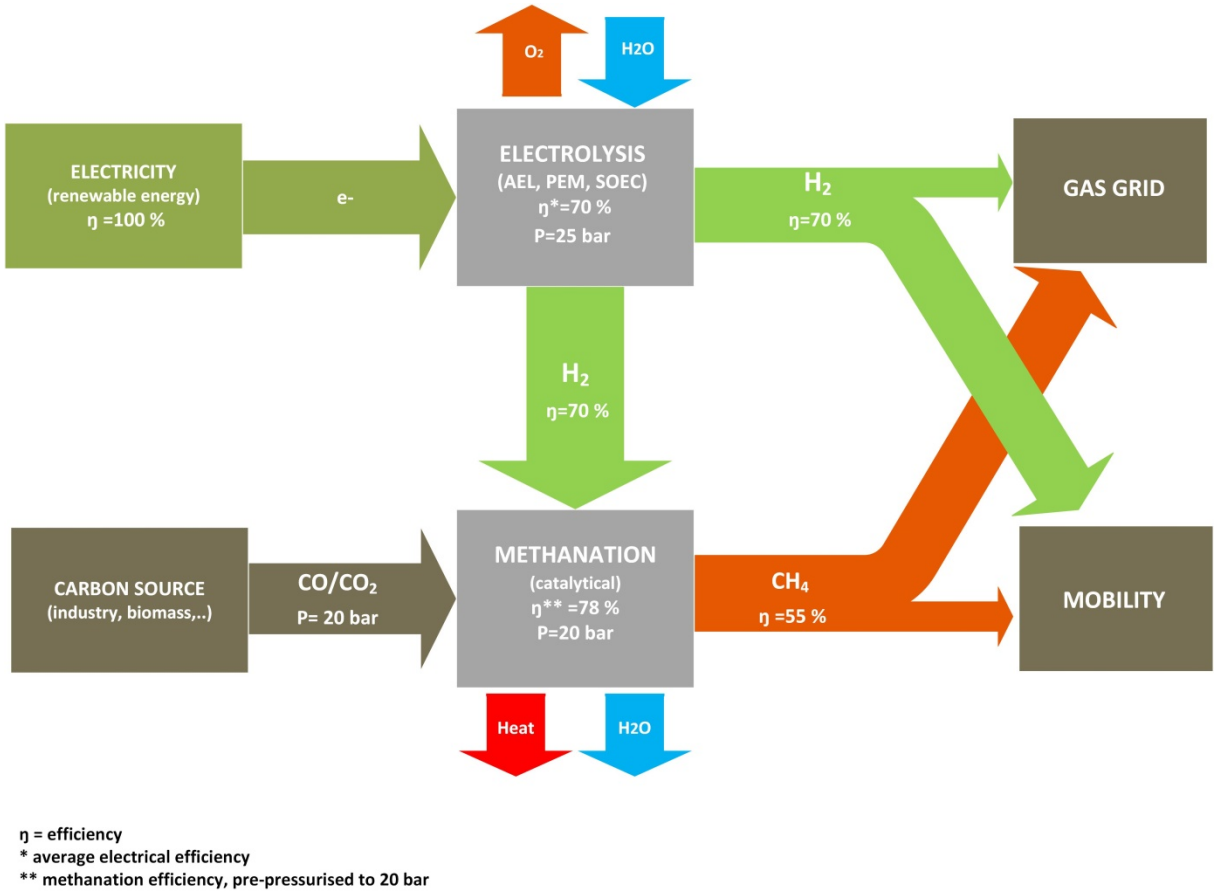

Figure 3-3: Power-to-Gas, overall process efficiency specified as an example of methanation at P=20 bar and average electrolysis efficiency of 70%, without heat recuperation (adapted from [29])

As shown in Figure 3-3, when comparing CH_4 and H_2 as energy carriers, a number of parameters have to be taken into account. Although the direct use of hydrogen is preferred due to the higher electrical efficiency (average electrical efficiency of electrolysis 70%), as well as saving of the cost of the methanation unit and subsequent CO_2 separation unit, its following utilisation is challenging. Whereas CH_4 has no storage limitations in the natural gas grid, the allowed volume of hydrogen is limited for regulatory and technical reasons. The requirements for gas injection into the existing natural gas grid vary in the EU from country to country from 0–10 mol.-%. For Austria the requirement is ≤4 mol.-% [32], whereas, for example, Germany allows up to 10 mol.-% H_2, but it is restricted to ≤2 mol.-% for application in CNG (compressed natural gas) stations, due to the possibility of embrittlement of the tanks [33]. Furthermore, the utilisation of H_2 in fuel cells for the mobility sector and heating sector is prosperous, but it is still a field under development. Other new emerging technologies such as heating systems based on biomass and solar power, battery-electric cars and the already existing conventional systems are in competition with green hydrogen.

The already existing natural gas infrastructure for transportation, storage and utilisation in the energy sector as well in the chemical industry is state-of-the-art, and can be used unchanged with synthetic methane. Another advantage for methane against hydrogen is its higher

volumetric energy density (CH_4=10 kWh/m^3, H_2=3.5 kWh/m^3), and therefore smaller required storage volumes. [25]

The efficiency of the methanation process is limited by thermodynamics, η_{max}= 83% for a stoichiometric mixture of H_2/CO_2 and η_{max}= 80% for H_2/CO, which also decrease when the feed gas is pre-pressurised (on example of 20 bar to η_{max}=78% as shown in Figure 3-3. However, the overall efficiency of the system when methanation is included can be increased and can reach those of pure hydrogen, with recuperation of the released heat from the methanation synthesis [34]. An additional increase in economic efficiency can be achieved with the use of O_2 as the by-product of the electrolysis in steel industry, glass melting or gasification processes [35].

3.1.1 Water Electrolysis

An important step of the PtG technology is the conversion of electrical into chemical energy via water electrolysis. Renewable electrical energy can be used for the production of hydrogen and oxygen via water electrolysis. The overall equation is given by:

$$H_2O_{(l)} \rightarrow \frac{1}{2}O_{2(g)} + H_{2(g)} \qquad \Delta H_r^0 = 286\ kJ\ mol^{-1} \qquad \Delta G^0 = 237\ kJ\ mol^{-1} \qquad \text{(Eq. 3-1)}$$

Three main water electrolysis technologies are available at the moment, namely Alkaline Electrolysis (AEC), Proton Exchange Membrane Electrolysis (PEMEC) and Solid Oxide Electrolysis (SOEC).

AEC is the oldest and the most established technology. Two electrodes, mainly made of nickel or nickel plated steel are immersed in the electrolyte solution ($KOH_{(aq)}$ or NaOH) and separated by a diaphragm, where OH^{-1} is the charge carrier. Due to electrolyte corrosion high maintenance costs arise. The long restart time and the advised continuous operation is one of the disadvantages, while flexible operation due to the electrical energy supply is expected in PtG applications. On the other hand, PEMEC shows a higher flexibility, more compact construction and the operation at higher pressures is of benefit for the subsequent hydrogen applications (such as methanation). Therefore, the latter is lately used as the technology of choice for implementation of PtG [21,29,36,37]. Within the Austrian research project H2Future, the world´s largest pilot-plant PEMEC with 6 MW on ground of the steel manufacturer voestalpine GmbH was installed and put into operation [38]. Generally the PEMEC technology is based on the proton exchange membrane (usually Nafion®) working as a solid polymer electrolyte. However, the usage of noble metals and membranes is making it more costly than AEC. The youngest of the three technologies, the high temperature electrolysis SOEC, has the highest efficiency potential, because the high operating temperatures have thermodynamic benefits (low electrolysis voltage). Another advantage is the possibility of heat coupling with methanation, due to the optimal match between the exothermic nature of methanation and the heat requirement for the water vaporization in the SOEC. [36]

A comprehensive overview of the available water electrolysis is given in different review papers [29,37]. The summary of the important operational parameters is given in Table 3-1.

Table 3-1: Summary of the operational parameters of AEC, PEMEC and SOEC electrolysis [25,29,30,36,37]

	Unit	AEC	PEMEC	SOEC
Cathode reaction		$2H_2O + 2e^- \rightarrow H_2 + 2OH^-$	$2H^+ + 2e^- \rightarrow H_2$	$H_2O + 2e^- \rightarrow H_2 + O^{2-}$
Anode reaction		$2OH^- \rightarrow \frac{1}{2}O_2 + H_2O + 2e^-$	$H_2O \rightarrow \frac{1}{2}O_2 + 2H^+ + 2e^-$	$O^{2-} \rightarrow \frac{1}{2}O_2 + 2e^-$
Cell temperature	°C	40–90	20–100	800–1000
Working pressure	bar	< 30	< 200	< 25
Efficiency	%	62–82	67–82	65–82
Specific energy consumption	kWh m^{-3}	4.2–4.8	4.4–5.0	3
H_2 production/stack	$Nm^3 h^{-1}$	up to 1400	up to 400	< 10
Max. stack capacity	MW	< 6	< 2	< 0.01
State of development		commercial	commercial	pilot plant

3.1.2 Methanation

Methanation is a chemical reaction by which H_2 with CO_2 and/or CO, in the presence of a catalyst, is converted to CH_4 and H_2O. It can be performed in biological or catalytic reactors. In a biological reactor, the methanogenic microorganisms serve as bio-catalyst, whereas in catalytic (chemical) methanation different metal materials catalyse the reaction.

A comparison between both technologies shows fundamental differences. The biological methanation can be performed ex-situ (separate reactor) or in-situ (e.g. biogas digester tank). Possible reactor concepts for ex-situ biological methanation (typically as one stage) are fixed bed reactors, trickle bed reactors and continuously stirred tank reactor (CSTR), where the latter is the predominantly used reactor concept [39]. For the catalytic methanation a range of different reactor concepts has been developed, fixed bed (multi-stage), fluidised bed, three phase, and structured reactors. Biological methanation takes place at lower temperatures (up to 70°C) than catalytic (up to 700°C), and lower pressures (biological < 10 bar, catalytic < 80 bar) [40,41]. Other than catalytic methanation, the biological methanation reaction takes place in an aqueous solution, resulting in gas-liquid mass transfer limitations and consequently lower space-time yields [42]. Despite microorganisms higher tolerance towards hazardous feed gas (e.g. hydrogen sulphide) and process flexibility with immediate recovery after up to 1 month shut-downs [43], microorganisms simultaneously converting CO and CO_2 are still a subject of research [44]. The cost estimation for both technologies varies in the open literature, either due to a lack of cost specification (what is included in the cost, e.g. engineering, construction, etc.) or because the reference for the costs are not uniform (e.g. kW_{el} of H_2 input vs. kW_{SNG} output) [45].

Thus, the choice of the technology strongly depends on the framework conditions such as feed gas composition (carbon source) and volume flow as well as the potentially possible synergies between different operation units (heat utilisation). A comparison between both technologies can be found in Table 3-2.

Table 3-2: Comparison of biological and catalytic methanation

	Catalytic	**Biological**
Catalyst	VIII-X groups metals (Ni, Co, Fe, Ru)	Methanogenic microorganisms (e.g. archaea)
Reactor	Fixed bed, fluidised bed, three phase, structured	CSTR
Operation mode	adiabatic, polytropic, isothermal	isothermal
Reactor stages	1 – 7	1
Catalyst poisons	S-components, HCl, NH_3, O_2, …	Low demands, CO conversion very poor
Temperature [°C]	200 – 700	30-70
Pressure [bar]	5 – 80	1 – 10
By-products	H_2O	Waste water recycling and treatment necessary
Mass transfer	Good	Medium
Efficiency	75-80% 95% with heat recuperation	90%
GHSV [h^{-1}]	2,000 – 10,000	< 100
Upscaling	> MW	> kW
TRL	7 (9)	6

3.1.2.1 Catalytic Methanation

A catalyst changes the rate of chemical reactions to approach the equilibrium but does not change the equilibrium itself. Therefore, it is important to distinguish between kinetics (rate of reaction) and thermodynamics (equilibrium constant of reaction). The concentration reaches the equilibrium concentration faster over a catalyst with a higher activity, but the equilibrium concentration is the same. [46]

The catalytic methanation was first discovered by Paul Sabatier and Jean-Baptiste Senders in 1902, and the reactions are often referred to as the Sabatier reactions or Sabatier-process, given in equations (3-2) and (3-3). [47]

CO_2-methanation:

$$CO_2 + 4H_2 \leftrightarrow CH_4 + 2H_2O \qquad \Delta H_r^0 = -164\ kJ\ mol^{-1} \quad \Delta G^0 = -114\ kJ\ mol^{-1} \qquad \text{(Eq. 3-2)}$$

CO-methanation:

$$CO + 3H_2 \leftrightarrow CH_4 + H_2O \qquad \Delta H_r^0 = -206\ kJ\ mol^{-1} \quad \Delta G^0 = -142\ kJ\ mol^{-1} \qquad \text{(Eq. 3-3)}$$

Beside reactions (3-2) and (3-3), the following reactions have additionally been taken into account in catalytic methanation.

Reverse Water-gas shift reaction (rWGSR):

$$CO_2 + H_2 \leftrightarrow CO + H_2O \qquad \Delta H_r^0 = 41\ kJ\ mol^{-1} \quad \Delta G^0 = 29\ kJ\ mol^{-1} \qquad \text{(Eq. 3-4)}$$

Boudouard reaction:

$$2CO \leftrightarrow CO_2 + C \qquad \Delta H_r^0 = -172\ kJ\ mol^{-1} \quad \Delta G^0 = -120\ kJ\ mol^{-1} \qquad \text{(Eq. 3-5)}$$

CO reduction:

$$CO + H_2 \leftrightarrow C + H_2O \qquad \Delta H_r^0 = -131\ kJ\ mol^{-1} \quad \Delta G^0 = -91\ kJ\ mol^{-1} \qquad \text{(Eq. 3-6)}$$

CO_2 reduction:

$$CO_2 + 2H_2 \leftrightarrow C + 2H_2O \qquad \Delta H_r^0 = -90\ kJ\ mol^{-1} \quad \Delta G^0 = -65\ kJ\ mol^{-1} \qquad \text{(Eq. 3-7)}$$

Methane cracking:

$$CH_4 \leftrightarrow 2H_2 + C \qquad \Delta H_r^0 = 75\ kJ\ mol^{-1} \quad \Delta G^0 = 51\ kJ\ mol^{-1} \qquad \text{(Eq. 3-8)}$$

3.1.2.1.1 Catalyst

There are three important criteria for a catalyst:

- selectivity
- activity
- stability (durability)

Metals of the groups VIII-X have been widely used as suitable catalysts for methanation. They can be sorted according to the activity: Ru>Fe>Ni>Co>Mo and selectivity: Ni>Co>Fe>Ru. Due to high selectivity, good activity and relatively low price, nickel is often chosen as the active substance for the methanation applications. Apart from the active surface itself, the carrier or support materials and promoters as well as the activation procedure of the catalyst contribute to the catalyst´s effectiveness in terms of enlarging the specific surface area and thermal stability of the catalyst and thus the performance.

Commonly used carriers are metal oxide (Al_2O_3, SiO_2, MgO, TiO_2, ZrO_2), with promoters such as MgO, Co, La_2O_3, V_2O_3 and CeO_2. [30,48].

3.1.2.1.2 Catalyst deactivation

When applying the catalyst in the methanation process, the deactivation is of great importance while considering the reactor design, operating parameters and the necessity of feed gas pre-treatment. According to Bartholomew [49,50], with the example of nickel catalyst, deactivation can be divided into three types with the following mechanisms:

- mechanical:
  - Fouling: physical deposition of carbon or coke on an active catalyst surface, usually in the presence of CO and C_xH_y (Boudouard reaction (3-5)).
  - Attrition: loss of the catalytic material due to abrasion (common in fluidised-bed reactors)
  - Crushing: loss of the internal surface areas, caused by pressure fluctuations
- chemical:
  - Poisoning: chemisorption of species on the catalyst active surface (e.g. ammonia, sulphur species (H_2S, SO_2..), Cl)
  - Vapour-solid reactions: formation of $Ni(CO)_4$ at operating temperatures < 250°C in the presence of CO (Eq.3-9) and production of the inactive phases (not just hazardous but leads to the loss of the surface area) [51]

    $Ni_{(s)} + 4CO_{(g)} \leftrightarrow [Ni(CO_4)]_{(g)}$ $\Delta H_r^0 = -159\ kJ\ mol^{-1}$ (Eq. 3-9)

- thermal: degradation or sintering of the catalyst, due to the high operating temperatures (e.g. > 500°C), leading to loss of the surface area and permanent catalyst activity

For the methanation in fixed-bed reactors, all mechanisms with the exception of attrition can occur.

3.1.2.2 Characteristics of the catalytic methanation

The final product composition of a heterogeneous catalytic reaction is subjected to the limitations of thermodynamic equilibrium and reaction kinetics, influenced by the catalyst material, temperature, pressure and gas composition.

3.1.2.2.1 Thermodynamics

The Gibbs free energy minimisation method is based on the principle that the total Gibbs energy of the system has its minimum value at the chemical equilibrium. Due to the complexity of the methanation process it is difficult to determine individual equilibrium constants for exact reaction involved in the methanation [52]. Therefore, the following method can be used to determine the thermodynamic conditions and limitations for the methanation process [53]. There are several available software programs that enable the

calculation. Within the thesis the HSC 7.1 was used for the first analysis of each relevant reaction (under the assumption of an ideal gas), as well as Aspen Plus V9.0 for the Gibbs free minimisation method (under the assumption of a real gas) used for the evaluation of the experimental data.

Methanation can be accompanied by different reactions. Figure 3-4 shows the Gibbs free energy for each relevant reaction (3-2)–(3-8) as a function of temperature, determined by the software program HSC 7.1, under the assumption of ideal gas conditions.

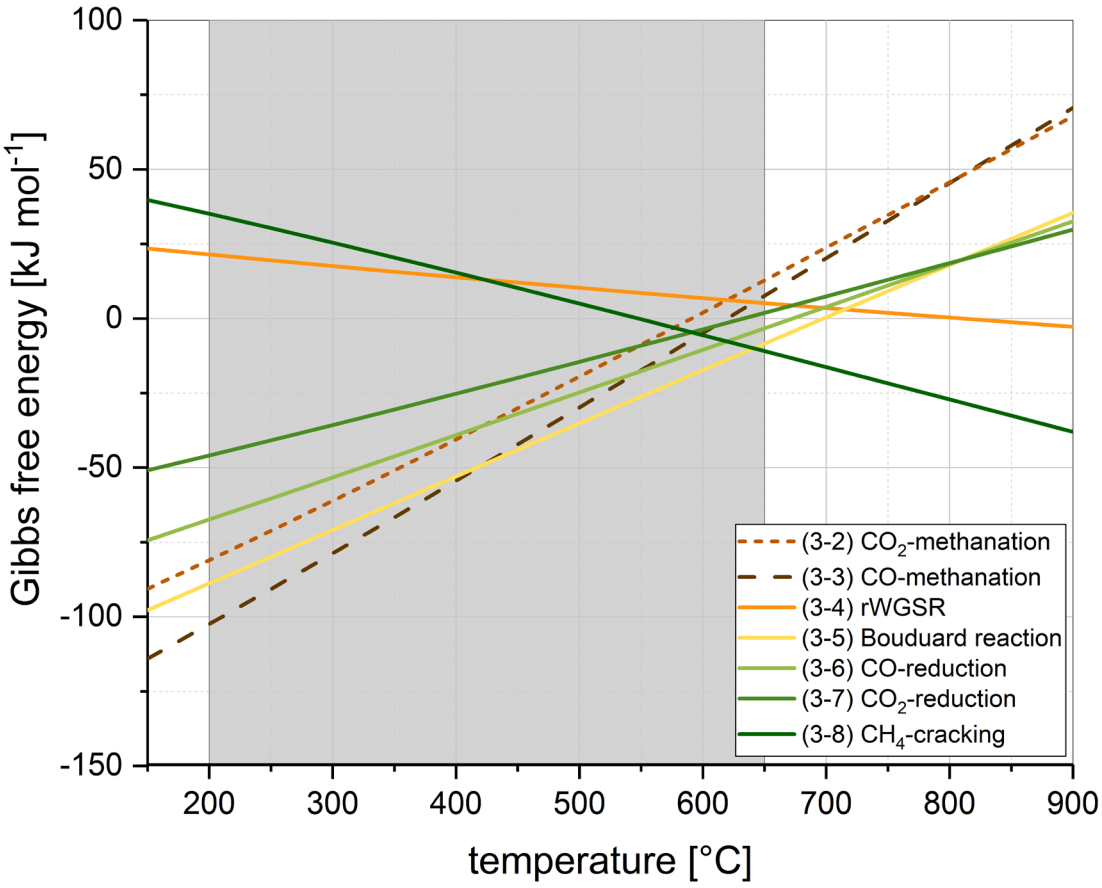

Figure 3-4: Gibbs free energy for each (3-2) - (3-8) reaction, conducted with HSC 7.1

It can be seen that all the exothermic reactions are suppressed with increased temperature, except for the endothermic rWGSR (3-4) and CH_4-cracking (3-8). The CO-methanation is thermodynamically favoured over the CO_2-methanation, with the free energy values being lower than the latter. Furthermore, with temperature increase, the possibility of carbon deposition gets higher. With temperatures from 400°C upwards, the Boudouard reaction and CO reduction start to dominate, inhibiting the conversion of CO_2 and CO, which are completely overruled by the reactions (3-5) – (3-8) from 600°C upwards. Therefore, the temperatures above 550°C should be avoided as well as those below 200°C due to the formation of hazardous $Ni(CO)_4$. The carbon deposition is of concern as it can cause fouling of the catalyst (Chapter 3.1.2.1.2).

A basic thermodynamic equilibrium analysis for each of the main three reactions (3-2)–(3-4) was conducted, considering only the CO, CO_2, H_2, CH_4 and H_2O that occur in the reactions, therefore without the solid carbon formation. CO_2 and CO methanation are volume-contracting reactions of the reactant gases (40% for the CO_2-methanation and 50% for CO-methanation) and therefore pressure dependent. If the pressure increases, higher conversion of CO_2 and CO and therefore higher CH_4 formation can be expected (Figure 3-5 and Figure 3-6), whereas WGSR is not affected by the pressure (Figure 3-7). CO_2 methanation is a linear combination of CO-methanation and WGSR; the latter always accompanies CO-methanation in the presence of a nickel catalyst. With the increased temperature around 550°C, the CO_2 curve achieves its maximum, shifting from the conversion to CH_4 towards the formation of CO. In thermodynamic equilibrium, high pressures favour the production of methane, whereas high temperatures limit it.

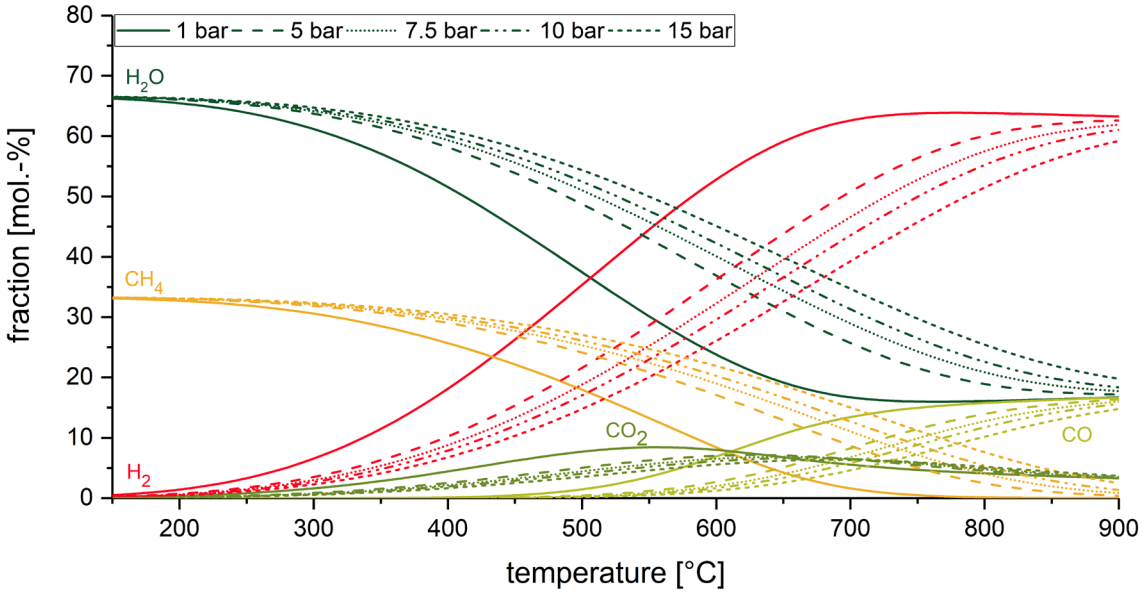

Figure 3-5: Gas composition of the stoichiometric CO_2-methanation as a function of the temperature at different pressures, conducted with HSC 7.1

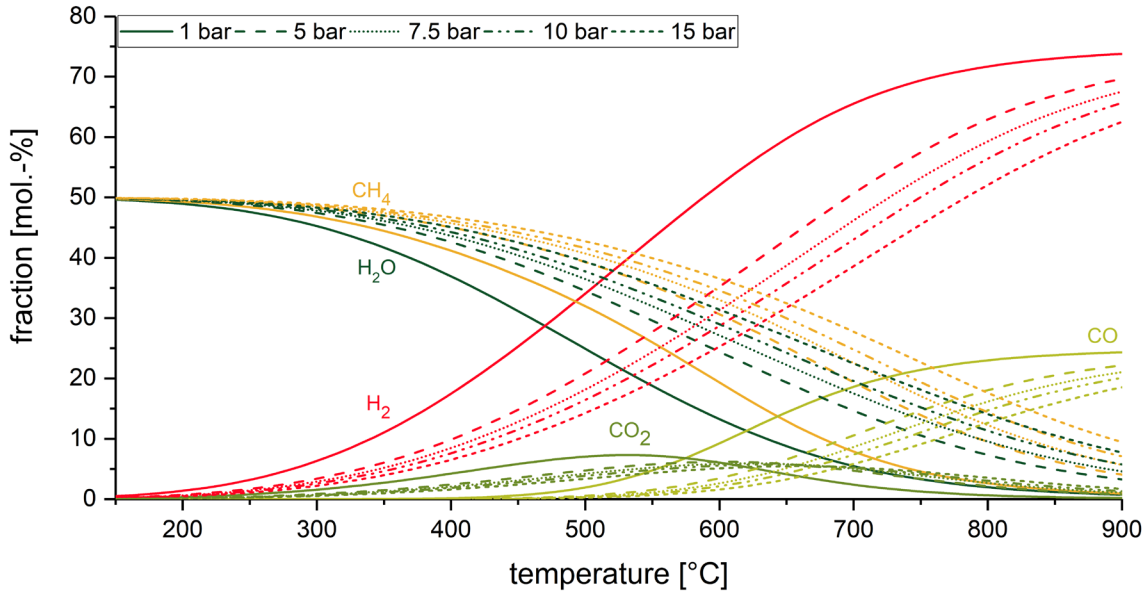

Figure 3-6: Gas composition of the stoichiometric CO-methanation as a function of the temperature at different pressures, conducted with HSC 7.1

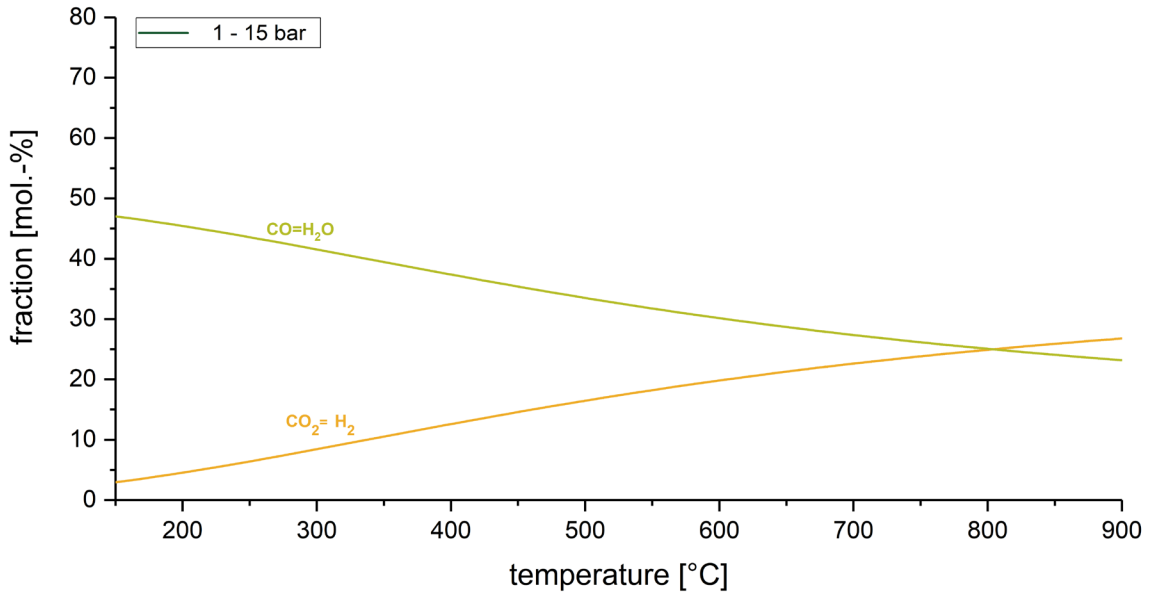

Figure 3-7: gas composition of the stoichiometric rWGSR as a function of the temperature at different pressures, conducted with HSC 7.1

3.1.2.2.2 Kinetics and reaction mechanism

“A reaction mechanism, or equivalently, mechanism, is the fundamental concept of chemical kinetics, which reflects the complexity of the chemical reaction” [54].

A mechanism gives a detailed description of the elementary steps of a reaction; from reactants over intermediates to products. In the case of methanation, as a typical heterogeneous gas-solid catalytic reaction, the dominating reaction mechanism with its rate determining step (RDS) is still the subject of an open discussion, according to the research publications. Several studies with respect to CO [55–57] as well as, separately, CO_2 [58–60] methanation reaction mechanisms have been done over the years, with the application of various catalysts and summarised in comprehensive reviews [30,61–63]. Maio et al. in his review outlined the proposed CO and CO_2 mechanisms as associative and dissociative and accounted for their discrepancy by different reaction conditions [61]. Generally, the two commonly proposed reaction mechanisms differ from one another in the assumed intermediate. As listed in Table 3-3, in the first mechanism (A), applicable for CO and CO_2 methanation reaction, the adsorbed carbon atom (C*) results from the dissociation of CO* which further gradually reacts with H* to CH_4, assuming step 4 as the RDS in mechanism A [56,58]. CO and CO_2 methanation therefore proceeds via the same mechanism, with the difference of an additional first dissociation step of CO_2 [58]. In the case of the proposed mechanism B, no CO dissociation is assumed. Instead, the H* reacts with adsorbed CO* to produce formyl (CHO*), followed by the C-O bond cleavage to CH* and further hydrogenation to CH_4, with assumed step 3 as the RDS [59]. Additionally, intermediates such as formate (HCOO*) presented in mechanism C have been proposed for CO_2 methanation, as well with step 3 as RDS. In the latter mechanism, the adsorbed CO_2 gradually reacts to CH_4 via HCOO* and HCO* intermediates [64–66]. Despite the tendencies toward mechanism A in the early studies, the latest comprehensive computational and experimental studies reported better or equal fits of the rate equations derived from the assumption of mechanism B [57,59,60].

Nevertheless, with both CO and CO_2 present in the feed gas, the CO strongly inhibits the CO_2 conversion, due to the faster adsorption of CO on the catalyst active surface. [67]

Table 3-3: Three proposed reaction mechanisms taken from [59,66]

Step	mechanism A	mechanism B	mechanism C
1	$H_2 + 2^* \leftrightarrow 2H^* +$	$H_2 + 2^* \leftrightarrow 2H^*$	$H_2 + 2^* \leftrightarrow 2H^*$
2	$CO_2 + 2^* \leftrightarrow CO^* + O^*$	$CO_2 + 2^* \leftrightarrow {CO_2}^* + O^*$	$CO_2 + * \leftrightarrow CO_2^*$
3	$CO^* + * \leftrightarrow C^* + O^*$	$CO^* + H^* \leftrightarrow CHO^* + O^*$	$CO_2^* + H^* \leftrightarrow HCOO^* + *$
4	$C^* + 4H^* \leftrightarrow CH^* + *$	$CHO^* + * \leftrightarrow CH^* + *O^*$	$HCOO^* + H^* \leftrightarrow HCO^* + OH^*$
5	${CH_4}^* \leftrightarrow CH_4 + *$	$CH^* + 3H^* \leftrightarrow {CH_4}^* + 3^*$	$HCO^* + H^* \leftrightarrow CH^* + OH^*$
6	$O^* + H^* \leftrightarrow OH^* + *$	${CH_4}^* \leftrightarrow CH_4 + *$	$CH^* + H^* \leftrightarrow {CH_2}^* + *$
7	$OH^* + H^* \leftrightarrow H_2O^* + *$	$O^* + H^* \leftrightarrow OH^* + *$	$CH_2^* + H^* \leftrightarrow {CH_3}^* + *$
8	$H_2O^* \leftrightarrow H_2O + *$	$OH^* + H^* \leftrightarrow H_2O^* + *$	$CH_3^* + H^* \leftrightarrow CH_4 + 2^*$
9		$H_2O^* \leftrightarrow H_2O + *$	$OH^* + H^* \leftrightarrow H_2O + 2^*$

As for various reaction mechanism approaches, different kinetic models, power law or Langmuir-Hinschelwood-Hougen-Watson (LHHW) as well as Eley-Rideal [68], have been proposed for CO and CO_2 methanation over the years. A kinetic model strongly depends on the used catalyst material and reaction conditions (pressure, temperature, gas composition, reactor type).

When using an industrial commercial catalyst, typically Ni/Al_2O_3, the kinetic expression is usually not provided by the manufacturer. Screening of proposed kinetic models from the literature is, therefore, a common approach to find an applicable fit, applied also in the present thesis. Since the 1970´s a number of kinetic approaches have been proposed with regards to CO methanation [67–78] and CO_2 methanation [58,59,67,79–81]. Nevertheless, kinetic models used for the simulation in the present thesis (Chapter 5), as well the basic models the researchers used for their further adaptations, were chosen based on the used catalyst and operating conditions, where CO_2 methanation was described as a linear combination of CO-methanation and WGSR. The kinetic models are summarised by the year of publication in Table 3-4. Xu and Froment derived an intrinsic rate equation for steam reforming of methane and WGSR on a $Ni/MgAl_2O_4$ (15.2 wt.-% Ni) commercial catalyst. When considering WGSR and methanation, the experiments were performed in a fixed-bed reactor with temperatures between 300–400°C and pressures between 3–10 bar [80]. In 2013, Zhang et al. performed experimental studies on a commercial nickel catalyst (50 wt.-% Ni) for elevated temperatures between 275-360°C and pressures between 1–5 bar. They focused on different biomass-derived syngas feed gas compositions, GHSV and influence of

CO_2 and H_2O on the methanation reaction. Based on their experimental data, the reaction rate for CO methanation from Klose/Baerns [71] was adapted by changing the pre-exponential factor. Additionally, Zhang et al. modified the WGSR model from Xu/Froment with attainment of the adsorption term but without considering its exponent [76]. A typical modern methanation process application is subjected to dynamic operating conditions as well as the different nickel load of commercially available catalyst. To address this topic, Rönsch et.al proposed two different rate equations for CO methanation, adapted from Klose over 18 wt.-% commercial catalyst and Zhang over 50 wt.-% commercial catalyst, with the addition of the reverse reaction term of CO methanation. As for the rate equation for WGSR, Rönsch et al. kept the term from Xu/Froment [82]. Kopyscinski et al. developed a kinetic model, based on the experimental data obtained over a commercial nickel catalyst (50 wt.-% Ni) in a fluidised-bed reactor for ambient pressure and temperatures between 200–360°C [83].

All the aforementioned authors used the LHHW model for the proposed kinetic models. The LHHW mechanism, or adsorption mechanism, assumes a rate-determining step and requires adsorption constants of each species for assumed reactions, described in Eq. 3-9:

$$r = \frac{[Kinetic\ factor][Driving\ force]}{[Adsorption]} \qquad \text{(Eq. 3-9)}$$

When compared to the simple power law, the LHHW model is suitable for more complex reaction mechanisms, therefore applicable for complex methanation reactions.

Table 3-4: Kinetic rate expression taken from the literature

Author	Year	Catalyst	Operating conditions	Kinetic rate expression
Klose/Baerns [71]	1984	commercial 18 wt.-% Ni/Al_2O_3	P= 1–25 bar T= 180–284°C	$r_{CO-Meth.} = -\frac{k_{CH_2} K_C K_H^2 p_{CO}^{0.5} p_{H_2}}{(1+K_C p_{CO}^{0.5}+K_H p_{H_2}^{0.5})^3}$ $r_{C_2H_4} = \frac{k_{CH_2} K_C^2 p_{CO}}{(1+K_C p_{CO}^{0.5}+K_H p_{H_2}^{0.5})^2}$
Xu/Froment [80]	1989	commercial 15.2 wt.-% $Ni/MgAl_2O_4$	P= 3–10 bar T= 300–400°C	$r_{CO-Meth.} = -\frac{k_1 p_{H_2}^{-2.5}(p_{H_2O} p_{CH_4} - \frac{p_{H_2}^3 p_{CO}}{K_{METH}})}{(DEN)^2}$ $r_{WGSR.} = \frac{k_{WGS} p_{H_2}^{-1}(p_{H_2O} p_{CO} - \frac{p_{H_2} p_{CO_2}}{K_{WGS}})}{(DEN)^2}$ $DEN = 1 + K_{CO} p_{CO} + K_{H_2} p_{H_2} + K_{CH_4} p_{CH_4} + K_{H_2O} p_{H_2O}/p_{H_2}$
Kopyscinski [83]	2011	commercial 50 wt.-% Ni/Al_2O_3	P= ≈1 bar T= 200–380°C	$r_{CO-Meth.} = \frac{k_1 K_c p_{CO}^{0.5} p_{H_2}^{0.5}}{(1+K_c p_{CO}^{0.5}+K_{OH} p_{H_2O} p_{H_2}^{-0.5})^2}$ $r_{WGSR.} = \frac{k_2 (K_\alpha p_{CO} p_{H_2O} - p_{CO_2} p_{H_2}/K_{eq})}{p_{H_2}^{0.5}(1+K_1 p_{CO}^{0.5}+K_{OH} p_{H_2O} p_{H_2}^{-0.5})^2}$
Zhang [76]	2013	commercial 50 wt.-% Ni/Al_2O_3	P= 1–5 bar T= 275–360°C	$r_{CO-Meth.} = -\frac{k_{CH_2} K_c K_H^2 p_{CO}^{0.5} p_{H_2}}{(1+K_c p_{CO}^{0.5}+K_H p_{H_2}^{0.5})^3}$ $r_{WGSR.} = \frac{k_{WGS} p_{H_2}^{-1}(p_{H_2O} p_{CO} - \frac{p_{H_2} p_{CO_2}}{K_{WGS}})}{DEN}$ $DEN = 1 + K_{CO} p_{CO} + K_{H_2} p_{H_2} + K_{CH_4} p_{CH_4} + K_{H_2O} p_{H_2O}/p_{H_2}$
Rönsch [82]	2015	commercial 18 wt-% Ni/Al_2O_3	P= 1–5 bar T= 275–360°C	$r_{CO-Meth.} = -\frac{k_1 K_C K_H^2 p_{CO}^{0.5} p_{H_2} + k_1 K_C K_H^2 p_{CH_4} p_{H_2O} p_{CO}^{-0.5} p_{H_2}^{-2} \frac{1}{K_{METH}}}{(1+K_C p_{CO}^{0.5}+K_H p_{H_2}^{0.5})^3}$ $r_{WGSR.} = \frac{k_{WGS} p_{H_2}^{-1}(p_{H_2O} p_{CO} - \frac{p_{H_2} p_{CO_2}}{K_{WGS}})}{(DEN)^2}$ $DEN = 1 + K_{CO} p_{CO} + K_{H_2} p_{H_2} + K_{CH_4} p_{CH_4} + K_{H_2O} p_{H_2O}/p_{H_2}$

3.1.2.3 Reactor concepts and heat control

To avert thermodynamic limitation and damages to the catalyst by the formation of hot spots, considerable heat control has to be realised. The primary application of catalytic methanation in the ammonia production, as a gas cleaning step for the removal of CO traces in the H_2 stream, is a mature technology with technology readiness level (TRL) of 9. The consideration of methanation as a main synthesis process became important in the 1970s, as an answer to the oil crisis, where syngas from the coal gasification was used for the production of synthetic natural gas (SNG). It resulted in an broad range of different methanation processes as fixed-bed and fluidised bed reactor concepts [84]. Nevertheless, with the rising interest in PtG, the limitations of the existing processes required its optimisation. Plant size (down-scaling), better heat management and minimising the pressure drop as well as dynamic operation had to be addressed. As a result, several optimisations and new reactor concepts have been developed in the last decade to address the drawbacks.

Depending on the different phases the reactor concepts can be classified as [30]:

- Two-phase (gas-solid)
  - Fixed-bed
  - Fluidised-bed
  - Structured reactors (microchannel, honeycomb, sorption enhanced)
- Three-phase (gas-liquid-solid)
  - Fluidised-bed
  - Slurry

The reactor concepts can be classified, depending on the heat transfer and resulting temperature profile, as adiabatic, isothermal and polytropic, respectively. Each of the reactor concepts has its advantages and disadvantages. Detailed described different concepts can be found in the comprehensive reviews from Götz et al. [29], Rönsch et al. [30] and Kopyscinski et al. [84]. Their short summary is provided in the following sub-chapters.

3.1.2.3.1 Fixed-bed reactors

Adiabatic fixed-bed reactor concepts are typically carried out in multi-stages (2-7), connected in series, to achieve high conversions of the process gases. To control the elevation of the reaction heat, especially in the first reactor, intermediate cooling, removal of the condensate or the recycling of the product gas is applied [84]. Fixed-bed reactors enable a wide operating range in terms of temperature, flow rate and pressure, with high reaction rates. Despite the low mechanical stress on the catalyst, the thermal stress caused by the temperature hot-spots resulting in catalyst sintering, is a disadvantage. Nevertheless, its simple design enables simple handling of the catalyst and good scalability. Two commercially available technologies are compared in the following, namely the Lurgi process and the TREMP process. The Lurgi process (now owned by Air Liquide company) typically comprises two adiabatic reactors. To limit the temperature in the first reactor, a partial product gas after the first reactor is being recycled. The first commercial coal to SNG plant has been in

operation, since its commission in 1984, in North Dakota (USA) operated by Dakota Gasification Company [85]. The Lurgi process is implemented at the end of the process chain after the complex syngas conditioning with CO_2 scrubbing, with operating temperature of 450°C and pressure of 18 bar, resulting in average production of 4.81 million m^3_{SNG}/day [36]. The TREMP process (company Haldor Topsøe), on the other hand, is typically operated with three fixed-bed reactors, pressures up to 30 bar and temperatures between 250-700°C, with downstream intermediate cooling for steam generation [36]. Compared to the Lurgi process, the first two reactors are equipped with a special catalyst, withstanding high reaction temperatures (MCR-2, MCR-2X catalyst) [86]. The largest commercial coal-SNG plants using TREMP process are implemented in China with the capacities up to 16.4 million Nm^3_{SNG} /day [30].

3.1.2.3.2 Fluidised-bed reactors

In fluidised-bed reactors, the catalyst particles are fluidised by the feed gas. The main advantage of this concept is the avoidance of localised overheating (hot-spots), due to a effective heat removal resulting in near isothermal conditions. Therefore, normally only one reactor stage suffice to achieve high conversions of the reactant gas. Another advantage is a high specific surface area of the catalyst. A considerable disadvantage of this concept is the attrition of the catalyst (Chapter 3.1.2.1.2) as well as damage to the reactor wall and limitation of the gas velocity within the fluidised-bed reactor. The gas velocity must be adjusted in such a way that for the catalyst particles, fluidised conditions occur but are not discharged. This creates restrictions of the process flexibility [29,36]. An example of the process reaching a demonstration plant scale is the Comflux process. The process developed in the 1980s by Thyssengas GmbH and University of Karlsruhe was re-established 20 years later by the Paul Scherrer-Institut and demonstrated in 2009 in a $1MW_{SNG}$ plant with 250 operating hours at Güssing (Austria). [84]

3.1.2.3.3 Three-Phase reactors

In this type of reactor, the fine catalyst particles (solid phase) are suspended in a temperature-stable liquid phase (e.g. mineral oil) and fluidised by the inlet gas flow. Due to the high heat capacity of the liquid phase, an effective temperature control can be achieved, resulting in nearly isothermal operation. A disadvantage is the transport resistance between the gas and liquid phases, as well as the decomposition of the liquid material. The LPM process was developed by the company Chem System Inc. (USA) in the 1970s and operated at pilot scale with the capacity up to 1,534 Nm^3_{SNG}/h. [84]. In recent years, new developments of the concept (e.g. utilisation of ionic liquids instead of mineral oils) have been carried out at the Karlsruhe Institute of Technology (Germany) [87,88].

3.1.2.3.4 Structured reactors

Structured reactors, such as sorption enhanced reactors, micro-structured reactors [89,90] and honeycomb reactors, were developed as an answer to the drawbacks of the adiabatic fixed-bed reactors. Honeycomb reactors are fundamentally very similar to fixed-bed reactors, usually subordinated under the fixed-bed reactor concepts. They differ essentially in the structured design of the catalysts. Monolithic honeycombs as carriers for the catalyst are made of metal or ceramic block, where the catalyst is applied via coating procedure. The advantages in favour of the bulk catalysts are in low pressure loss and easier heat dissipation through better radial heat transport, resulting in lower demand for intermediate cooling. In the context of methanation technology, honeycomb reactors have so far only been used on a laboratory scale [91,92].

A summary of different reactor concepts can be found in Table 3-5.

Table 3-5: Overview of the reactor concepts, adapted from [30]

	Fixed-bed	**Fluidised bed**	**Three-Phase**	**Structured**
Temperature Profile	Adiabatic Polytropic	≈Isothermal	≈Isothermal	Polytropic
Catalyst state	Bulk	Fluidised	Fluidised or suspended	Coated
Temperature [°C]	250-700	300-400	300-350	250-500
Reactor stages	2-7	1-2	1-2	1-2
Stress of the catalyst **- mechanical** **- thermal**	 Low High	 High Low	 Moderate Low	 Low Moderate
TRL	7 (9)	7	4-5	4-5
Concepts/process	Lurgi; TREMP; Hicom, RMP; Linde, Vesta	Comflux, BCR (Bi-Gas)	LPM	

3.2 Steelmaking Process as Carbon Source

The mass production of low-price steel became available with the patents of Bessemer in 1856 and Kelly in 1857. With oxygen replacing air, oxidation of the impurities in liquid blast furnace iron (silicon, manganese and carbon) took place, providing faster and cheaper refining and conversion into liquid steel [93].

Generally, two classifications of steel production can be used, depending on the origin of the raw material (Figure 3-8):

- Primary steel production or “iron ore to steel” and
- Secondary steel production or “scrap to steel”;

Where the second classification depends on the technology applied, with four different routes currently used worldwide:

- blast furnace/basic oxygen furnace route (BF/BOF),
- smelting reduction,
- direct reduction and
- electric arc furnace (EAF)

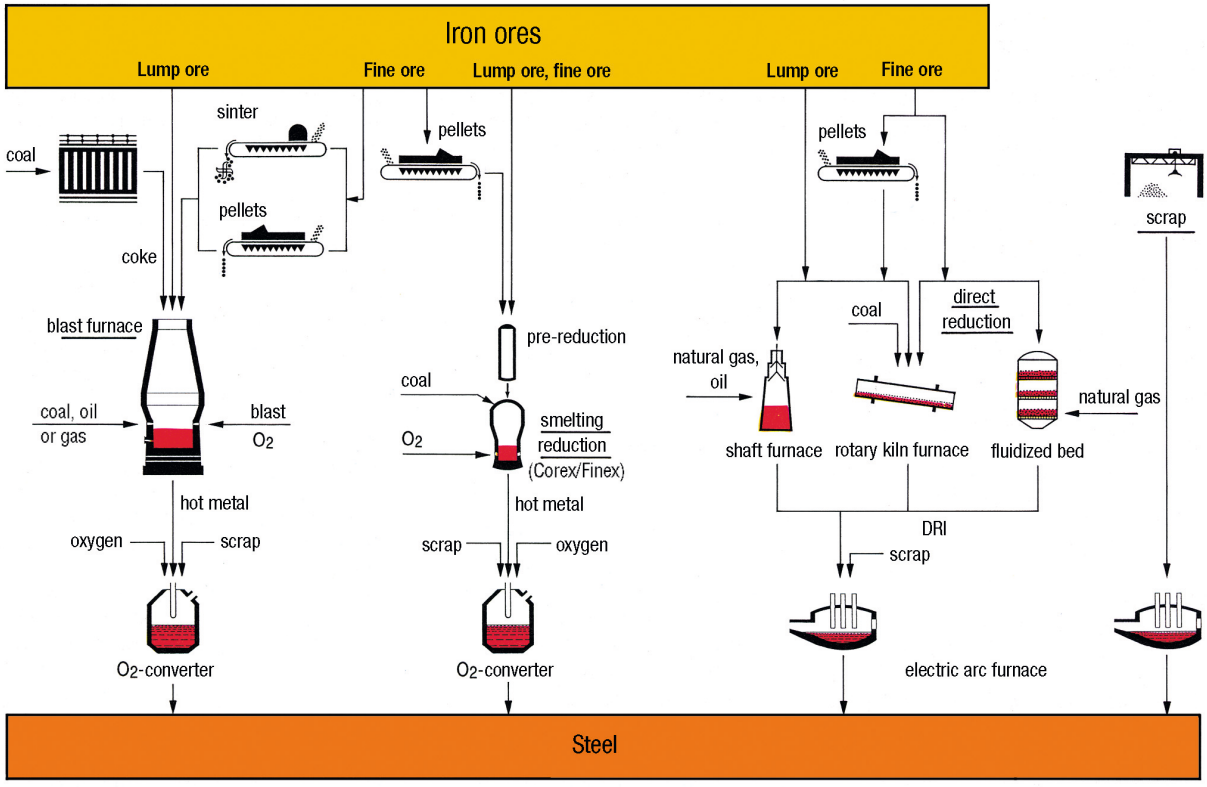

Figure 3-8: Different routes for primary and secondary steel production [94]

The classic BF/BOF route, or integrated steel plant, is the most complex and widely used process. In 2018, 1808 million tons of crude steel were produced worldwide, mainly via the oxygen route (70.8%) and EAF (28.8%), whereas other routes, such as open-hearth furnaces, smelting reduction and direct reduction accounted only for approx. 0.4%. China is the world´s largest steel producer (51.3%), followed by India and Japan. Europe (EU-28) on the other hand accounted for 9.3% of the world´s production, where 58.5% of the crude steel was produced via the oxygen route and 41.5% in EAF. In Austria 6.9 million tons of crude steel was mainly produced via the basic oxygen route (89.7%). [95]

For these reasons, the following subchapter will focus only on the integrated steel plant and gases emitted during steel production, explaining the potential for its usage as a carbon source for the subsequent methanation.

3.2.1 Integrated steel plant

In the blast furnace, the primary reduction of the iron ores takes place. The charge material is used either in the form of lump or fine-grained ores, prepared in the sinter or pellet plant. The oxygen in the iron ore (usually in the form of hematite (Fe_2O_3) and magnetite (Fe_3O_4)) has to be removed through reduction with carbon. The carbon is provided as pulverised coal and coke, produced in the coke oven; other reducing agents such as oil, natural gas or plastics can also be used. A hot blast provides the oxygen to form carbon monoxide with carbon that strips the oxygen from the iron oxides resulting in hot metal and slag that is collected at the bottom of the furnace. The hot metal from the blast furnace is further transported to the basic oxygen furnace, where the impurities such as silicon, sulphur and phosphorus, as well as carbon, are oxidised and accumulated in the form of slag. The formed steel is subsequently treated in secondary metallurgy to achieve the desired chemical composition, product purity and form.

In three essential operational units, as indicated by their names, Coke Oven Gas (COG), Blast Furnace Gas (BFG) and Basic Oxygen Furnace Gas (BOFG) are produced as by-products, accounting, together with slag, for around 733 kg per ton of crude steel. [12]

3.2.1.1 Coke Oven Gas (COG)

As already addressed, coke and coal serve as reducing agents, as well as providing heat and mechanical stability for different material layers in the blast furnace. As the charging material for the blast furnace, coke is produced from the destructive distillation of the coal, usually in the range from 900–1095°C. There are two commercialised coking processes, the beehive process and the by-product process, where the latter is the predominant and the ovens are designed to collect the by-products. The coking oven consists of three main parts: coking chambers, heating flues and the regenerative chambers, where the process starts immediately after coal has been charged. Coal is heated by the heating or firing system and remains in the coke oven until the centre of the coal reaches 1000–1100°C. The moisture is driven off, and carbonisation gas is produced.

The coking process can be divided into three stages:

- primary breakdown of coal (< 700°C) and yield of by-products such as water, CO_x, H_2S, paraffins, olefins and nitrogen-compounds
- secondary thermal degradation and synthesis (>700°C), with release of H_2, CH_4 and aromatic hydrocarbons as well decomposition of nitrogen compounds yielding ammonia, hydrogen cyanides and N_2
- removal of hydrogen from the residue and production of hard coke [96]

The coke oven gas (COG) leaves the oven at 600–700°C via ascension pipes into the collecting main. Before its utilisation, the impurities as well valuable by-products such as tar, light oils, naphthalene, ammonia and sulphur are separated from the raw gas in multi-stage gas scrubbing. In the first stage, the gas is cooled to remove water and dissolved tar, phenol and part of the ammonia is removed, followed by the next stage of scrubbers removing the sulphur compounds, the rest of the ammonia and BTX (benzene, toluene, xylene), depending on the process selected as an individual cleaning step. The cleaning of the impurities is necessary in this way to avoid the fouling of the equipment, as well as the SO_2 and ammonia due to the possibility of corrosion. [97]

The composition of COG depends on coking time (14–28 h) and coal composition. A general overview of the raw gas composition (Table 3-6) was taken from [12]

Table 3-6: Typical raw COG composition

Raw gas	Units	
H_2	vol-%	39–65
CH_4	vol-%	20–42
C_xH_y	vol-%	2–8.5
CO	vol-%	4–7
CO_2	vol-%	1–3
H_2S	g Nm^{-3}	4–12
NH_3	g Nm^{-3}	6–8
BTX	g Nm^{-3}	20–30
Yield [98]	Nm^3 t_{coal}^{-1}	410–560
Lower heating value	MJ Nm^{-3}	17.4–20

Due to its high calorific value, it is usually utilised for the enrichment of other steel gases for further usage, for example in blast furnace stoves, under firing of the coke oven or generally for other high-temperature processes as well as a reducing agent and for use in power plants. [12]

3.2.1.2 Blast Furnace Gas (BFG)

The blast furnace (BF) remains by far the most important process for the production of hot metal (pig iron). A continuously operating counter-current flow furnace is charged with iron

ore along with sinter, pellets or both, additives and reducing agents (coke) and fed from the top of the furnace through a charging system. A hot air blast, enriched with oxygen and auxiliary reducing agents, is injected on the tuyère lever providing reducing agents. The air blast reacts with the reducing agents to produce mainly carbon monoxide (CO), which in turn reduces iron oxides to metal iron shown in reactions (3-9) – (3-12). The hot metal is collected in the bottom along with the slag, where both products are cast on a regular basis. The hot metal is transported, for example, in torpedo vessels to the steel plant (basic oxygen furnace) and the slag processed to produce aggregate, granulate or pellet for road construction and cement manufacture. The blast furnace gas is collected at the top of the furnace and, after treatment, distributed around the steel-works and used as a fuel for heating or for electricity production. [12][99]

In the BF, the coke reacts with the oxygen from the hot air, resulting in CO_2 heating the process with the released heat. Due to the Boudouard reaction that occurs, this is parallel to the generation of CO and H_2 from the water steam. The ore, mostly consisting of hematite (Fe_2O_3) and magnetite (Fe_3O_4), is reduced to iron while CO is oxidised to CO_2. The main reactions are depicted in Eq. 3-9 to Eq. 3-12.

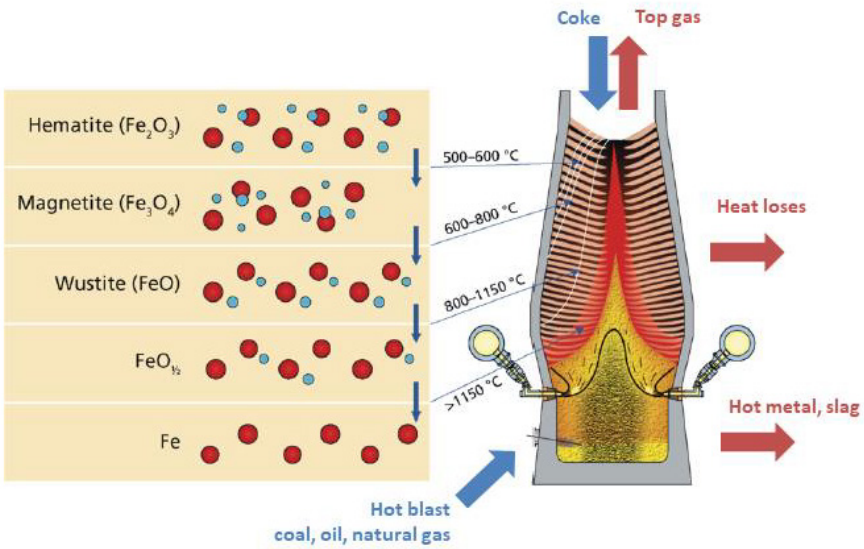

Figure 3-9: Input and output stream and reduction of the iron ore in a blast furnace, adapted from [100]

$$C_{(s)} + O_{2(g)} \leftrightarrow CO_{2(g)} \quad \text{(Eq. 3-9)}$$

$$CO_{2(g)} + C_{(s)} \leftrightarrow 2CO_{(g)} \quad \text{(Eq. 3-10)}$$

$$Fe_2O_{3_{(s)}} + 3CO_{(g)} \leftrightarrow 2Fe_{(s)} + 3CO_{2(g)} \quad \text{(Eq. 3-11)}$$

$$Fe_3O_{4_{(s)}} + 4CO_{(g)} \leftrightarrow 3Fe_{(s)} + 4CO_{2(g)} \quad \text{(Eq. 3-12)}$$

The formed BFG (top gas), as shown in Figure 3-9, consists of CO, CO_2, N_2 and H_2 with impurities such as sulphur and cyanide compounds and large amounts of dust from the burden. A typical BFG composition range can be found in Table 3-7, with approximate production of 1,200–2,000 Nm^3 BFG /ton of hot metal. [12]

Table 3-7: Typical raw BFG composition

Raw gas	Units	
H_2	vol-%	1–5
CH_4	vol-%	-
CO	vol-%	19–27
CO_2	vol-%	16–26
N_2	vol-%	44–58
C_xH_y	g Nm^{-3}	37–250
H_2S	g Nm^{-3}	4–12
NH_3	g Nm^{-3}	10–40
Yield	$m^3t_{hot\ metal}^{-1}$	1,200–2,000
Lower heating value	MJ Nm^{-3}	2.6–4

3.2.1.3 Basic Oxygen Furnace Gas (BOFG) or Converter Gas

There are several types of reactors/converters used for the basic oxygen steelmaking process. The most commonly used is the LD converter (Linz-Donawitz) applied for hot metal with a low phosphorus content, with a typical capacity of 400 tonnes of steel per converter vessel [101].

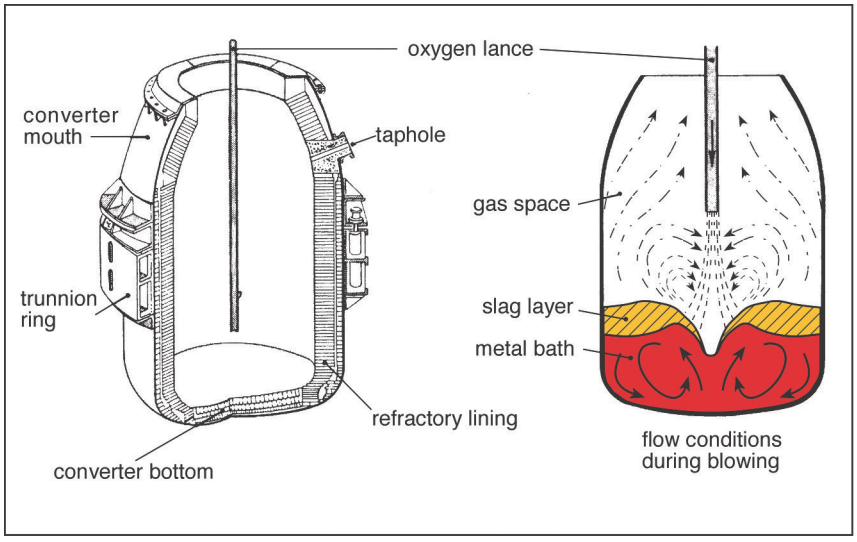

Figure 3-10: Simplified scheme of LD-converter, taken from [94]

The converter (Figure 3-10) is pear-shaped with a refractory lining, where oxygen is blown into or through the metal bath in a basic lined vessel by a water-cooled vertical pipe (oxygen lance). Oxygen with a high purity from an air separation plant is used for the oxidation

process of the hot metal in which the accompanying elements (e.g. silicon and manganese) and the carbon content of approximately 4% reduces under 0.5%, causing a temperature rise to 1700°C. To control the temperature rise, additives such as scrap metal, lime and sponge iron are added. The dissolved carbon reacts with oxygen, resulting in high concentrations of CO and small amount CO_2. The main advantage of this process is the good mixing of the melt and lower amount of produced smoke, but the process is limited by the quantities of used scrap. The generated BOFG contains a large amount of dust. The de-dusting takes place in several stages usually with venturi-scrubbers or dry and wet electrostatic precipitators (ESP) [12,101].

Table 3-8: Typical raw BOFG composition [12]

Raw gas	Units	
H_2	vol-%	2–10
CH_4	vol-%	-
CO	vol-%	55–80
CO_2	vol-%	10–18
N_2	vol-%	8–26
C_xH_y	g Nm^{-3}	-
H_2S	g Nm^{-3}	-
NH_3	g Nm^{-3}	-
Yield	m^3 $t_{liquid\ steel}^{-1}$	500–1,000
Lower heating value	MJ Nm^{-3}	7.1–10.1

Although all three steel gases are utilised in the integrated steel plant, covering part of the energy demand (heat and electricity), their share of emitted CO_2, not only by composition but also amount, varies. Generally, 69% of the emitted CO_2 originates from BFG, 7% from the BOFG, 6% from COG and the rest from imported fossil fuels required in the steel production [102]. The consideration of their alternative re-utilisation as a feedstock for the chemical industry has been a part of the research since the early 1950s. Nevertheless, the main source of the CO_2 emissions, the blast furnace itself, is a well established and highly efficient process, without additional possibilities of reducing its necessary carbon demand. Despite environmentally friendlier alternative technologies (e.g. direct reduction, EAF), the resource demand for their implementation in such production measures as BF exceeds those available in the medium term (e.g. renewable energy, green hydrogen) as well as requiring additional high investment costs [103].

3.3 Coupling an integrated steel plant with renewable energy

Several theoretical studies have emerged in the recent years [104–107], with the following research projects across Europe exploring the alternative utilisation of steel gases and coupling it with renewable energy to produce valuable products.

The largest German steel producer, thyssenkrupp, is leading the “Carbon2Chem” project, comprised from consortium of 18 project partners and funded by the German Federal Ministry of Education and Research [108,109]. During the project duration (2016-2026), the possibility of methanol [110–112], ammonia/urea [113], higher alcohols and polymers [114] as well as oxymethylene ether (OME) synthesis with the utilisation of BFG, BOFG and COG are being investigated. As a result, a reduction of 20 million tons of CO_2 per year is expected [115].

In 2018 the EU funded project “i3-upgrade” started, supported by the Research Fund for Coal and Steel and under participation of Austria´s largest steel producer voestalpine Stahl GmbH. In this project, the possibilities of converting steel gases under dynamic conditions into methanol and SNG, using BFG and BOFG as a carbon source are explored [116]. As for the methanation process, two reactor concepts are being explored: load-flexible methanation with the utilisation of a newly developed ceramic honeycomb catalyst [117] and a structured fixed-bed reactor, with integrated heat pipes for reactor cooling [118].

Additionally, in the project “Steelanol” the technology from LanzaTech is being implemented at the ArcelorMittal steel plant in Ghent (Belgium), where CO from the BFG/BOFG will be used as a feed in the gas-fermentation for ethanol production as well as bio-based raw materials. The estimated production of 25,000 tonnes of ethanol per year in a demonstration plant is expected. [119,120]

An example of the alternative utilisation of steel gases can be seen in the Figure 3-11. Possible integration options were explored in the research project “RenewableSteelGases”, funded by the Austrian “Klima- und Energiefonds” from 2017-2020, with the cooperation of the steel producers voestalpine Stahl GmbH and voestalpine Stahl Donawitz GmbH [121–123]. The concept, based on H_2 production by water electrolysis and additional biogenic H_2 production by dual fluidised-bed gasification of biomass [124], was subsequently used for the methanation of the steel gases or biogenic CO_2, producing SNG. Furthermore, O_2 utilisation from electrolysis in the steel production as well as in the biomass gasification process was explored. Ten scenarios were specified in order to map the renewable energy integration and the CO_2 reduction potential. The scenarios were supported by the experimental results from biomass gasification as well as catalytic methanation, on which the present thesis is based. The aim of the scenarios was the minimisation or complete substitution of the integrated steel plant´s demand for fossil natural gas (NG), with the premise of avoiding significant modifications in the existing steel plant infrastructure. Therefore, despite higher H_2 concentration, the COG was not considered as an H_2 source in the scenarios, since its withdrawal from the steel production would result in additional demand for NG. Three

extreme scenarios (1-3) and seven scenarios realistic in the medium term (4-10) are listed in the following. Based on the current biomass fuel availability and already installed gasification capacity in the European perspective, scenarios 7-10 were limited by 100 MW_{th} as the maximum plant size of the biomass gasification plant [125].

- Scenario 1: complete NG substitution with methanation of BFG
- Scenario 2: complete CO_2 reduction via methanation of BFG and BOFG
- Scenario 3: complete CO_2 reduction via methanation of BFG, BOFG and COG
- Scenario 4: methanation of biogenic CO_2 stream of biomass gasification
- Scenario 5: methanation of biogenic CO_2 stream of biomass gasification operated in OxySER mode
- Scenario 6: utilisation of biogenic H_2 and CO_2 streams in OxySER mode
- Scenario 7: complete NG substitution with methanation of BFG and biomass gasification limited to 100 MW_{th} gasification power
- Scenario 8: complete NG substitution with methanation of BFG with biomass gasification limited to 100 MW_{th} gasification power and without N_2 separation
- Scenario 9: complete NG and PCI (pulverised coal injection) substitution with methanation of BFG and BOFG, with biomass gasification limited to 100 MW_{th} gasification power
- Scenario 10: complete NG substitution with biomass gasification limited to 100 MW_{th} gasification power (BOFG)

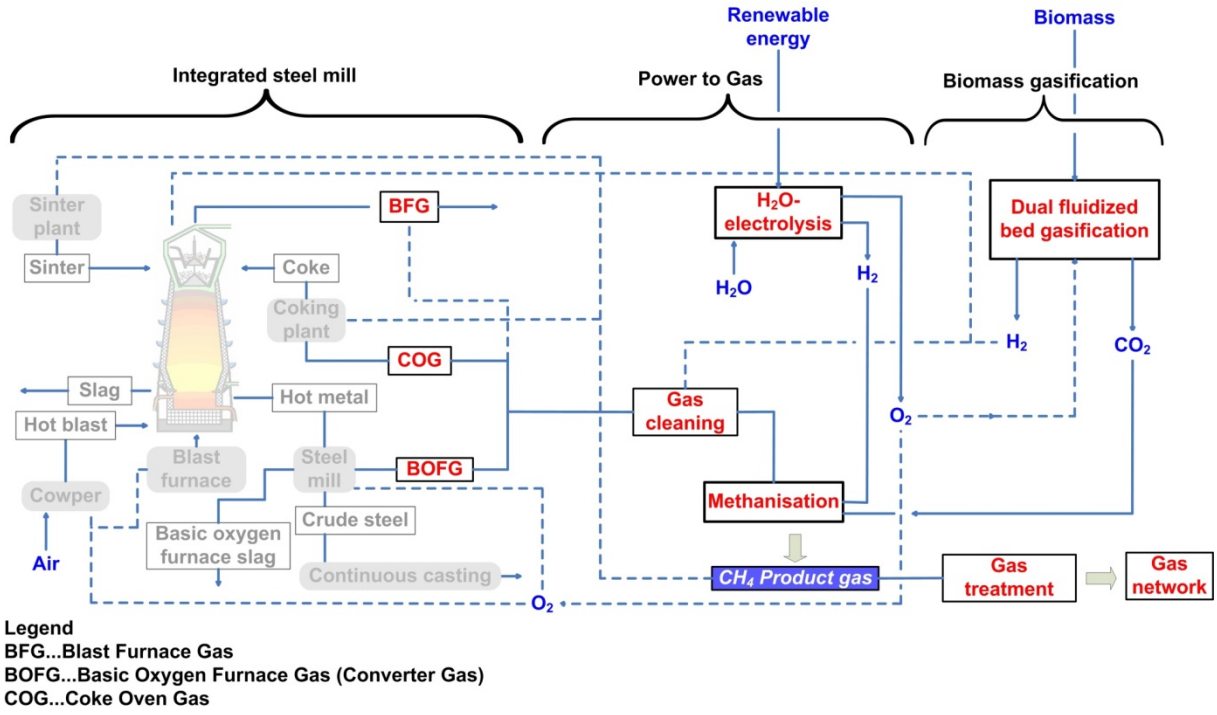

Figure 3-11: Possible integration variations in the project "RenewableSteelGases"

The multidisciplinary process evaluation, in the sense of systemic, ecological, techno- and macro-economic analysis of the ten scenarios, provided a good overview of the order of magnitude of required renewable energy with a CO_2 emission reduction potential. A CO_2 emission reduction of 0.81 million tonnes per year is possible through a complete substitution of the steel plants NG demand, where the NG demand can be substituted by a lean product gas from the methanation of BFG or BOFG. However, the requirement of the renewable electricity as well as biomass substantially exceeds the resource availability. On example of extreme scenarios, the required renewable energy as well as the biomass gasification rise up to 3 GW_{el} and 3 GW_{th}, respectively. Despite the limitation of the maximal biomass gasification plant size, the necessary renewable electricity cannot be provided to this order of magnitude in the foreseeable future.

A detailed overview on example of the scenario 9, supported by the experimental results of catalytic methanation, can be found in Chapter 4.4.

4 Experimental

The methanation experiments were carried out at the laboratory-scale test plant at the Chair for Process Technology and Industrial Environmental Protection (VTiU). The test plant for catalytic methanation has been in operation since 2013, financially supported by the Austrian Research Promotion Agency (FFG) and designed for early studies of CO_2-methanation by P. Biegger [92] and A. Felder [126]. Used for diverse methanation research projects over these years, a number of component and instrumentation equipment optimisations have been made. In Chapter 4, an overview of the laboratory-scale test plant modifications and the experimental setup with evaluation of the experimental series will be presented. The overall objective of the experimental research was to determine the behaviour of the methanation of BFG and BOFG at different operating conditions, particularly elaborating the influence of the N_2 on the methanation process.

Figure 4-1: Methanation laboratory scale test plant at VTiU

4.1 Laboratory-scale test plant

The laboratory test plant consists of three fixed-bed reactors connected in series with the purpose of achieving a multi-stage fixed-bed methanation. It enables the variation of CO, CO_2, H_2, CH_4 and N_2 synthetic feed gas ratios as well as the application of different catalyst materials and variation of their amount. Their effect can be investigated under different operating conditions and at any number of reactors, from one-stage to three-stage, giving flexibility for experimental planning. With the system flows up to 50 $l_n\,min^{-1}$, temperatures up to 650°C and pressure of maximal P_{abs}=21 bar can be realised. A detailed P&ID scheme can be found in Figure 4-2, and a description of the individual components is provided in the following subchapters.

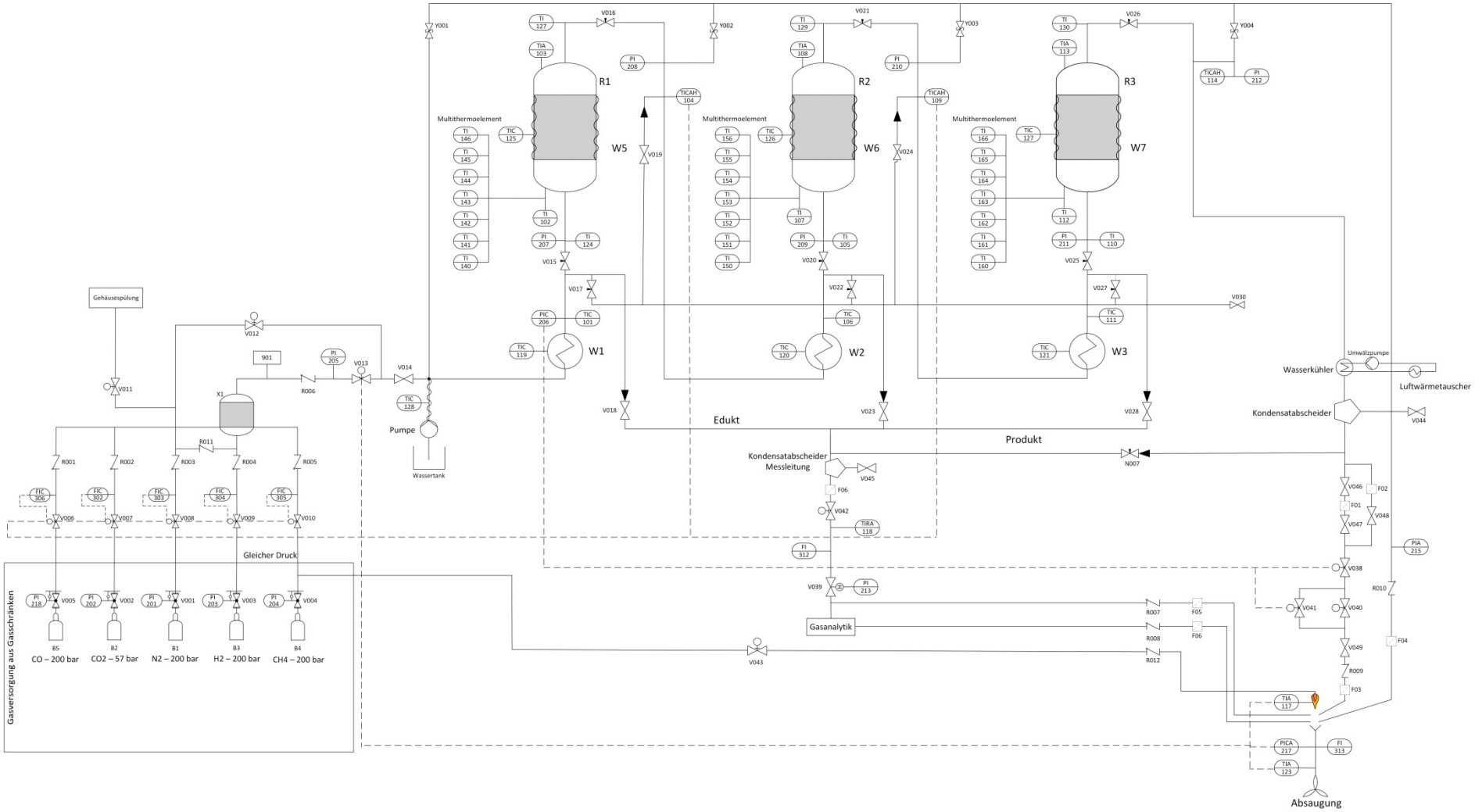

Figure 4-2: P&ID diagram of the methanation laboratory test plant at VTiU

The educt gases from gas cylinders are selectively added via mass flow controllers and homogenised in a mixing unit. The gas mixture can be preheated in heat exchangers (W1-W3) before entering each reactor. In the reactors, a minimum temperature of 250°C is set by means of electric heating sleeves (W5-W7), primarily with the purpose of avoiding the toxic $Ni(NO)_4$ formation and ensuring maximum activity of the catalyst. As already discussed in Chapter 3.1.2.1.1, to prevent possible carbon deposition, when the conditions are favourable for the Boudouard reaction, a steam supply unit was implemented. After the third reactor, a condenser is installed by means of water cooling to separate water, which is formed as a by-product of the methanation reaction. For safety reasons, the dried gas is burned in a torch at the end of the process and the burned gases vented off. Upstream and downstream of each reactor, a gas sample can be taken for the online analysis.

Generally, the laboratory test plant setup can be divided into three segments:

- reactor unit
- peripheral
- process control system (PCS).

The three-stage fixed-bed methanation plant has been optimised with new pressure reactors and pressure vessels, as well as a shorter pipe run. Furthermore, a magnetic metering pump for a water steam input in the educt gas has been put in operation.

4.1.1 Reactor Unit

Three fixed-bed reactors connected in series are the heart of the test plant. The first implemented reactors used for the early studies of the CO_2-methanation were exchanged for a new reactor concept. Due to the old reactor design and their massive construction (the weight of a single reactor is 190 kg), the heat losses were high and the handling was poor. Using the expertise in the field of high-pressure equipment and components, the new design of the compact flange “BestLoc® Compact Flange (Norsok L-005)” from the company BHDT GmbH was installed, and a weight reduction of nearly 80% was achieved. [127]

As reactor material, a 304H chromium-nickel austenitic stainless steel (1.4948), beneficial in terms of heat conductivity and weight, was used. The reactor has a length of 300 mm and 80 mm in diameter, therefore a volume of 1.51 dm^3. To protect the reactor from corrosion, a protective coating made of Balinit A (titanium nitride TiN), with typical “gold” colour was applied using Physical Vapor Deposition (PVD) technique. The screw-in sleeves implemented on the reactor vessel head (22 mm from the gas inlet position) for the axial temperature measurement of the reactor inside provide the flexibility of being changed if needed. A detailed drawing of the reactor can be found in Appendix A. With regard to the electric heating sleeves, nozzle band heaters are installed, with 500W power and temperatures up to 500°C can be realised. The reactors are insulated with insulating casing (company Hennlich GmbH).

Figure 4-3: Fixed-bed reactor without insulation (left) and with opened flange (right)

4.1.1.1 Catalyst implementation

Before adding the catalyst, a layer of inert spheres 9.5 mm HiDur® stoneware balls (RVT GmbH, Table 4-1) is added in order to achieve homogenisation and preheating of the feed gas. After adding the catalyst, the same material is used by means of keeping the catalyst in place while adding the reactant gas from the bottom up.

Table 4-1: Technical specification for HiDur® Stoneware balls [128]

Parameter	Unit	Specification
SiO_2	wt.-%	< 80
$SiO_2 + Al_2O_3$	wt.-%	> 90
TiO_2	wt.-%	0.5–0.8
Fe_2O_3	wt.-%	0.4–1.2
CaO	wt.-%	0.6–0.9
K_2O	wt.-%	2.3–3.0
Na_2O	wt.-%	0.5–0.8
Dissolved Fe	wt.-%	≤ 0.1
Spherical Form	mm	8.1–11.2 (9.5)
Density	kg L^{-1}	1.35

4.1.1.2 Catalyst

As catalyst, a commercial spherical methanation catalyst METH 134® from the company C&CS (catalysts &chemical specialities) GWP mbH was used. The alumina-supported nickel(II)oxide catalyst is commercially used for methanation applications in ammonia

synthesis or syngas production. The catalyst support consists of Al_2O_3 with nickel load of 20 wt.-% and 0.9 kg dm^{-3} density. The catalyst was implemented in the reactor in oxidised form and its reduction was carried out according to the manufacturer instructions. Under inert nitrogen atmosphere, the catalyst was heated up to 315°C ± 10°C and H_2 as process gas was used as reducing agent.

$$NiO + H_2 \leftrightarrow Ni + H_2O \qquad \text{(Eq. 4-0)}$$

Although the activation is not a strong exothermic process, to avoid a temperature rise (maximum allowed 65°C per hour), it was always carried out stepwise with H_2/N_2 mixtures. In Table 4-2, the general chemical and physical specifications of the catalyst are provided. [51]

Table 4-2: Technical specification for Meth134® catalyst specifications

Parameter	Unit	Specification
Ni	wt.-%	20.0 ± 1.0
Al_2O_3	wt.-%	65.0 ± 3.0
CaO	wt.-%	5.0 ± 2.0
S	wt.-%	≤ 0.05
Loss on Ignition at 540°C	wt.-%	≤ 10.0
Spherical Form	mm	3–6
Density	kg dm^{-3}	0.90 ± 0.10
Particles < 2.8 mm	wt.-%	≤ 5.0
Particles > 6.3 mm	wt.-%	≤ 5.0

Figure 4-4: Methanation catalyst METH 134®

4.1.2 Peripheral

The peripheral segment consists of mass flow controllers, gas analysis, steam supply, and heat exchangers. The components are connected with 6 mm diameter stainless steel pipelines (1.4404) and the regulation of the direction of flow is partly carried out manually with the help of needle (T<315°C) and ball (T<170°C) valves. Thermocouples type K (Ni-Cr/Ni) with single point temperature measurement as well multi-thermocouples for an axial temperature profile are used for the temperature measurement, where the pressure in the test plant is controlled and measured with pressure transmitters PITC-I.

4.1.2.1 Mass Flow Controllers (MFC)

The gas feed segment consists of five gas cylinders for CO, CO_2, H_2, N_2 and CH_4, where the mass flow controllers (MFC) from Bronkhorst High-Tech B.V. are used to control the feed gas input. Before the gas enters the reactor, the gases are mixed in the mixing vessel which is filled with 9.5 mm HiDur® stoneware balls, RVT GmbH (Table 4-1). Specifications of the MFC controllers are shown in the Table 4-3.

Table 4-3: Specifications of the MFC from Bronkhorst High-Tech B.V.

Device	Gas	Type	Range	Unit	Accuracy
MFC	CO	F-201CV-20K	0.2–10	l_n min^{-1}	±0.5% Rd* plus ± 0.1% FS**
MFC	CO_2	F-201CV-20K	0.2–10	l_n min^{-1}	±0.5% Rd* plus ± 0.1% FS**
MFC	CH_4	F-201CV-20K	0.2–10	l_n min^{-1}	±0.5% Rd* plus ± 0.1% FS**
MFC	H_2	F-201CV-20K	0.8–40	l_n min^{-1}	±0.5% Rd* plus ± 0.1% FS**
MFC	N_2	F-201CV-20K	1–50	l_n min^{-1}	±0.5% Rd* plus ± 0.1% FS**

* %Rd= percentage of reading ** %FS= percentage of full scale

The feed of the mass flow controller is strongly dependent on the upstream pressure and the temperature at which the calibration of the specific MFC, according to the manufacturer, was carried out. Since assuring the same upstream pressure at which the calibration was performed is not always achievable, a correction factor (CF_v) can be applied to assure the correct dosage of the feed gas. The correction factor is proportional to the heat capacity $(C_{p,i})$ at constant pressure and density $(D_{n,i})$, where $(i = 1)$ stands for the calibration parameters of the gas and $(i = 2)$ for the experiment parameters, according to (Eq.4-1). [129]

$$CF_v = \frac{C_{p,1} D_{n,1}}{C_{p,2} D_{n,2}} \qquad \text{(Eq. 4-1)}$$

4.1.2.2 Gas Analysis

The gas composition of the inlet and product gas after each reactor was determined with an infrared photometer (AL3000 URAS26) and a thermal conductivity analyzer (AL3000 CALDOS27) from the company ABB. The concentration measurement was always conducted with unpressurized gas, pre-dried at 4°C. Due to the cross-sensitivity of H_2 with the rest of the gases, a correction is made by compensating measured values with internal electronic cross-sensitivity correction.

Table 4-4: Specification of the FTIR and gas analysers

Device	Gas	Range	Unit	Accuracy
URAS26	CO	0–30	vol.-%	± 0.3 %*
	CO_2	0–100	vol.-%	± 1 % *
	CH_4	0–100	vol.-%	± 1 % *
CALDOS27	H_2	0–100	vol.-%	± 2 % *

* % of the measuring span

4.1.2.3 Steam Supply Unit

A number of steam supply units commercially available, but those are cost-intensive. Therefore, a simple combination of a technical magnetic metering pump and a heating hose was chosen.

Deionised water is pumped with the magnetic metering pump series gamma/X (ProMinent GmbH), which allows four different operating pressure levels (4, 7, 10 and 25 bar), depending on the operating pressure of the test plant. In an enclosed heating hose, with a temperature control, the deionised water is vaporised and mixed with the feed gas stream upstream the first heat exchanger. The implementation of the steam supply unit and first tests are well documented in the Master Thesis of Winkler. [130]

Table 4-5: Technical specification of the steam supply unit

Device	Specification	Unit	Range	Accuracy
Magnetic metering pump, gamma/X	max. flow rate	l h^{-1}	2.3	± 0.5%
	max. pressure	bar	25	
	typ		GMXA2504SST10000UA10300DE	
Heating hose	length	m	3.1	
	overall power	W	750	
	oper.temperature	°C	250	
	max. pressure	bar	55	

4.1.2.4 Heat exchangers

The heat exchangers or gas preheaters are based on the same design as the reactors, also made from chromium-nickel austenitic stainless steel (1.4948) (BHDT GmbH). The vessels are filled with the inert HiDur® stoneware balls and the feed gas is heated with the help of an electric heating mat (Horst GmbH) up to 450°C.

4.1.3 Process Control System (PCS)

For the system control and data acquisition, a modular control system Eurotherm Modell 2500 was used. The control of the test plant was carried out using the visualisation program Lookout from National Instruments and communication via OPC-Server and Ethernet. The individual components (flow rates, valves, temperature of the heating sleeves etc.) as well as all data recorded were controlled with the control window (Figure 4-6) and on-site data reading was provided with the display window (Figure 4-5), with safety-relevant control loops. The detailed description has been documented in a Bachelor Thesis (Binderbauer [131]).

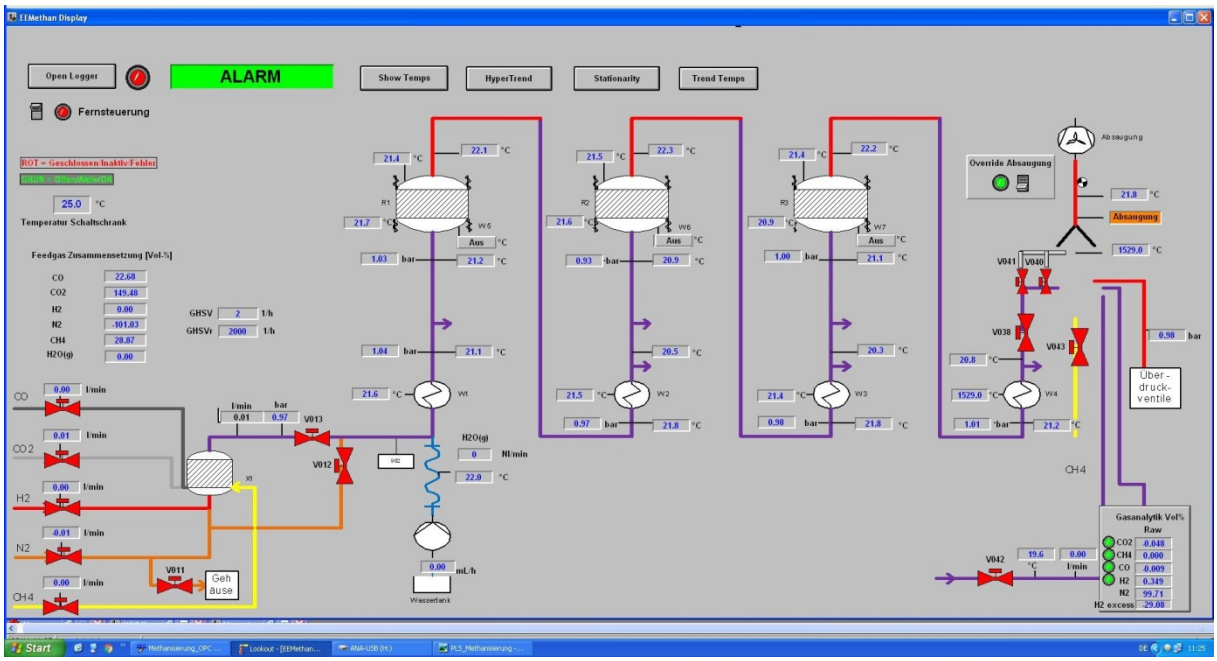

Figure 4-5: Display window of the Lookout visualisation program

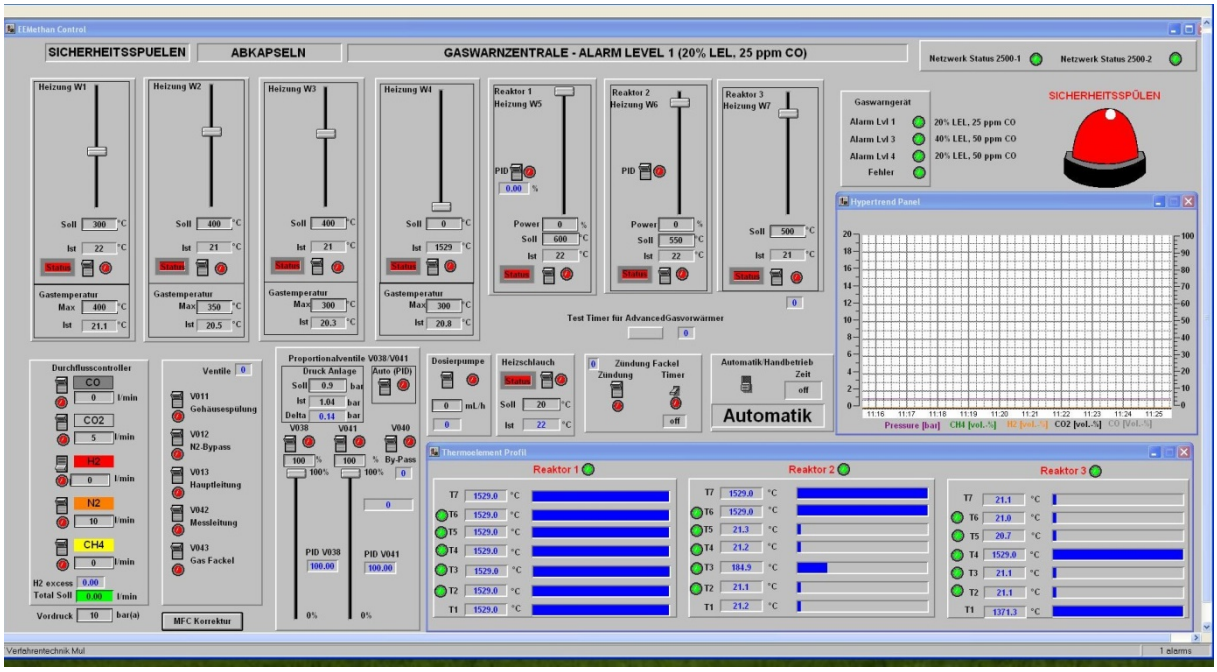

Figure 4-6: Control window of the Lookout visualisation program

4.2 Experimental setup and procedure

The overall objective of the experimental investigations was to determine the behaviour of the methanation of BFG and BOFG composition under different operating conditions.

The influence of N_2 on the methanation process as well as feed gas volume flow rate, pressure and the H_2-surplus variation was examined in 14 experimental series with two different process configurations for the gas mixture of synthetic BFG and BOFG. The initial composition of the respective examined gas (BFG and BOFG) can be seen in Table 4-6. As described in Chapter 3.2, both gases differ from one another in the amount of N_2 concentration, 48 mol.-% for BFG and 28 mol.-% for BOFG, as well as CO concentration, where BOFG contains a double amount of CO as BFG, with approximately equal CO_2 concentration.

Table 4-6: Synthetic BFG and BOFG gas composition

	synthetic gas [molar fraction]			
	CO_2	CO	N_2	H_2
BFG	0.23	0.25	0.48	0.04
BOFG	0.20	0.52	0.28	0

All three reactors connected in series were used in both configurations and for each experimental series. In Table 4-7 can be seen a feed gas composition dependent on the molar fraction of BFG and BOFG, with variation of H_2 surplus. A suitable parameter for the description of the stoichiometry is the ratio (r_{H_2}) of molar H_2 flow and molar flows of CO and CO_2 in the feed gas. r_{H_2} indicates the ratio between the amount of hydrogen used and the required stoichiometric amount according to the Eq. 4-2:

$$r_{H_2} = \frac{n_{H_2}}{4\,n_{CO_2} + 3\,n_{CO}} \qquad \text{(Eq. 4-2)}$$

where r_{H_2} equals to 1 for stoichiometric mixtures, r_{H_2}<1 for sub- and r_{H_2}>1 for over-stoichiometric mixtures, respectively.

Table 4-7: Gas composition of the feed gas for different experimental series #

	Experimental series		Feed gas [molar fraction]			
	#	r_{H_2}	CO	CO_2	N_2	H_2
BFG	1–3	1	0.095	0.088	0.183	0.634
	7–10	1.02	0.094	0.086	0.181	0.639
	7–10	1.04	0.092	0.085	0.179	0.643
	7–10	1.05	0.092	0.085	0.178	0.646
	7–10	1.06	0.091	0.084	0.177	0.648
	7–10	1.09	0.090	0.083	0.173	0.654
	1–3	1.1	0.089	0.082	0.172	0.656
BOFG	4–6	1	0.155	0.060	0.082	0.703
	11–14	1.02	0.153	0.059	0.081	0.707
	11–14	1.04	0.151	0.058	0.080	0.711
	11–14	1.05	0.149	0.058	0.080	0.713
	11–14	1.06	0.148	0.057	0.079	0.715
	11–14	1.09	0.146	0.056	0.077	0.721
	4–6	1.1	0.145	0.056	0.077	0.723

Gas hourly space velocity (GHSV) is one of the parameters used for the characterisation of operational parameters (reactor space loading), defined by the volumetric flow rate (nominal conditions) of the feed gas (Eq. 4-3) on the volume of the catalyst given in (Eq. 4-4). For each experimental series, the volume of the catalyst load remain the same (V_{cat} =0.25 L) for all three reactors.

$$\dot{V}_{input} = \dot{V}_{CO_2} + \dot{V}_{CO} + \dot{V}_{CH_4} + \dot{V}_{H_2} + \dot{V}_{N_2} \quad \text{(Eq. 4-3)}$$

$$GHSV = \frac{\dot{V}_{input}}{V_{cat}} \quad \text{(Eq. 4-4)}$$

For the first evaluation, the influence of N_2/CO/CO_2 gas mixture with the gas composition of synthetic BFG and BOFG with variation of GHSV (2000, 3000, 4000, 5000 and 6000 h^{-1}) and pressure (5, 7.5 and 10 bar) was examined.

Due to the limitations of the mass flow controller dosing, the experiments with BOFG were performed from 3000 – 6000 h^{-1}. The experimental setup (Configuration A) included the isolation of the reactors where the temperature in the reactor was determined by 2 thermocouples. The bottom thermocouple was placed directly at the beginning of the catalyst bed and the second one 20 mm below the reactor top, enabling the variation of the catalyst load. The catalyst implementation with the positioned thermocouples can be seen in Figure 4-7.

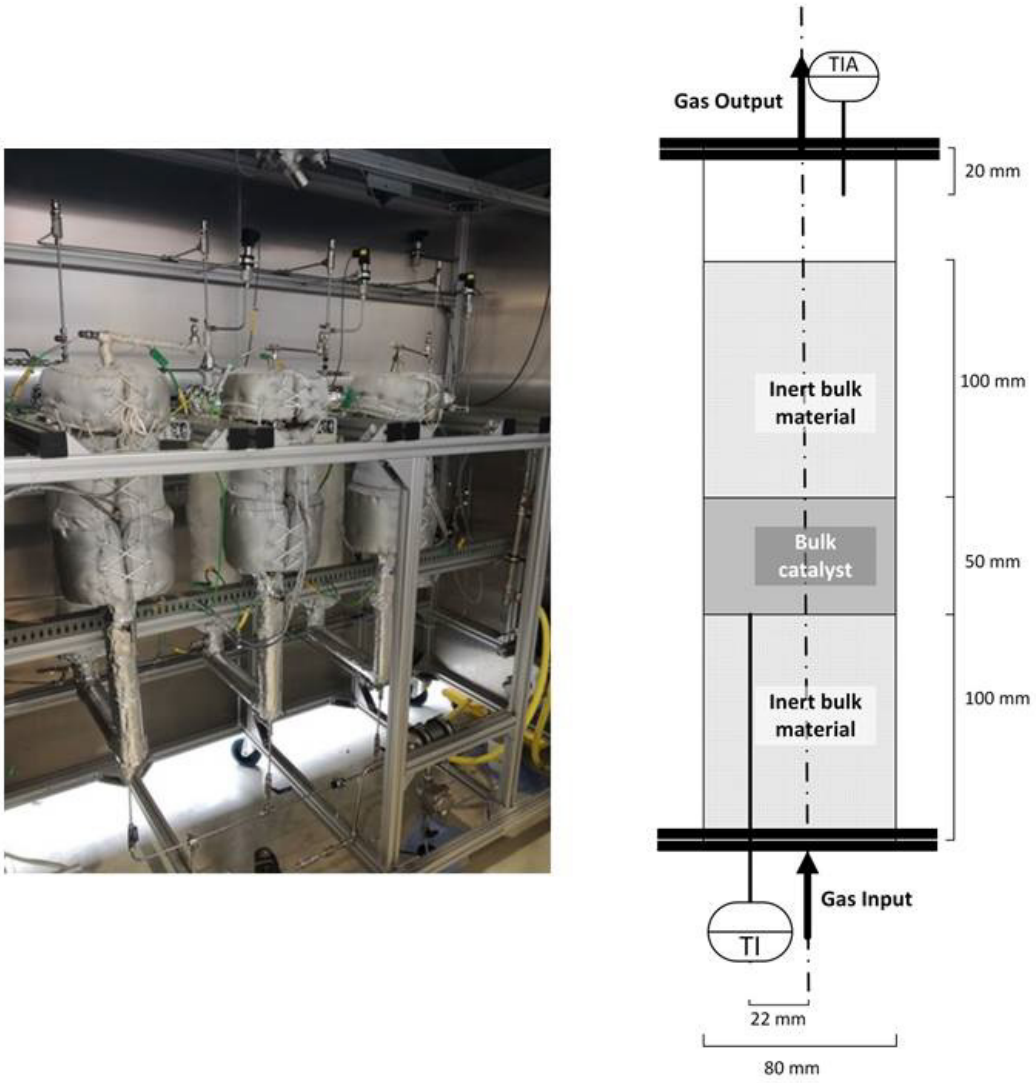

Figure 4-7: Configuration A with catalyst implementation and positioned thermocouples (TI and TIA)

The enhancement of the temperature measurement to multi-thermocouple gave a new understanding of the temperature behaviour within the catalyst bed. Multi-thermocouples with seven measuring points were implemented, with two measuring points in the inert layer (below and above the catalyst zone) and five in the catalyst bed, giving an axial temperature profile of the catalyst (Figure 4-8).

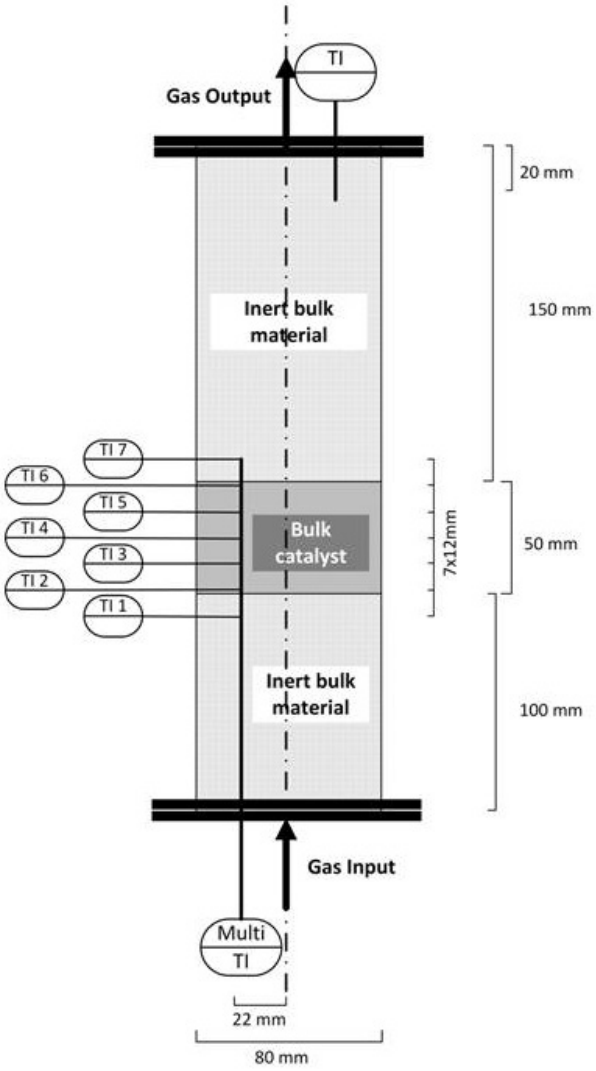

Figure 4-8: Configuration B with catalyst implementation and positioned multi-thermocouple (MTE)

Additionally, the isolation of the reactors was removed and with the new experimental setup (Configuration B) the variation of the H_2-surplus as well as experiments with and without N_2 were performed at two different pressure levels (4 and 7.5 bar). The two chosen pressures coincided with the steel producer´s gas supply system and the influence of the N_2 and H_2 experimental series was limited to GHSV of 4000 h^{-1}.

An overview of performed experimental series with the information regarding experiment parameters (gas composition, pressure, GHSV, volume flow and ratio r_{H_2}) is given in Table 4-8. The GHSV value refers to the total volume flow, entering the first reactor.

Table 4-8: Overview of the experimental series with 2 experimental setup configurations

	Experimental series #	gas composition	P [bar]	GHSV input [h^{-1}]	$\dot{V}$ [l_n min^{-1}]	r_{H_2}
Configuration A	1	BFG	5	2000–6000	8.5–25.0	1 & 1.1
	2	BFG	7.5	2000–6000	8.5–25.0	1 & 1.1
	3	BFG	10	2000–6000	8.5–25.0	1 & 1.1
	4	BOFG	5	3000–6000	8.5–25.0	1 & 1.1
	5	BOFG	7.5	3000–6000	8.5–25.0	1 & 1.1
	6	BOFG	10	3000–6000	8.5–25.0	1 & 1.1
Configuration B	7	BFG	4	4000; 5000	16.7–21.0	1; 1.02; 1.04; 1.05; 1.06; 1.09
	8	BFG	7.5	4000; 5000	16.7–21.0	1; 1.02; 1.04; 1.05; 1.06; 1.09
	9	BFG–N_2	4	3250*; 4200*	13.6–17.5	1; 1.02; 1.04; 1.05; 1.06; 1.09
	10	BFG–N_2	7.5	3250*; 4200*	13.6–17.5	1; 1.02; 1.04; 1.05; 1.06; 1.09
	11	BOFG	4	4000	16.7	1; 1.02; 1.04; 1.05; 1.06; 1.09
	12	BOFG	7.5	4000	16.7	1; 1.02; 1.04; 1.05; 1.06; 1.09
	13	BOFG–N_2	4	3690*	15.4	1; 1.02; 1.04; 1.05; 1.06; 1.09
	14	BOFG–N_2	7.5	3690*	15.4	1; 1.02; 1.04; 1.05; 1.06; 1.09

*** ±50 GHSV input variation due to the MFC dosage limitation**
 # Number of the experimental series

4.2.1 Calculations with respect to feed and product gas

In chemical reaction engineering the conversion, yield and a combination of both – the selectivity, describe the progress of the reaction in a system. Conversion describes a share of the converted reactant, whereas yield gives information about the formed product from the reactant. [132,133]

Since the data screening of the process during the experiment enables only the measurements of the dry gases (y_{ji}), the water content had to be balanced. The balancing of the wet product gas as well conversion, yield and selectivity and additionally the heating value, was calculated with the Wolfram Mathematica 11 software (Appendix C). Molarity n_{ij} of reactants ($i = 1$) and products ($i = 2$) was calculated from the molar flow ($\dot{n}_i$) and wet gas composition (x_{ij}) for each component (j):

$$n_{ij} = \dot{n}_i x_{ij} \quad \text{(Eq. 4-5)}$$

$$x_{ij} = y_{ij}(1 - x_{i\,H_2O}) \quad \text{(Eq. 4-6)}$$

The conversion of the overall process (UCO_x) and per reactant (UCO or UCO_2) was calculated according to (Eq. 4-7)–(Eq. 4-9):

$$UCO_x = \frac{(n_{CO}+n_{CO_2})_1 - (n_{CO}+n_{CO_2})_2}{(n_{CO}+n_{CO_2})_1} \quad \text{(Eq. 4-7)}$$

$$UCO = \frac{(n_{CO})_1 - (n_{CO})_2}{(n_{CO})_1} \quad \text{(Eq. 4-8)}$$

$$UCO_2 = \frac{(n_{CO_2})_1 - (n_{CO_2})_2}{(n_{CO_2})_1} \quad \text{(Eq. 4-9)}$$

Methane yield and selectivity were given according to (Eq. 4-10) and (Eq. 4-11)

$$Y_{CH_4} = \frac{n_{CH_4}}{(n_{CO}+n_{CO_2})_1} \quad \text{(Eq. 4-10)}$$

$$S_{CH_4} = \frac{n_{CH_4}}{(n_{CO}+n_{CO_2})_1 - (n_{CO}+n_{CO_2})_2} \quad \text{(Eq. 4-11)}$$

The wet gas was balanced according to (Eq. 4-6) for each component, and the molar flow of the product after each reactor, as well as water concentration, was calculated with mathematical equalization of the equations for each atom balancing (C= carbon (Eq. 4-13), H=hydrogen (Eq. 4-14) and O=oxygen (Eq. 4-15)) and the sum of the reactant and product wet gas composition x_{ij}. Since the quantity determination of the carbon deposit was not possible, molar flow $\dot{n}_3$ was added as an unknown variable.

$$CBl: \quad \dot{n}_1(x_{1_{CO}} + x_{1_{CO_2}} + x_{1_{CH_4}}) = \dot{n}_2(x_{2_{CO}} + x_{2_{CO_2}} + x_{2_{CH_4}}) + \dot{n}_3 \quad \text{(Eq. 4-13)}$$

$$HBl: \quad \dot{n}_1(2\,x_{1_{H_2}} + 2x_{1_{H_2O}} + 4\,x_{1_{CH_4}}) = \dot{n}_2(2\,x_{2_{H_2}} + 2\,x_{2_{H_2O}} + 4\,x_{2_{CH_4}}) \qquad \text{(Eq. 4-14)}$$

$$OBl: \quad \dot{n}_1(x_{1_{CO}} + 2\,x_{1_{CO_2}} + x_{1_{H_2O}}) = \dot{n}_2(x_{2_{CO}} + 2\,x_{2_{CO_2}} + x_{2_{H_2O}}) \qquad \text{(Eq. 4-15)}$$

Higher (HHV) and lower heating value (LHV) of the product gas were calculated (in the example, for (HHV) according to the Eq. 4-16:

$$HHV = \; y_{2_{CO}}\,HHV_{CO} + y_{2_{CH_4}}\,HHV_{CH_4} + y_{2_{H_2}}HHV_{H_2} + y_{CO_2}\,HHV_{CO_2} + y_{2_{N_2}}\,HHV_{N_2} \qquad \text{(Eq. 4-16)}$$

Table 4-9*: HHV* and *LHV* for each gas component, taken from [134]

		CO	CH_4	H_2	CO_2	N_2
HHV	[kJ mol^{-1}]	283	890.8	285.8	0	0
	[MJ Nm^{-3}]	12.6	39.7	12.8	0	0
LHV	[kJ mol^{-1}]	283	802.3	241,8	0	0
	[MJ Nm^{-3}]	12.6	35.8	10.79	0	0

The mean reactor temperature for each reactor stage (R1-R3) was determined as an arithmetic mean temperature from the measuring points (Eq. 4-16). For Configuration A by two thermocouples and Configuration B with the multi-thermocouple determined five measuring points in catalyst bed for positions 2-6.

$$T_{mean} = \frac{1}{n}\sum_{i=1}^{n} T_i \qquad \text{(Eq. 4-16)}$$

To incorporate the dosing accuracy of the mass flow controllers and measuring error of the gas analysis for each component, as well as the resulting balancing of N_2 concentration and consequently CO_x conversion calculations, the Gaussian propagation of uncertainty for independent quantities was applied (Eq. 4-17). u_y represents the standard deviation of the function y with the independent input quantities x_1, x_2, etc. with corresponding uncertainties u_1. For the calculation of the uncertainties of the experimental results, a Matlab software script, created at the VTiU (DI Martin Peham), was used (Appendix D).

$$u_y = \sqrt{(\frac{\partial y}{\partial x_1}u_1)^2 + (\frac{\partial y}{\partial x_2}u_2)^2 + \cdots} \qquad \text{(Eq. 4-17)}$$

4.3 Experimental results

4.3.1 Configuration A: methanation of BFG and BOFG with pressure and GHSV variation.

In Figure 4-9, achieved CO_x conversion rates for each reactor at different pressures and GHSV variation can be seen for BFG composition with 10% H_2-surplus in the feed gas, demonstrating the influence of the process conditions, pressure and GHSV. The mean reactor temperature (right y-axis) represents the average temperature of the two thermocouples. The conversion increases steadily between the reactor stages from R1 to R3 at each set-point (with the exception at GHSV= 2000 h^{-1}). With increasing GHSV the conversion decreases in each R1, as an example, at a pressure of 5 bar from 83.2% (2000 h^{-1}) to 58.1% (6000 h^{-1}). The decreased conversion is a result of the increased mean reactor temperature due to more released reaction heat caused by the higher amount of the reactive gas. In the case of 5 bar in R1, the mean temperatures rises in R1, from 350°C for 2000 h^{-1} and to 440°C for 6000 h^{-1}. The same trend is evident at pressures of 7.5 and 10 bar. Considerable reaction conversion increase can be seen in reactor R2, while only slight increases are observed in R3, and the multi-stage reaction process increasingly compensates for the negative influence of a higher GHSV, which is reflected in end conversions in R3 > 94% at all set-points, with the exception of 2000 h^{-1}. As discussed in Chapter 3.1.2.2.1., high pressures shift equilibrium toward products and conversion increases; for example, in R1 at GHSV 4000 h^{-1}, a conversion of 68.7% at 5 bar is achieved, whereas conversions of up to 72.3% and 75.2% for 7.5 and 10 bar were reached.

The exceptional conversion downstream of R3 in case of 2000 h^{-1} can be attributed to a measurement error of the gas analysis, possibly due to the volume-contracting CO and CO_2 reactions (Chapter 3.1.2.2.1) that result in too low a volume flow of product gas, especially for methanation at higher pressures.

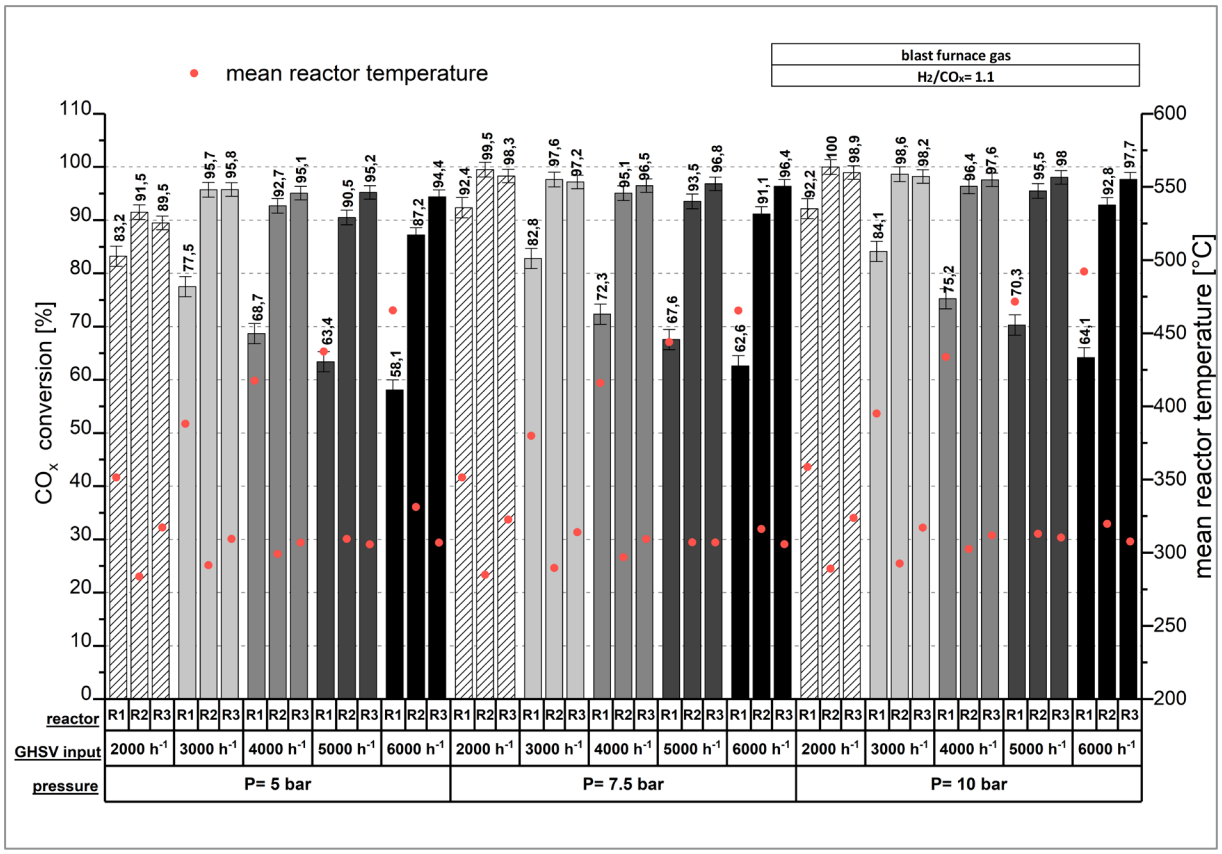

Figure 4-9: Pressure and GHSV variation with 10% H_2-surplus for methanation of BFG (#1 - #3)

A similar conclusion can be drawn for the methanation of BOFG gas with 10% H_2-surplus as shown in Figure 4-10. The conversion increases steadily between the reactor stages from R1 to R3 at each set-point. Also in this case, a substantial CO_x conversion increase can be seen in reactor R2, with only slight increases in R3. The multi-stage reaction process compensates for the negative influence of a higher GHSV, reflected in end conversions in R3 > 95.8% in all set-points. Due to the higher share of CO present in the BOFG compared to BFG, the mean reactor temperatures are 100–200°C higher in R1, thermodynamically hindering the conversions which are 5–10 percent points% lower when compared to the BFG.

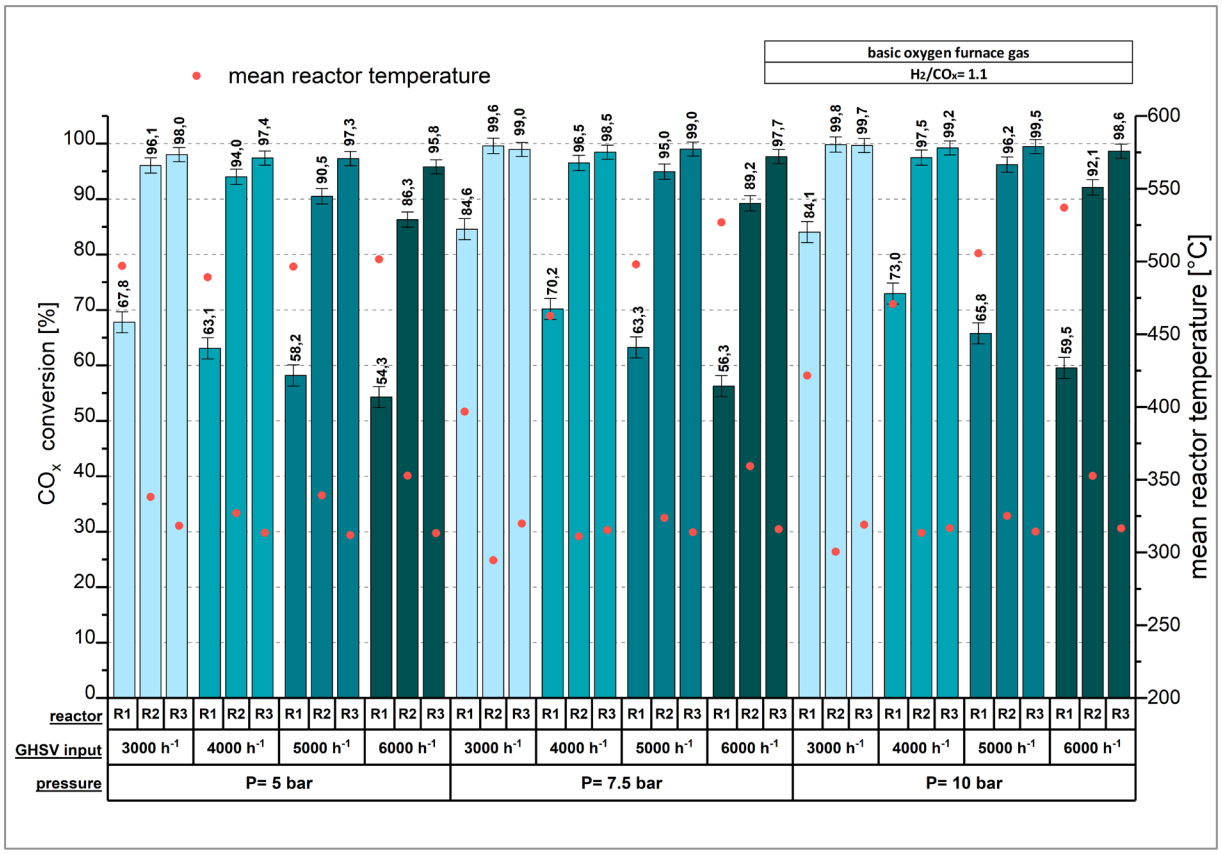

Figure 4-10: Pressure and GHSV variation with 10% H_2-surplus for methanation of BOFG (#4–#6)

First test series with the newly implemented multi-thermocouple for R1 showed a comprehensive picture of the measured temperatures of the catalyst bed. As seen in Figure 4-11 the two-point measurement (Configuration A) did not provide sufficient information on the actual temperature profile, when compared to tests with Configuration B. It has to be mentioned that the results with the same process conditions (with reactor isolation) are applied with red lines. The red dashed line presents a sketch of the expected or assumed temperature profile of Configuration A. Additionally, with the removed isolation of R1 with Configuration B, 150–200°C lower temperatures were achieved. The screened temperature profile over catalyst bed, confirmed the typical temperature profile of an exothermic reaction with the temperature increase reaching a temperature maximum in the first layers of the catalyst followed by its decrease [135]. Further experimental tests were therefore performed with the new Configuration B setup.

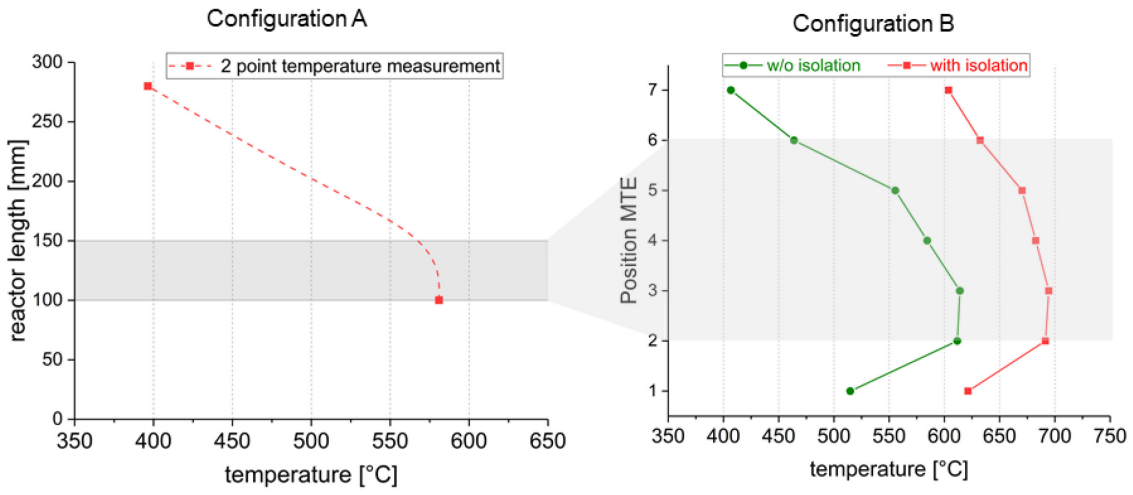

Figure 4-11: Temperature measurement of the catalyst for Configuration A and multi-thermocouple (MTE) measurement of Configuration B with and without isolation with the same applied process parameters, experimental series 4# (r_{H_2}=1.1 for BOFG)

4.3.2 Configuration B: methanation of BFG and BOFG with H_2 and N_2 variation for 4 and 7.5 bar.

To determine the influence of the N_2, experiments with and without N_2 in the feed gas were performed, while the ratio of the reactive components CO, CO_2 and H_2, for each experimental series remained unchanged. Consequently the GHSV for the experiments without N_2 is lower. The results for each experimental series for BFG and BOFG gas compositions as well as H_2- surplus variation can be found in the following subchapter.

4.3.2.1 BFG for experimental series #7–#10

Achieved CO_x conversion rates for each reactor with H_2 surplus variations at 4 and 7.5 bar, with and without N_2 can be seen in Figure 4-12 and Figure 4-13. The mean reactor temperature on the right y-axis was calculated according to the Eq. 4-16 of the measured catalyst bed temperatures (MTE positions 2-6). With the new experimental setup, no substantial CO_x conversion increase is spotted in reactor R2 or R3, compared to the first experiment series (#1–#3), since in R1 between 79.2%–88.9% at 4 bar and 82.4%–90.5% at 7.5 bar of the CO_x is already converted. Better heat management (removal of the isolation) and consequently lower catalyst bed temperatures explain the higher conversions in R1. Furthermore, complete CO_x conversion at 5% H_2-surplus and upwards is achieved in all four experimental series (#7-#10), with and without N_2 in the feed gas. Although the mean reactor temperatures in R1 are approximately 50°C lower with N_2 present, due to additional heat capacity of the inert gas, slightly better conversions are achieved in all three reactors when N_2 is not present in the feed gas. Since the amount of the reactive gas remained the same, the withdrawal of the N_2 in the feed gas resulted in lower GHSV, consequently prolonging the residence time in the reactor. Therefore, N_2 in the feed gas has a substantial influence on the

heating value of the product gas, but a minor one on the conversion of the reactive gas. For example, in R3 at 4 and 7.5 bar with N_2, the higher heating values vary from 19.2–19.8 MJ m^{-3} (r_{H_2}=1.09–1) whereas without N_2, the values are between 32.7 and 37.9 MJ m^{-3} (r_{H_2}=1.09–1). Although with higher H_2-surplus better conversions are achieved, the unconverted H_2 is decreasing the heating value due to its lower volumetric heating value compared to CH_4. When comparing the conversion dependence of the pressure at 4 and 7.5 bar, slightly better final conversions (approx. 3 percent points) are achieved at 7.5 bar. With the H_2-surplus of 5% upwards, complete conversion is reached after two reactor stages. However, the decrease of the temperatures in each reactor stage (R2 and R3) is expected, since the majority of the reactive gas converts in R1, resulting in lower release of the exothermic reaction heat in the following reactor stages.

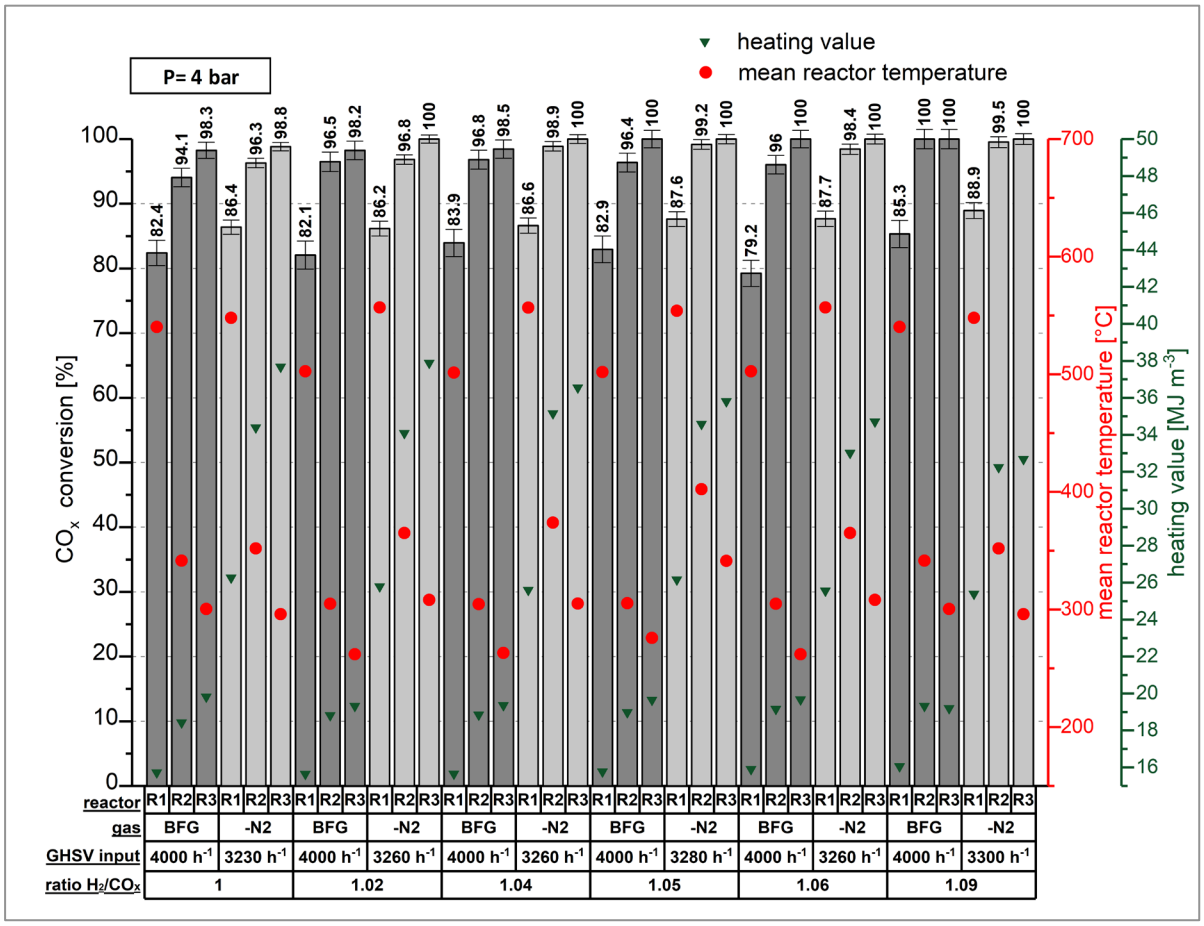

Figure 4-12: Influence of N_2 and H_2 surplus variation for BFG at 4000 h^{-1} and 4 bar (#7, #9)

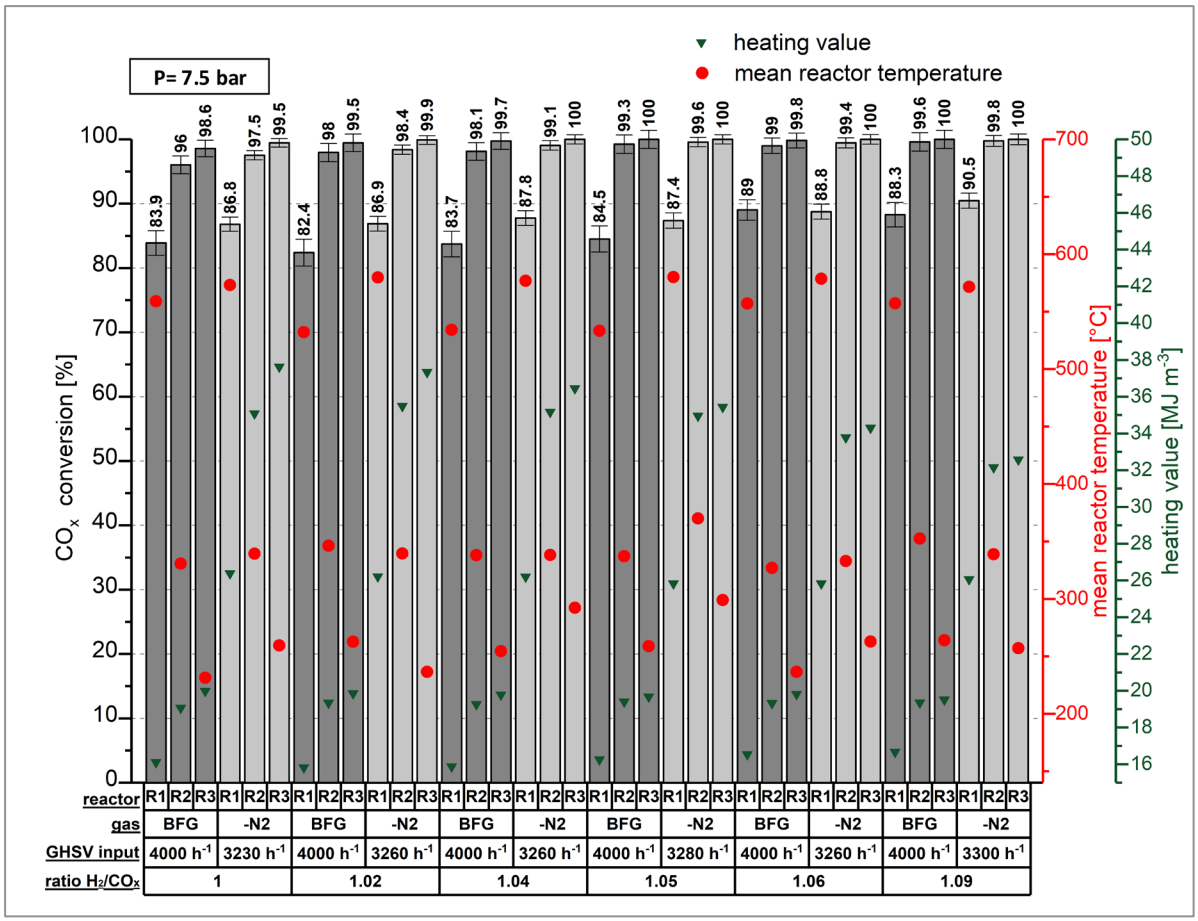

Figure 4-13: Influence of N_2 and H_2 surplus variation for BFG at 4000 h^{-1} and 7.5 bar (#8, #10)

For a detailed insight into the CO (UCO) and CO_2 (UCO_2) conversion, the difference between the CO and CO_2 methanation as well as CH_4 yield (YCH_4) is depicted in Figure 4-14. A complete CO conversion is already achieved in all set-points in R2, because the conversion of CO_2 is inhibited by the CO-methanation, due to the faster adsorption of CO on the catalyst active surface, confirmed also in the early studies of van Herwijnen et al. [67] and Gao et al. [53]. Presence of N_2 is slightly inhibiting the conversion at both r_{H_2}, where the UCO and UCO_2 are 5 percent points higher when N_2 is withdrawn from the feed gas. The higher conversions are a result of the longer residence times of the reactive gas in the reactor.

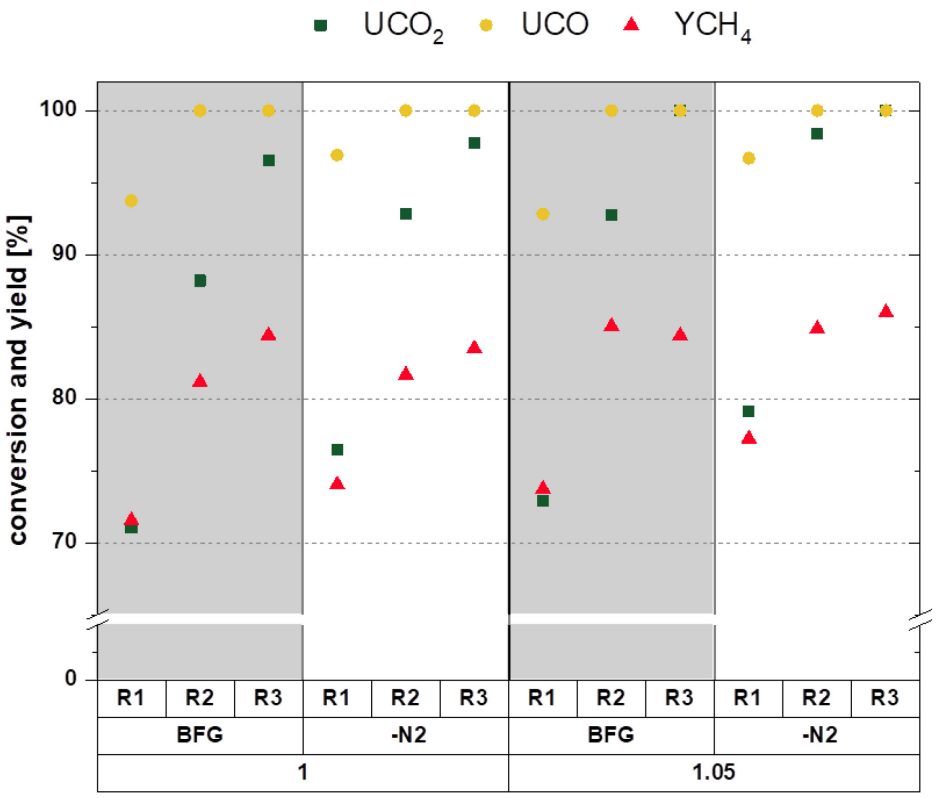

Figure 4-14: Influence of N_2 on UCO, UCO_2 and YCH_4 at surplus variation for BFG at 4000 h^{-1} and 4 bar (#7, #9)

To investigate the influence of the feed gas flow rate (GHSV) experiments were performed at higher GHSV of 5000 h^{-1} with H_2 and N_2 variation at 4 bar for synthetic BFG mixtures as an example (Figure 4-15). When compared to the results of 4000 h^{-1}, complete conversions are not attained in all set-points with N_2 present in the feed, meaning the three reactor stages are not sufficient for the complete CO_x conversion. Due to the higher amount of the reactive gas, the temperature range is between 580 and 600°C in R1 for both cases. In the case of N_2 present in the feed, the temperature is only around 10°C lower. The higher amount of the reactive gas present subsequently results in a greater heat release, due to the exothermic nature of the reaction. Conversions without N_2 in the feed are only around 1 percentage point better. Complete CO_x conversions were achieved without N_2 in the feed from 5% H_2-surplus onwards, but no complete conversion was noted with the N_2 present. This can be attributed to the higher GHSV, resulting in the shorter residence time of the reactive gas in the reactor.

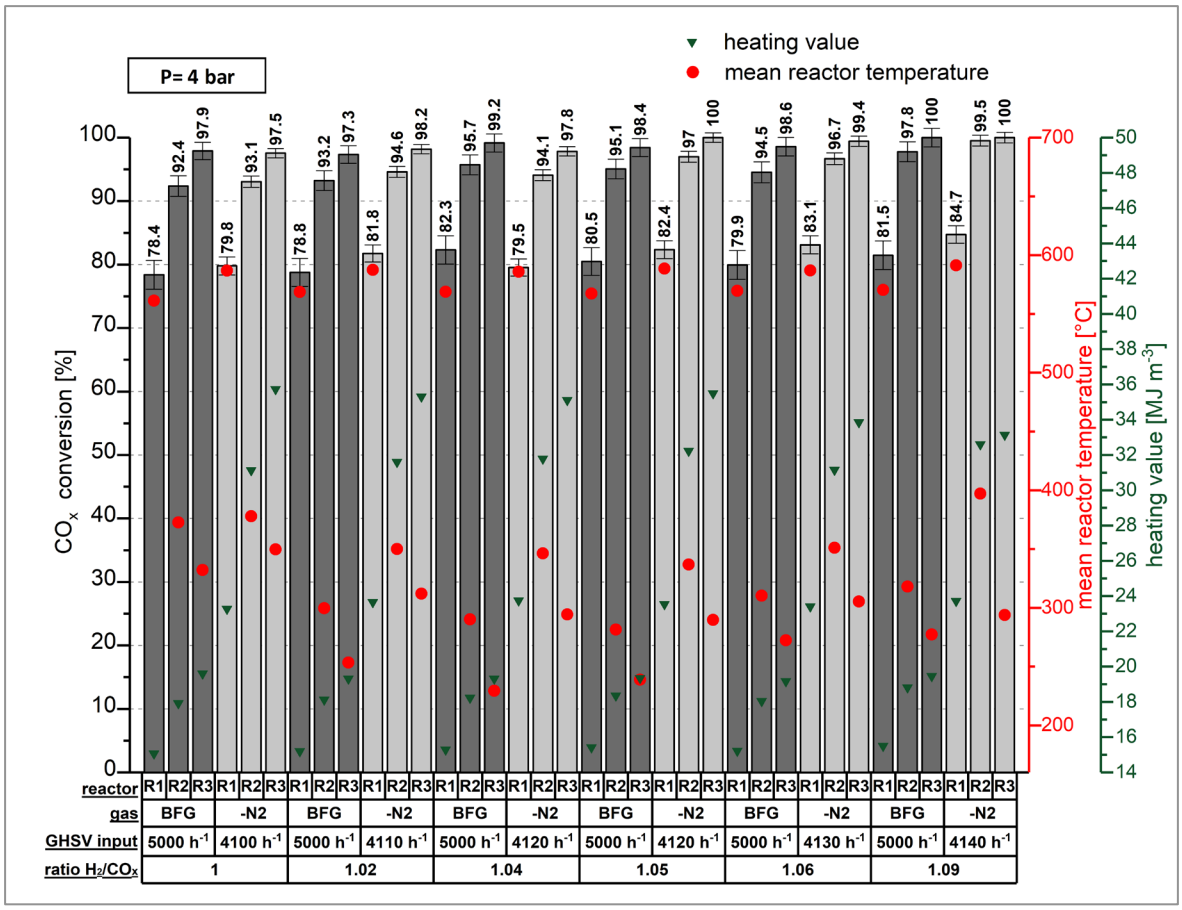

Figure 4-15: Influence of N_2 and H_2-surplus variation for BFG at 5000 h^{-1} and 4 bar (#7, #9)

4.3.2.2 BOFG for experimental series #11–#14

For the methanation of BOFG as well, performed at 4 and 7.5 bar at GHSV 4000 h^{-1} and H_2-surplus variation, shown in Figure 4-16 and Figure 4-17, a similar conclusion can be drawn as for the BFG experimental series. With the new experimental setup, a marginally higher CO_x conversion between R1 and R2 is spotted, but no substantial CO_x conversion increase between reactor R2 or R3, compared to the first experiments (#4- #6)), since in R1 between 77.1% and 84.2% at 4 bar, and 80.0%–85.4% at 7.5 bar of CO_x is already converted. Due to the higher share of the CO in the feed gas, the mean reactor temperatures in R1 are around 600–620°C in all set-points (#11–#14), therefore 50–100°C higher as of BFG methanation (#7-#10). On account of a lower N_2 share in the feed gas (approximately 8%), no noticeable effect of the temperature and, consequently, conversion can be recognized.

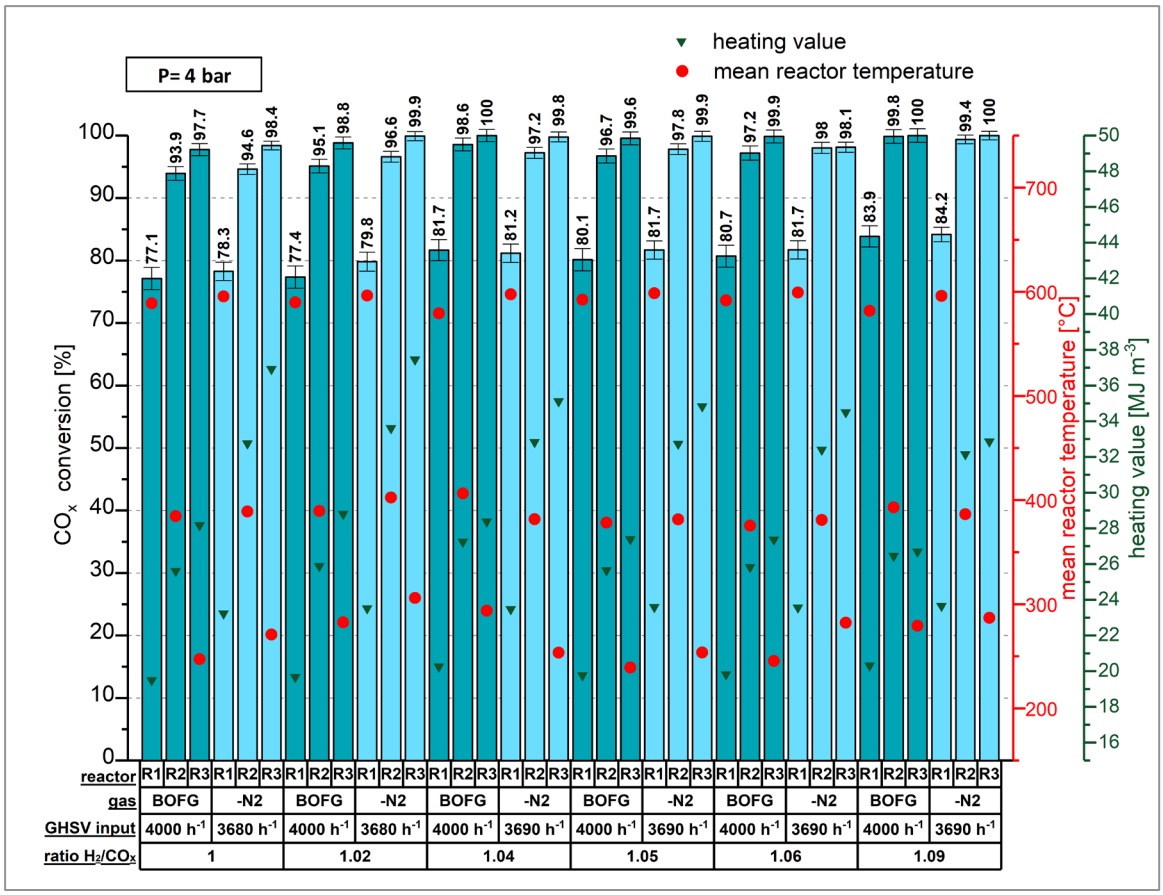

Figure 4-16: Influence of N_2 and H_2 surplus variation for BOFG at 4000 h^{-1} and 4 bar (#11, #13)

Furthermore, a complete CO_x conversion at 4% H_2-surplus is achieved in all four experimental series (#11-#14), with or without N_2 in the feed gas. Therefore, N_2 in the feed gas only has an influence on the heating value of the product gas. For example, in R3 at 4 and 7.5 bar with N_2, the higher heating values vary from 26.7–28.8 MJ m^{-3} (r_{H_2}=1.09–1) whereas without N_2, the values are between 33.2 and 37.7 MJ m^{-3} (r_{H_2}=1.09–1).

In a similar way to the results of BFG, here also the higher H_2 surplus leads to better conversions but the unconverted H_2 decreases the overall heating value of the product gas, due to its lower volumetric heating value compared to CH_4.

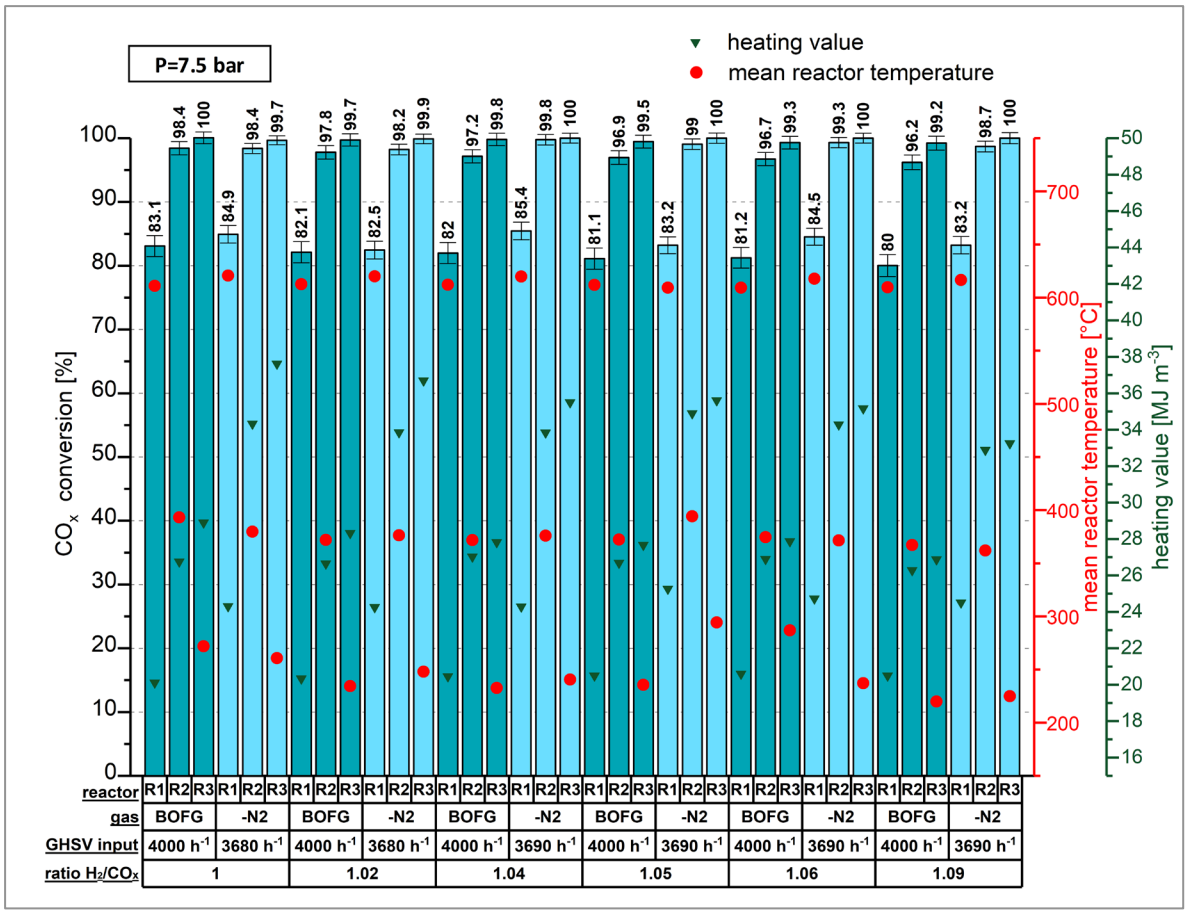

Figure 4-17: Influence of N_2 and H_2 surplus variation for BOFG at 4000 h^{-1} and 7.5 bar (#12, #14)

Similar conclusions as for the BFG can be drawn for BOFG methanation. Figure 4-18 provides the figures of CO (UCO) and CO_2 (UCO_2) conversion as well as CH_4 yield (YCH_4) at stoichiometric and at 5% H_2-surplus. As expected, a complete CO conversion is already achieved in all set-points in R2, whereas the conversion of CO_2 is inhibited by the CO-methanation. Compared to the BFG experiments, CO_2 conversion is approximately 5 percent points lower, which is a result of thermodynamic limitations and caused by higher elevated temperatures in R3. N_2 is inhibiting the conversion at both r_{H_2}, whereas the UCO and UCO_2 are 2–4 percent points higher when N_2 is not present in the feed gas.

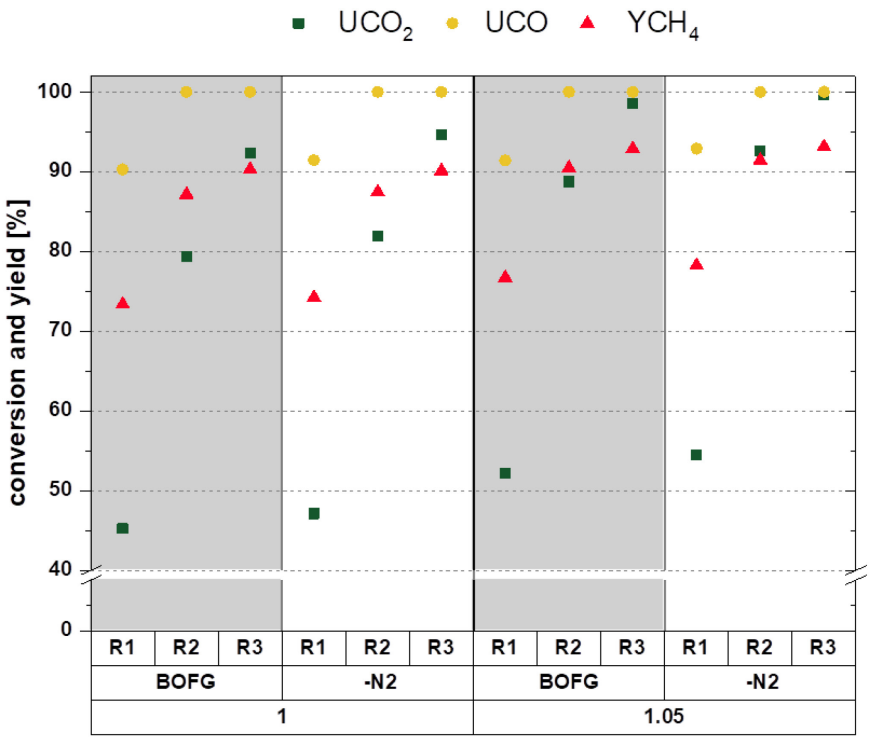

Figure 4-18: Influence of N_2 on UCO, UCO_2 and YCH_4 at surplus variation for BOFG at 4000 h^{-1} and 4 bar (#11, #13)

4.4 Implementation in the integrated steel plant

As indicated in the previous chapter, the experimental tests have shown that the methanation of BFG and BOFG is technically possible without separation of the inert gas N_2. As explained in Chapter 3.3, the obtained results were applied to the possible integration scenarios of the research project “RenewableSteelGases”. [123]

Based on the experimental results an optimum process chain will be presented on example of medium term realistic scenario 9 (Table 4-10), where both BFG and BOFG were used as a carbon source for the methanation. The required H_2 was partly covered by the H_2-rich stream from the biomass gasification (100 MW_{th}) and the remaining part from the water electrolysis. Scenario 9 was defined as methanation of BOFG without N_2 for a complete substitution of the fossil fuels NG and PCI-Coal, the latter used as injection for the blast furnace. When withdrawing the BOFG from the steel production, a shortage of its currently used energy input in the power plant occurs that would consequently result in loss of electric power production. To compensate for the missing amount of BOFG, the BFG with N_2 is enriched via methanation. The required H_2 for the methanation was calculated based on the experimental results for a complete CO_x conversion for BFG (5% surplus) as well BOFG (4% surplus). For the evaluation a H_2 content of 72 vol.-% in the H_2-rich stream [136] from the biomass gasification and a specific power consumption of 5 kWh/Nm^3 H_2 in the electrolyser were assumed. As demonstrated by the methanation experimental tests, the resulting product gas obtained comparable higher heating values (19.4–19.8 MJ m^{-3}) as COG (21 MJ m^{-3}) and more than double that of the unrefined BOFG (8.26 MJ m^{-3}). Therefore, the product gas from the methanation of BFG could substitute for the withdrawal of BOFG and subsequently be sent to the enrichment process in the steel plant. Complete utilisation of the available BOFG and 8% of the available BFG amount would be necessary. Additionally, with the required 901 MW_{el} electrolyser, the complete O_2 demand would be covered. A CO_2 reduction potential of 0.81 million tonnes of CO_{2eq} annually would be possible with a complete substitution of the natural gas demand. However, despite the limitation of the possible gasification power, the necessary renewable electricity to this order of magnitude cannot be provided in the foreseeable future. Nevertheless, based on the selected scenario it provides a good overview of the required renewable energy as well as biomass for the transition of the integrated steel plant towards renewable gas supply.

Table 4-10: Scenario 9 performance overview

Process gas utilisation	100% BOFG and 8% BFG
Electrolyser	901 MW_{el}
Methanation	349 MW_{th} for BOFG and 119 MW_{th} for BFG
Biomass gasification	100 MW_{th}
NG substitution	100%
CO_{2eq}	0.81 Mio.t/a

5 Simulation

In the following chapter the Aspen Plus® V9 simulation program was used for modelling the catalytic methanation with feed gas containing N_2. Different kinetic models from literature have been implemented and the simulation results compared with the experimental data obtained for methanation of BFG and BOFG (Chapter 4). The aim of this work was to prove that kinetic models known from literature can be applied to the methanation with the inert gas N_2 present in the feed gas. In the simulation, the experimental conditions: temperature, pressure and feed gas compositions as well as the reactor dimensions and catalyst specifications are applied in accordance with the laboratory experimental series.

From the kinetic models described in Chapter 3.1.2.2.2, three kinetic models were chosen matching the type of the catalyst as well as the operating conditions. In these models, CO_2 methanation is described as a linear combination of CO-methanation and WGSR. The kinetic models from Kopyscinski and Xu/Froment are often used by various researchers in their simulation based evaluations [137–142]. Since the experimental data conducted in this thesis showed high elevated temperatures (especially in the reactor R1), the kinetic model from Xu/Froment seemed a valid choice due to its origin from “methane steam reforming, methanation and water gas shift reaction” performed at high temperatures. Despite the reaction rate determination at near isothermal conditions from Kopyscinski, this kinetic model was chosen as a comparison. Nevertheless, when modelling three reactors connected in series, a broad temperature and gas concentration range occurs. Therefore the suggested kinetic model from Rönsch, derived for dynamic methanation conditions, seemed promising. As already mentioned, Rönsch et al. adjusted two reaction rates for CO methanation, for a commercial catalyst with 18 wt.-% Ni (from Klose) and for 50 wt.-% Ni (from Zhang). In the present work, the reaction rate for 18 wt.-% Ni (Klose) was chosen, because it corresponds best with the used catalyst with 20 wt.-% Ni.

5.1 Reactor setup with kinetic implementation in Aspen Plus

Two different types of reactors were set up (I and II) in the simulation program flowsheet. All three reactors connected in series were modelled as one-dimensional (1-D) RPlug (plug flow reactor), allowing the implementation of the rate expression (Set-up I) and equilibrium calculation by applying a Gibbs reactor (Set-up II). The kinetic models had to be rewritten in a form such that they could be implemented in the simulation program.

As property method a RKSMHV2 equation of state according to Redlich-Kwong-Soave with mixing rules according to Huron-Vidal was chosen, with $(Vapor)$ as a reacting phase.

In the Set-up I, all three chosen kinetic models applied are of the Langmuir-Hinshelwood-Hougen-Watson (LHHW) approach. In the LHHW approach, the reaction rate (r) as seen in Eq. 5-1 is described as a kinetic factor depending on the adsorption expression and the driving force and is written as follows:

$$r = \frac{[Kinetic\ factor][Driving\ force]}{[Adsorption]} \quad \text{(Eq. 5-1)}$$

For the rate basis a $Cat(wt)$ was chosen as the kinetic expression and the data from the commercial nickel catalyst (Meth134) were implemented in the simulation.

The rate coefficients (k_i) are defined according to the Arrhenius equation (Eq- 5-2),

$$k_i = k_i^0 \exp\left(-\frac{E_{a,i}}{RT}\right) \quad \text{(Eq. 5-2)}$$

with adsorption constants (K_j) for each species (j) according to the van´t Hoff equation:

$$K_j = K_j^0 \exp\left(-\frac{\Delta H_{ads,j}}{RT}\right) \quad \text{(Eq. 5-3)}$$

The kinetic factor for the Arrhenius equation in the simulation program for not specified T_0 was expressed as (Eq. 5-4), where E_a is the activation energy and R the ideal gas constant:

$$Kinetic\ factor = kT^n\ e^{-Ea/RT} \quad \text{(Eq. 5-4)}$$

The driving force was entered after equation (Eq. 5-5) and the adsorption term (Eq. 5-6) with $[C_i]\ basis$ as partial pressures (p_i) of each species and the denominator (m) according to the rate expressions.

$$Driving\ force\ = K_1 \prod p_i^{\alpha i} - K_2 \prod p_j^{\beta j} \quad \text{(Eq. 5-5)}$$

$$Adsorption\ = \{\sum K_i (\prod p_j^{\gamma i})\}^m \quad \text{(Eq. 5-6)}$$

The simulation program required implementation of equilibrium equations and adsorption constants in the following form to estimate their dependence on the temperature:

$$ln\ (K_i) = A_i + \frac{B_i}{T} + C_i \ln(T) + D_i\ T \quad \text{(Eq. 5-7)}$$

Additionally, the temperature in the reactor was specified as the axial temperature profile of the catalyst bed, according to the measured experimental data and the pressure drop as a frictional correlation according to Ergun equation. Since no equilibrium constant for CO methanation (K_{meth}) and WGSR (K_{WGSR}) was provided by Xu/Froment, this data was taken from [82,143].

For the second set up (II), a set of modelling data was performed with Gibbs reactors, since based on the conducted experimental data (Chapter 4), a thermodynamic limitation of the process can be assumed, at least in reactor R1. For the Gibbs reactor, the reactor temperature and the pressure was set according to the obtained experimental data. The experimental test plant enables a screening of the axial temperature profile of the catalyst bed, whereas the simulation of the Gibbs reactor requires a specific temperature. Therefore,

an arithmetic mean temperature of the five temperatures measured in the catalyst bed (MTE 2-6) was determined in accordance with Eq. 5-8.

$$T_{mean} = \frac{1}{n}\sum_{i=1}^{n} T_i \qquad \text{(Eq. 5-8)}$$

The total Gibbs free energy (G_T) of the system was calculated according to Eq. 5-9 [53] :

$$G_T = \sum_{i=1}^{m} n_i \mu_i = \sum_{i=1}^{m} n_i \mu_i^{\Theta} + RT \sum n_i \, ln \frac{f_i}{P^{\Theta}} \qquad \text{(Eq. 5-9)}$$

Where n_i stands for the molarity of species (i), fugacity coefficient (f_i) at standard pressure P^{Θ} and the chemical potential of species (μ_i^{Θ}). [53]

The three chosen kinetic rate expressions as well as the rewritten parameters for the implementation in Aspen Plus can be seen in Table 5-1 and Table 5-2. A detailed kinetic implementation procedure as an example of the Kopycinski kinetic model in the simulation program can be found in the master thesis of Khodier [144].

Table 5-1: Kinetic rate expressions for the three chosen kinetic models from the literature

Author	**Kinetic rate expression**
Xu/Froment 15.2 wt.-% $Ni/MgAl_2O_4$	$r_{CO-Meth.} = -\frac{k_1 p_{H_2}^{-2.5}\left(p_{H_2O} p_{CH_4} - \frac{p_{H_2}^3 p_{CO}}{K_{METH}}\right)}{(DEN)^2}$ $\quad$ $r_{WGSR.} = \frac{k_{WGS} p_{H_2}^{-1}\left(p_{H_2O} p_{CO} - \frac{p_{H_2} p_{CO_2}}{K_{WGS}}\right)}{(DEN)^2}$ $DEN = 1 + K_{CO} p_{CO} + K_{H_2} p_{H_2} + K_{CH_4} p_{CH_4} + K_{H_2O} p_{H_2O} / p_{H_2}$
Kopyscinski 50 wt.-% Ni/Al_2O_3	$r_{CO-Meth.} = \frac{k_1 K_C p_{CO}^{0.5} p_{H_2}^{0.5}}{\left(1 + K_C p_{CO}^{0.5} + K_{OH} p_{H_2O} p_{H_2}^{-0.5}\right)^2}$ $\quad$ $r_{WGSR.} = \frac{k_2 (K_\alpha p_{CO} p_{H_2O} - p_{CO_2} p_{H_2} / K_{eq})}{p_{H_2}^{0.5}\left(1 + K_1 p_{CO}^{0.5} + K_{OH} p_{H_2O} p_{H_2}^{-0.5}\right)^2}$
Rönsch 18 wt-% Ni/Al_2O_3	$r_{CO-Meth.} = -\frac{k_1 K_C K_H^2 p_{CO}^{0.5} p_{H_2} + k_1 K_C K_H^2 p_{CH_4} p_{H_2O} p_{CO}^{-0.5} p_{H_2}^{-2} \frac{1}{K_{METH}}}{\left(1 + K_C p_{CO}^{0.5} + K_H p_{H_2}^{0.5}\right)^3}$ $\quad$ $r_{WGSR.} = \frac{k_{WGS} p_{H_2}^{-1}\left(p_{H_2O} p_{CO} - \frac{p_{H_2} p_{CO_2}}{K_{WGS}}\right)}{(DEN)^2}$ $DEN = 1 + K_{CO} p_{CO} + K_{H_2} p_{H_2} + K_{CH_4} p_{CH_4} + K_{H_2O} p_{H_2O} / p_{H_2}$

Table 5-2: Parameters for the rate and adsorption for the three chosen kinetic models

Kopyscinski/Erbib [57,145]					Xu-Froment [80]					Rönsch [82]				
parameter		**unit**		**Aspen values**	**parameter**		**unit**		**Aspen values**	**parameter**		**unit**		**Aspen values**
$\mathbf{k_1}$	k_1^0	kmol $kg^{-1}_{cat.}s^{-1}$		3.34×10^3	$\mathbf{k_1}$	k_1^0	kmol $Pa^{0,5}$ $kg^{-1}_{cat.}$ s^{-1}		$3{,}711 \times 10^{14}$	$\mathbf{*k_{1= k1* Kc*KH\^2}}$	$*k_1^0$	kmol $kg^{-1}_{cat.}$ s^{-1}		1.98×10^{-6}
	E_{a1}	kJ mol^{-1}		74		E_{a1}	kJ mol^{-1}		240.1		$*E_{a1}$	kJ mol^{-1}		29
$\mathbf{k_2}$	k_2^0	kmol $kg^{-1}_{cat.}$ s^{-1}		9.62×10^{11}	$\mathbf{k_2}$	k_2^0	kmol Pa^{-1} $kg^{-1}_{cat.}$ s^{-1}		6.88×10^5	$\mathbf{k_1}$	k_1^0	kmol $kg^{-1}_{cat.}$ s^{-1}		1.33×10^9
	E_{a2}	kJ mol^{-1}		161.74		E_{a2}	kJ mol^{-1}		67.13		E_{a1}	kJ mol^{-1}		103
$\mathbf{K_1}$			A_1	-23.24	$\mathbf{K_{CO}}$		Pa^{-1}	A_{CO}	-20.92	$\mathbf{K_c}$	K_c^0	$Pa^{-0,5}$		1.83×10^{-6}
			B_1	7355.77				B_{CO}	8497.7		E_{ac}	kJ mol^{-1}		-42
$\mathbf{K_2}$			A_2	-20.49	$\mathbf{K_{H_2}}$		Pa^{-1}	A_{H_2}	-30.42	$\mathbf{K_H}$	K_H^0	$Pa^{-0,5}$		5.06×10^{-5}
			B_2	8731.97				B_{H_2}	9971.13		E_{aH}	kJ mol^{-1}		-16
$\mathbf{K_3}$			A_3	-19.64	$\mathbf{K_{CH_4}}$		Pa^{-1}	A_{CH_4}	-18.83	$\mathbf{k_2}$	k_2^0	kmol $kg^{-1}_{cat.}$ s^{-1}		0.0218
			B_3	781.25				B_{CH_4}	4604.28		E_{a2}	kJ mol^{-1}		62
$\mathbf{K_4}$			A_4	-13.208	$\mathbf{K_{H_2O}}$		-	A_{H_2O}	12.084	$\mathbf{K_{CO}}$		Pa^{-1}	A_{CO}	-20.92
			B_4	-4400				B_{H_2O}	-10666.3				B_{CO}	8497.71
					$\mathbf{*K_{meth}}$		Pa^2	A_1	53.162	$\mathbf{K_{H_2}}$		Pa^{-1}	A_{H_2}	-30.42
								B_1	-26830				B_{H_2}	9971.13
					$\mathbf{*K_{WGSR}}$		-	A_2	4.063	$\mathbf{K_{CH_4}}$		Pa^{-1}	A_{CH_4}	-18.83
								B_2	-4400				B_{CH_4}	4604.28
										$\mathbf{K_{H_2O}}$		-	A_{H_2O}	12.08
													B_{H_2O}	-10666.35
										$\mathbf{*K_{meth}}$		Pa^2	A_1	53.162
													B_1	-26830
										$\mathbf{*K_{WGSR}}$		-	A_2	4.063
													B_2	-4400

* **data taken from [82,143]**

5.2 Simulation results

Due to the large amount of data from the conducted experiments and simulations the results will be presented as a representative example of stoichiometric r_{H_2} at the pressure of 4 bar, and input GHSV of 4000 h^{-1} with N_2 and GHSV of 3230 h^{-1} without N_2 for BFG, and GHSV of 3680 h^{-1} for BOFG.

5.2.1 Simulation results for BFG composition

A detailed temperature profile of the catalyst bed for the three reactors connected in series (R1-R3) is shown in Figure 5-1, with feed gas entering the catalyst bed at multi-thermocouple (MTE) at position 1 and leaving it at position 7.

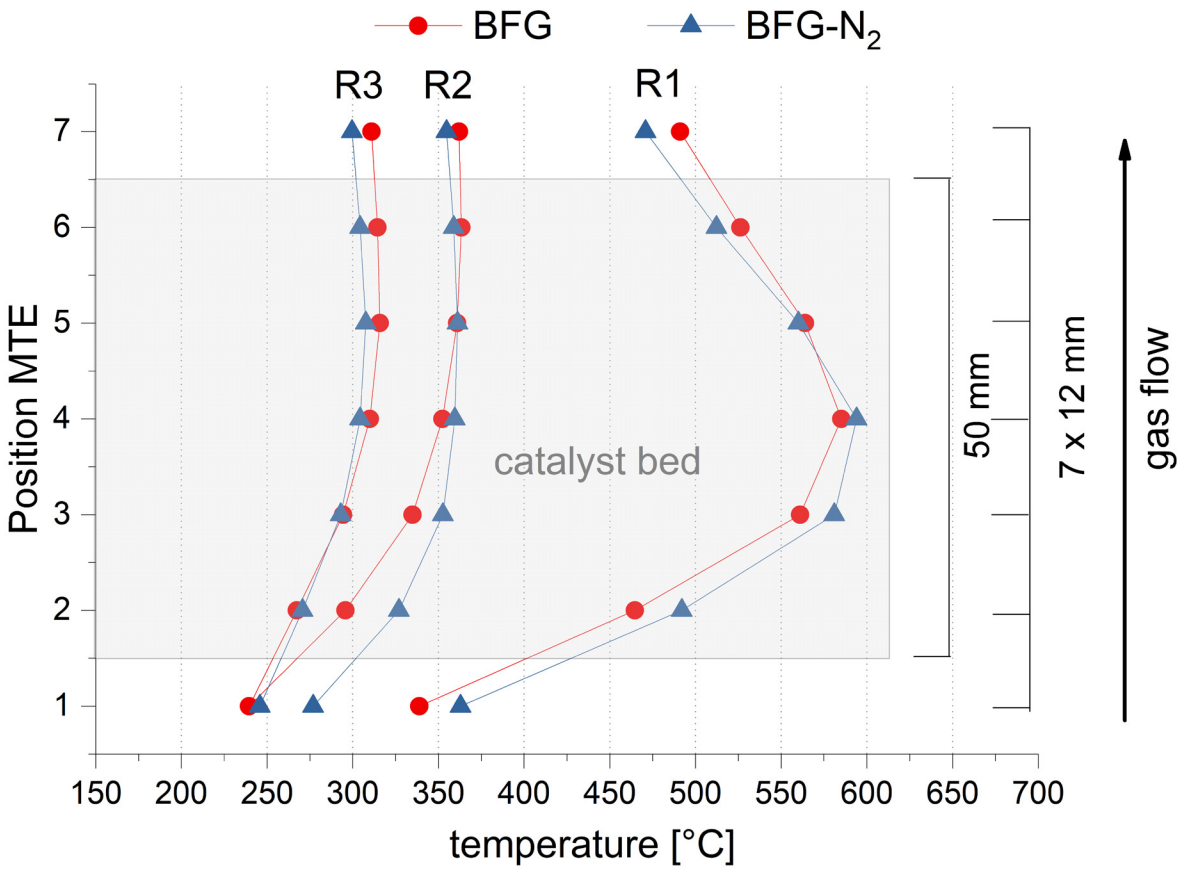

Figure 5-1: Experimentally determined axial temperature profile of the catalyst bed for three reactors (R1-R3) at feed gas compositions for BFG and BFG-N_2

The released reaction heat causes a temperature increase in the first reactor (R1), where in the case of the N_2 withdrawal (BFG-N_2) 10-30°C higher temperatures were measured in the first layers of the catalyst bed (Position MTE: 2-4). However, at MTE positions 5-7, the measured temperature for BFG is higher than for BFG-N_2. At the same time, the temperature elevation in the catalyst bed for R1 is approximately 140°C (from 460°C (position 2) up to

600°C (position 4), developing a temperature peak in position 4. The measured temperature profile is typical for exothermic reactions in fixed-bed reactors. The temperature elevation in the following two reactors (R2 and R3) is accordingly lower when compared to the R1 due to less released reaction heat (Chapter 4.3.2.1), with a modest temperature elevation between 25–40°C. The experimentally determined temperature profile of the catalyst bed was implemented in each reactor R1-R3 accordingly, for all three chosen kinetic models. In Figure 5-2, the results of the implemented kinetic models are presented.

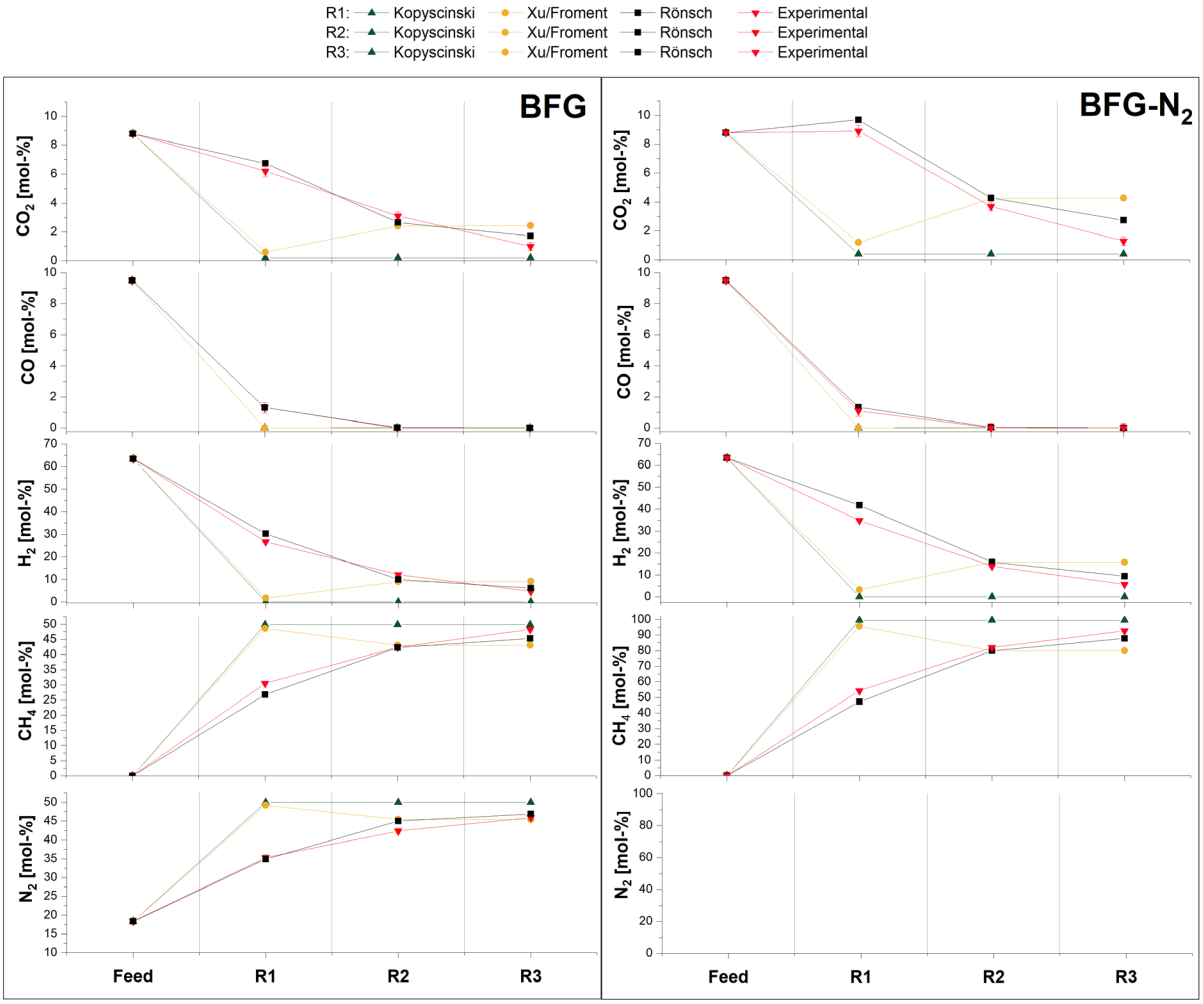

Figure 5-2: Gas composition (dry) of simulation results compared with the experimental data for BFG ($GHSV_{input}$= 4000h^{-1}) and BFG-N_2 ($GHSV_{input}$= 3230h^{-1}) at stoichiometric ratio (r_{H_2}=1.0) and P=4 bar

On the y-axis, the change of the gas concentrations for each species in relation to reactor stage (R1-R3) for the three kinetic models are compared with experimental data. It can be seen that the kinetic model from Kopyscinski overestimates the conversion of CO as well CO_2 in both cases BFG and BFG-N_2, already resulting in complete CO_x conversion in reactor R1. The reason is that for the applied temperatures (460-600°C in R1) it does not assume the reverse reaction (methane reforming) that occurs at high elevated temperatures. This confirms the observations from Rönsch et al. [82] and Neubert et al. [138] for their

calculations based on the Kopyscinski model. On the other hand, the proposed reaction rates from Xu/Froment also overestimate the complete conversion of CO_x in reactor R1. In reactor R2, a reverse reaction (methane reforming) occurs, resulting in a CO_2 concentration increase. As for the third reactor R3, no conversion occurs, since the reaction rate is too slow and the model remains inactive at temperatures between 260-300°C. This was expected since the reaction rate from Xu/Froment was determined at higher elevated temperatures (300-400°C). However, a similar trend as in the experiments and good fit of the gas composition for each reactor stage is achieved with the kinetic model from Rönsch. In the case of BFG-N_2 it is clear that at the high elevated temperatures in R1 (maximal measured temperature 600°C) a WGSR reaction starts to dominate, resulting in an increase of CO_2 concentration. Thus, the CO_2 concentration in all three reactor stages is slightly overestimated with the kinetic model of Rönsch. When comparing the simulation results of the Rönsch kinetic model for BFG and BFG-N_2, no substantial deviation can be seen. It can be concluded, that the kinetic model of Rönsch also predicts the conversions correctly in the case of present N_2. Due to three reactor stages in series, a complete CO_x conversion is achieved in both cases (BFG and BFG-N_2) downstream of R3, which also coincides well with the experimental data.

In order to further investigate the overestimation of the CO_2 concentration in the Rönsch kinetic model, a thermodynamic limitation in R1 was assumed. Thus, for the same feed gas concentrations a Gibbs reactor (with Gibbs free minimisation method) was applied for R1-R3. For this purpose, an arithmetic mean temperature of the catalyst bed was assumed in each reactor for a defined pressure (Eq. 5-8). When applying the arithmetic mean temperature (T_{mean}) of the five measured points of the reactor bed (R1-R3) in the simulation, no proper fit between measured and simulated data was attained. This led to the conclusion that the arithmetic mean temperature was not appropriate as a simulation parameter, resulting mostly in calculated equilibrium concentrations that were obviously too low (as example showed in Figure 5-3 for R1). For that reason, a sensitivity analysis with a temperature variation was conducted for each reactor stage.

The reactor temperature was varied in 1°C steps, starting from the mean reactor temperature (T_{mean}). The solid lines parallel to the x-axis in Figure 5-3 represent experimentally determined concentrations for each gas component, with a deviation band symbolizing the measurement error. The dotted lines are the calculated concentrations of each gas component for a given temperature (x-axis) according to (Eq.5-9). An approximation of the adapted temperature ($T_{adapted}$) was set by best accordance with the experimental data.

It can be seen that the applied arithmetic mean temperature derived from the measured data for R1 in the case of BFG was 43°C too high and in the case of BFG-N_2, 70°C.

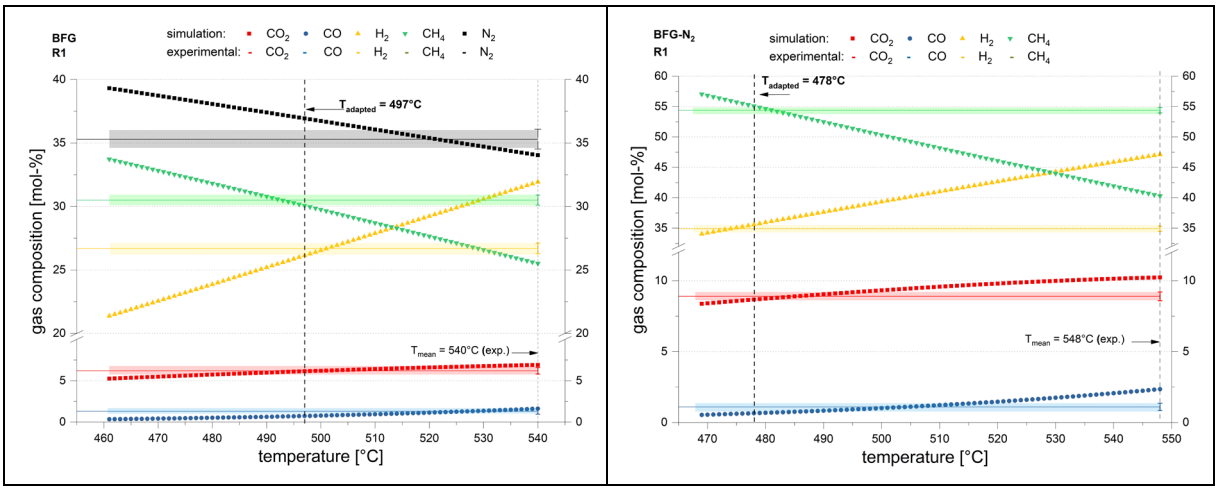

Figure 5-3: Comparison between experimental data and adapted temperature ($T_{adapted}$) for the simulation for BFG and BFG-N_2, r_{H_2}=1.0 for product gas in first reactor stage (R1)

The same procedure was used for the following R2 (Figure 5-4) and R3 (Figure 5-5). The temperature elevation over the catalyst bed in R2 was accordingly lower, but it resulted in the case of BFG at 27°C higher adapted temperature, whereas in the case of BFG-N_2, a 7°C lower temperature showed a better fit with accordance to experimental data.

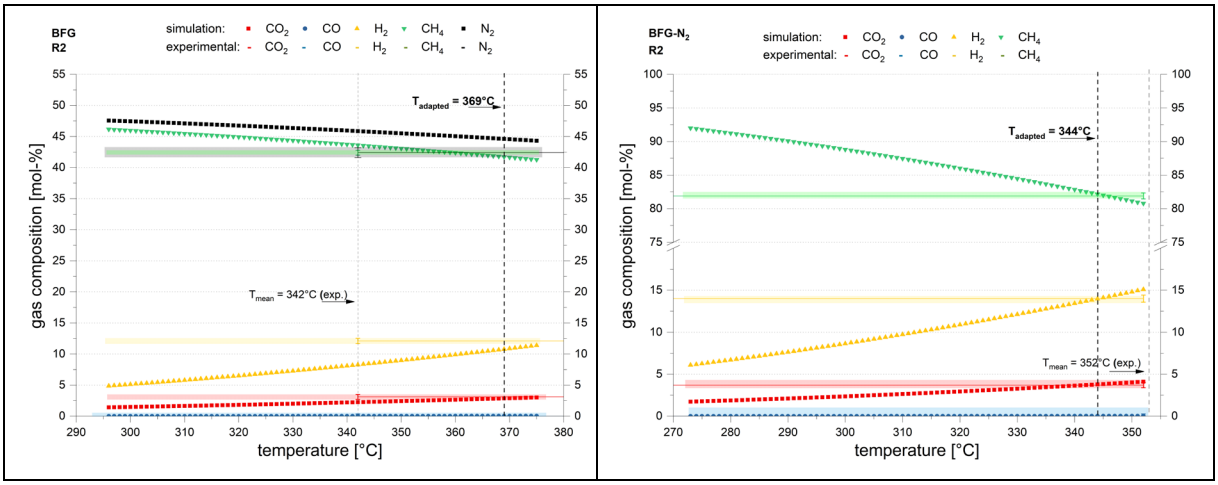

Figure 5-4: Comparison between experimental data and adapted temperature ($T_{adapted}$) for the simulation of BFG and BFG-N_2, r_{H_2}=1.0 for product gas in second reactor stage (R2)

As for reactor R3, seen in Figure 5-5, no temperature adaptation was necessary for BFG, since the implementation of T_{mean} provided suitable results. In the case of BFG-N_2, 27°C lower temperature compared to the applied arithmetic mean temperature corresponded well with the experimental data.

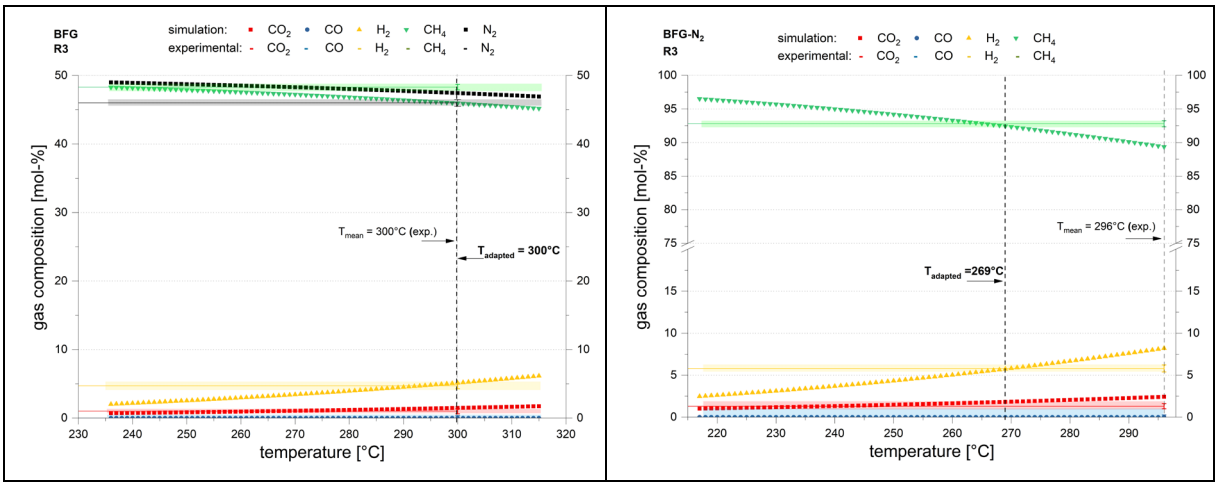

Figure 5-5: Comparison between experimental data and adapted temperature ($T_{adapted}$) for the simulation of BFG and BFG-N_2, r_{H_2}=1.0 for product gas in third reactor stage (R3)

A closer look at the screened temperature profile (Figure 5-6) shows a good correspondence to the adapted temperature, $T_{adapted}$, for both gas mixtures (BFG, BFG-N_2) in all three reactor stages R1-R3, with the measured temperature of the MTE on position 7. Position 7 is close to the outlet temperatures of the reactors. The small deviations up to 11°C (with the exception of BFG-N_2 in R3) can be caused due to the position of the multi-thermocouple, since the thermocouple was positioned 22 mm excentric from the reactor middle axis (Figure 4-8). The exception of BFG-N_2 in R3 can be attributed to the fact that in this experiment no steady state condition was reached in the reactor.

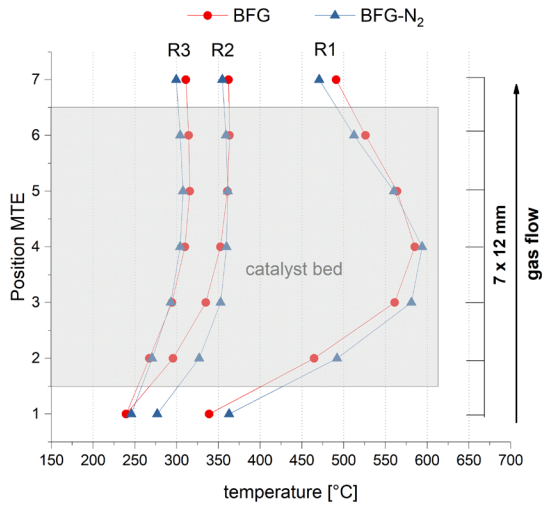

	R1		R2		R3	
	BFG	BFG-N_2	BFG	BFG-N_2	BFG	BFG-N_2
$T_{adapted}$	497	478	369	344	300	269
T_{mean}	540	548	342	352	300	296
7	491	471	362	355	311	300
6	526	512	363	359	315	304
5	564	560	361	361	316	308
4	585	594	352	360	310	304
3	561	581	335	353	294	293
2	465	492	296	327	267	271
1	339	363	240	277	240	246

Figure 5-6: Experimentally determined axial temperature profile of the catalyst bed, with arithmetic mean (T_{mean}) and adapted ($T_{adapted}$) temperature for three reactors (R1-R3) at feed gas compositions for BFG and BFG-N_2

The adapted temperatures for R1-R3 were applied in the simulation. As shown in the Figure 5-7, the experimental data are now in better accordance with the computed data from the

Gibbs reactor. From the obtained data, a thermodynamic limitation in the three reactor stages can be assumed, especially in reactor R1.

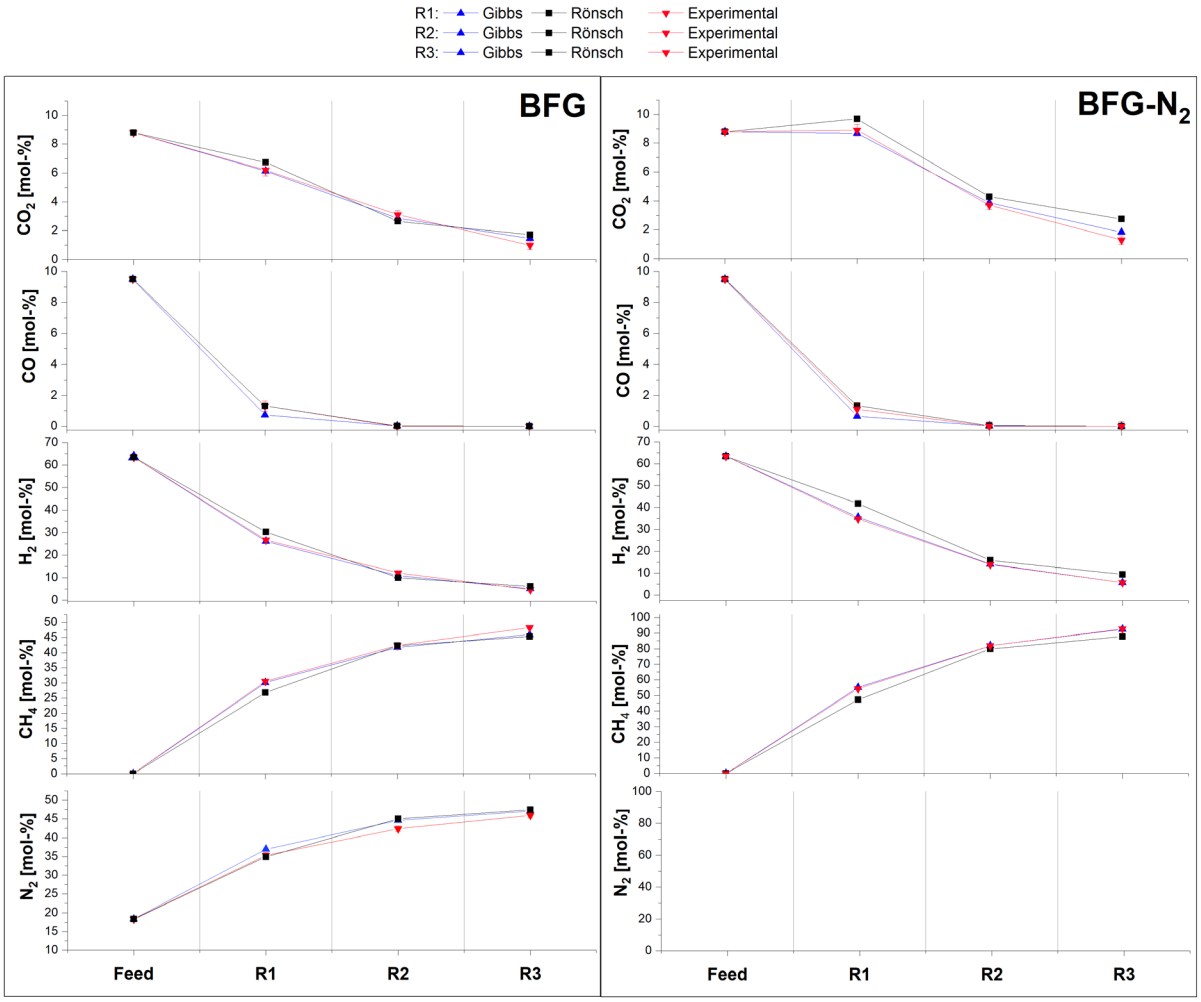

Figure 5-7: Gas composition (dry) of simulation results for kinetic model of Rönsch and Gibbs reactor (with $T_{adapted}$ in R1) compared with the experimental data for BFG ($GHSV_{input}$=4000h^{-1}) and BFG-N_2 ($GHSV_{input}$= 3230h^{-1}) at stoichiometric ratio (r_{H_2}=1) and P=4 bar

5.2.2 Simulation results for BOFG composition

A similar conclusion as for BFG can be drawn for BOFG. The released reaction heat causes the temperature increase, particularly in the first reactor (R1), both for BOFG and for BOFG-N_2, but with a smaller deviation, as for BFG, between the cases with and without N_2, as the amount of N_2 in the feed gas was only 8.2%. Up to 10°C higher temperatures were measured in the first layers of the catalyst bed (Position MTE: 2-4) for BOFG-N_2. At the same time, the temperature elevation in the catalyst bed for R1 is approximately 140°C (on example of BOFG-N_2 from 510°C (position 2) up to 650°C (position 4)). When compared to the BFG, the higher elevated temperatures in reactor R1 are due to the higher share of the component CO. Nevertheless, the temperature elevation in the following two reactors (R2 and R3) is accordingly lower when compared to R1 due to less released reaction heat (Chapter 4.3.2.2).

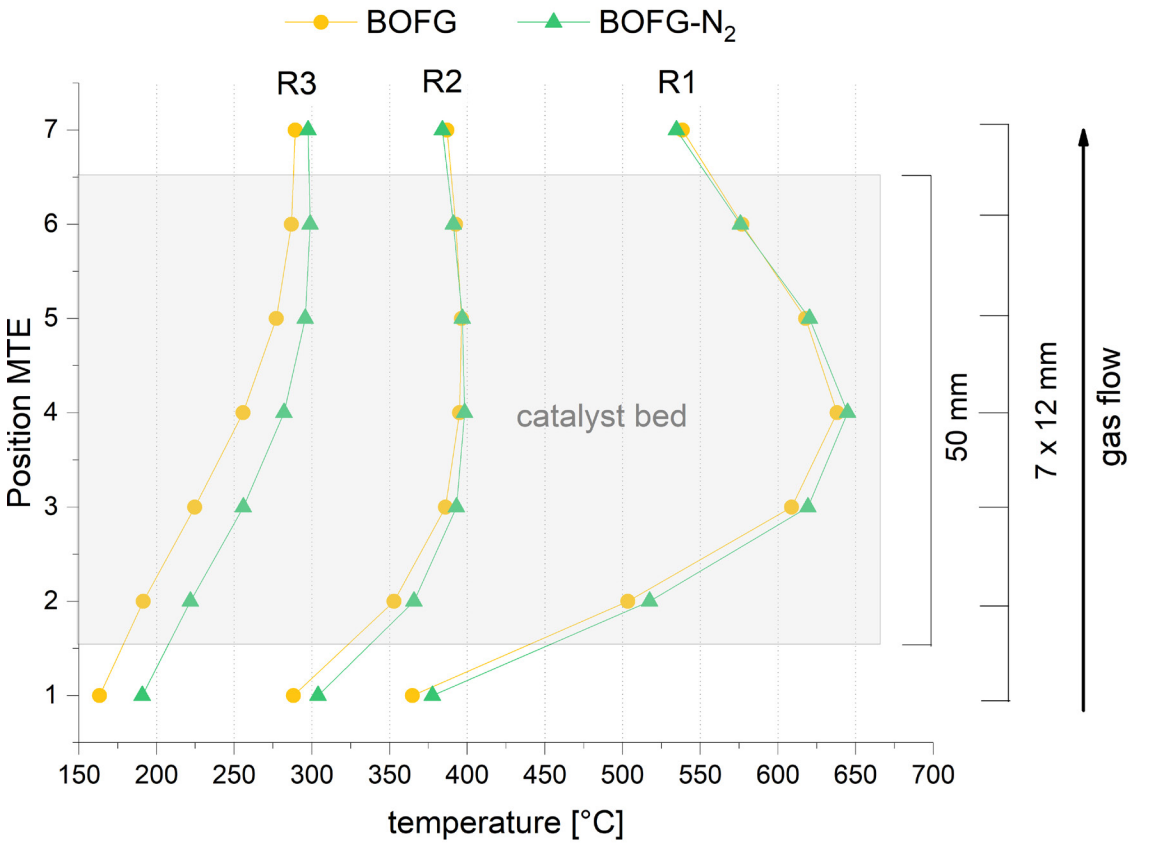

Figure 5-8: Experimentally determined axial temperature profile of the catalyst bed for three reactors (R1-R3) at feed gas compositions for BFG and BFG-N_2

As shown in Figure 5-9, the kinetic model from Kopyscinski estimates a complete conversion of CO as well as CO_2 for BOFG and for BOFG-N_2 already in R1, since the kinetic model does not assume that the methane reforms at high temperatures (500-650°C in R1). Additionally, the feed gas contained more than twice as much CO as CO_2 (ratio CO/CO_2=2.6) whereas in the case of BFG, the ratio between CO and CO_2 was approximately 1 (ratio CO/CO_2=1.1). Both for BOFG and BOFG-N_2, the reaction rates from Xu/Froment overestimate the complete conversion of CO_x in R1, resulting in methane reforming in the second reactor stage (R2), similar to the obtained observations for BFG and BFG-N_2. In the third reactor stage (R3) again, a slight conversion of the CO_2 occurs.

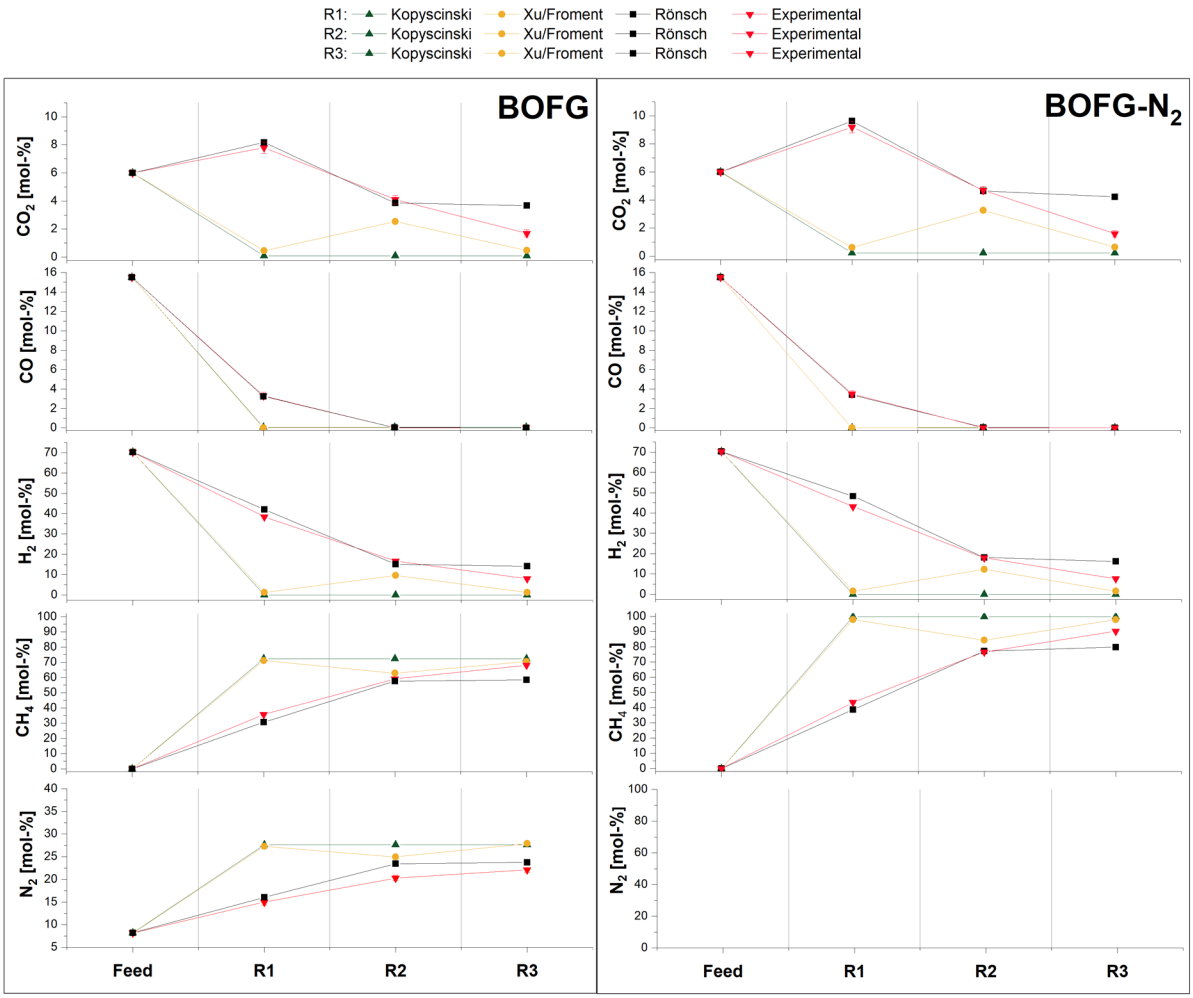

Figure 5-9: Gas composition (dry) of simulation results compared with the experimental data for BOFG ($GHSV_{input}$= 4000 h^{-1}) and BOFG-N_2 ($GHSV_{input}$= 3680 h^{-1}) at stoichiometric ratio (r_{H_2}=1) and P=4 bar

The simulation results based on the kinetic model of Rönsch show a similar trend of the gas composition for R1 and R2 as the experimental data. In the case of BOFG as well BOFG-N_2 it is clear, that at the highly elevated temperatures in R1 (maximal measured temperature 650°C) a WGSR reaction starts to dominate, resulting in increase of CO_2 concentration along with a significant decrease in CO concentration.

In case of BOFG-N_2, the increase of the CO_2 is even higher. On the other hand, the kinetic model from Rönsch predicts no further conversions in R3. This is most likely due to the low temperatures of 190-270°C in reactor R3, where the maximum temperature in the catalyst bed was measured at position 6. Analogous to BFG, when comparing the simulation results of the Rönsch kinetic model for BOFG and BOFG-N_2, no influence of the N_2 on the obtained data can be recognised. Therefore, it can be again concluded that the model of Rönsch can also simulate catalytic methanation in the presence of nitrogen.

The same approach as for the thermodynamic modelling of BFG and BFG-N_2 has been performed for the cases of BOFG and BOFG-N_2 in reactors R1-R3. Thus, for the same feed gas concentrations, a Gibbs reactor (with Gibbs free minimisation method) was applied in Aspen Plus for R1-R3. For this purpose, an average temperature has to be assumed in each reactor for a defined pressure. The temperature was varied by 1°C steps, starting from the mean reactor temperature, firstly for the reactor R1.

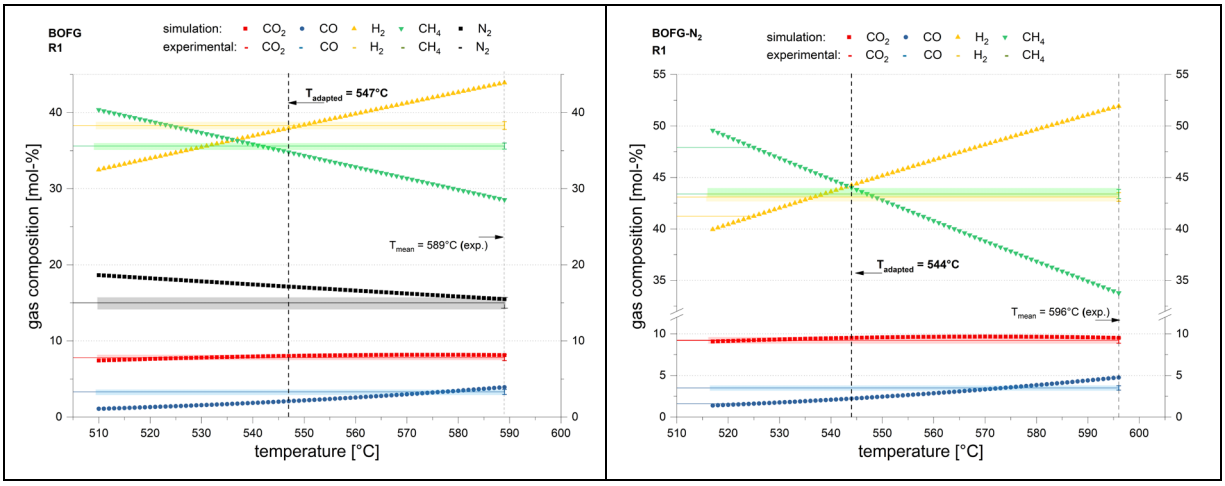

Figure 5-10: Comparison between experimental data and adapted temperature ($T_{adapted}$) for the simulation for BOFG and BOFG-N_2, r_{H_2}=1.0 in reactor R1

As shown in Figure 5-10, an approximation of the adapted temperature ($T_{adapted}$) was set by best accordance with the experimental data. It can be seen that the applied arithmetic mean temperature derived from the measured data in R1 in the case of BOFG was 42°C to high and in the case of BOFG-N_2, 52°C. The same procedure was used for the following R2 (Figure 5-11) and R3 (Figure 5-12).

The temperature elevation over the catalyst bed in R2 was accordingly lower but it resulted in the case of BOFG in 6°C higher adapted temperature, whereas in the case of BOFG-N_2 a 5°C lower temperature showed a better fit with accordance to experimental data.

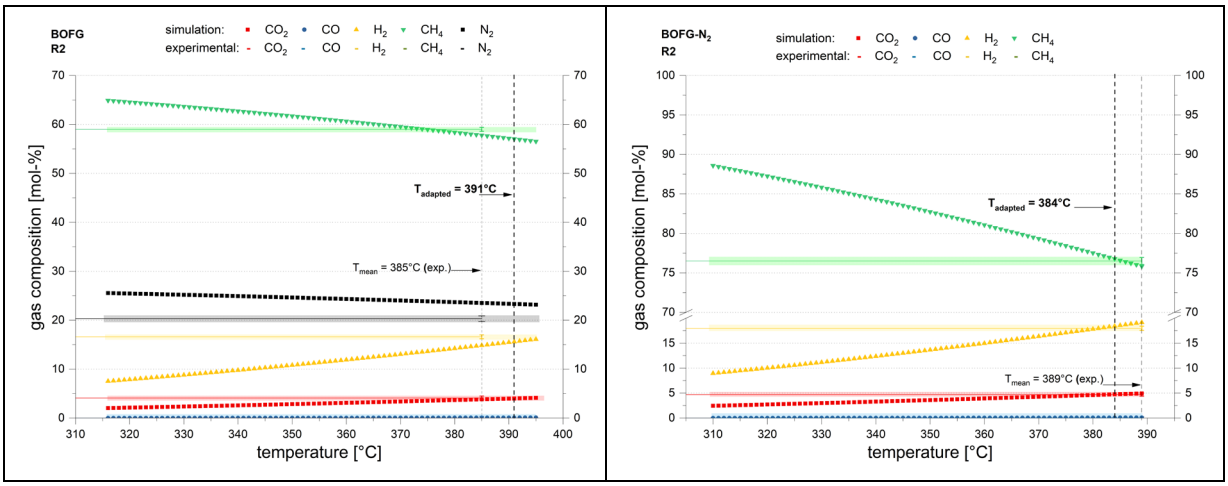

Figure 5-11: Comparison between experimental data and adapted temperature ($T_{adapted}$) for the simulation for BOFG and BOFG-N_2, r_{H_2}=1.0 in reactor R2

As for reactor R3, seen in Figure 5-12, a 43°C higher temperature adaptation was necessary for BOFG, since the implementation of T_{mean} provided suitable results. In the case of BOFG-N_2, 24°C higher temperature compared to the applied arithmetic mean temperature corresponded well with the experimental data.

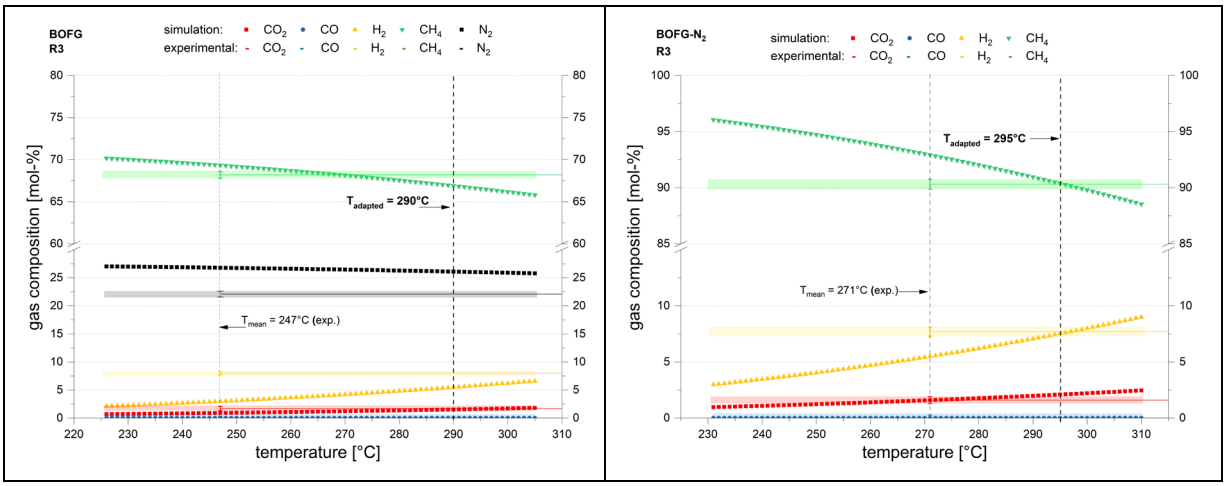

Figure 5-12: Comparison between experimental data and adapted temperature ($T_{adapted}$) for the simulation for BOFG and BOFG-N_2, r_{H_2}=1.0 in reactor R3

Yet again, the adapted temperatures, $T_{adapted}$ (marked red) correspond to the output temperatures measured at the MTE position 7 (marked green), with a deviation up to 10°C (Figure 5-13).

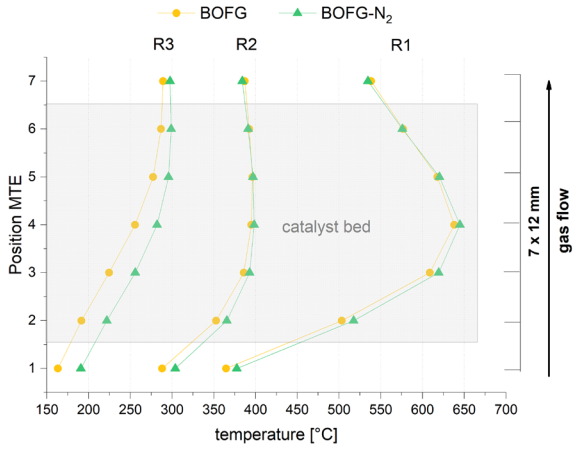

	R1		R2		R3	
	BOFG	BOFG-N_2	BOFG	BOFG-N_2	BOFG	BOFG-N_2
$T_{adapted}$	547	544	391	384	290	295
T_{mean}	589	596	385	389	247	271
7	538	535	387	384	289	298
6	577	576	393	391	287	299
5	618	620	396	397	277	296
4	638	645	395	398	256	282
3	609	619	386	393	225	256
2	503	517	353	366	192	222
1	365	378	288	304	163	191

Figure 5-13: Experimentally determined axial temperature profile of the catalyst bed, with arithmetic mean (T_{mean}) and adapted ($T_{adapted}$) temperature for three reactors (R1-R3) at feed gas compositions for BOFG and BOFG-N_2

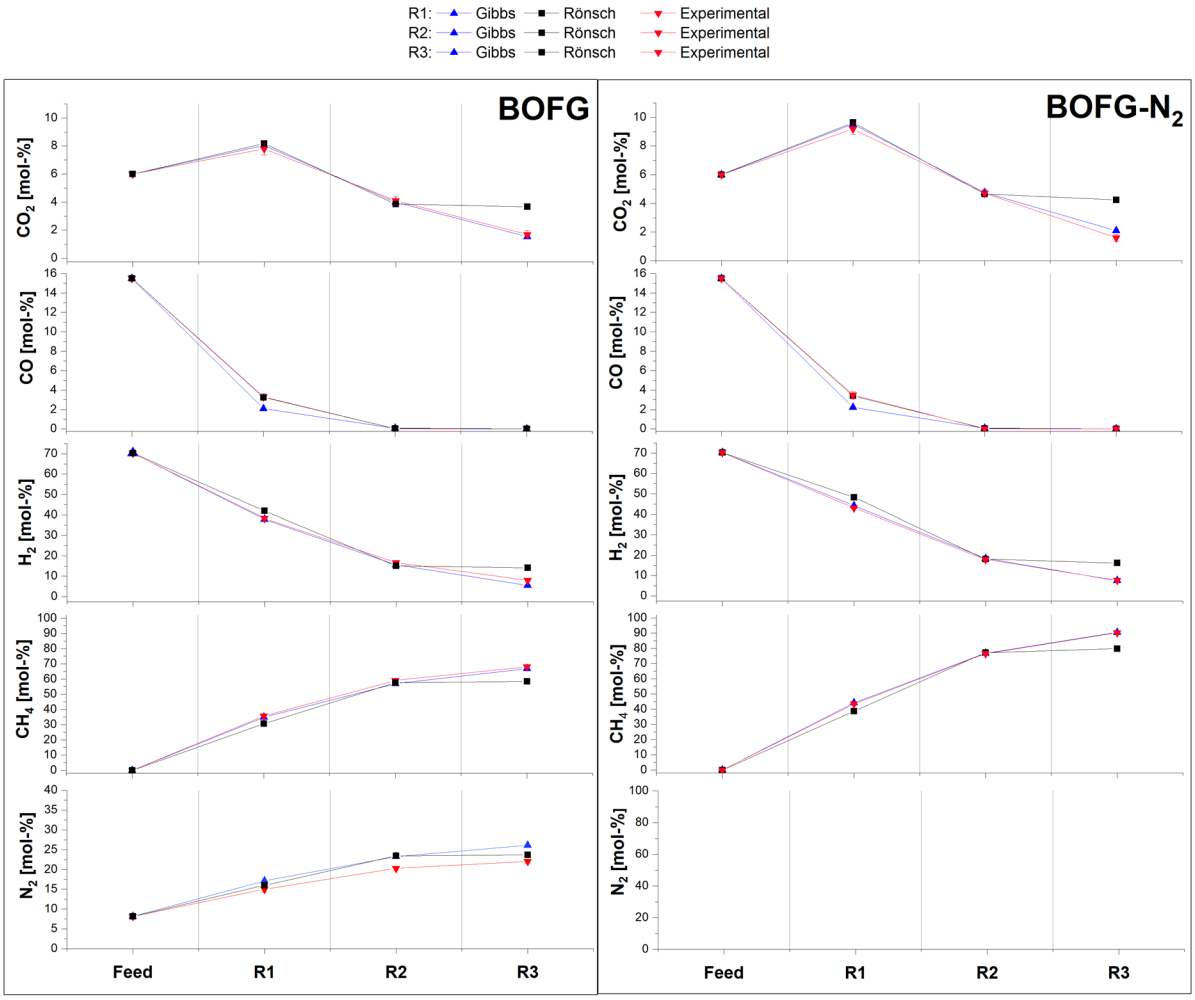

Figure 5-14: Gas composition (dry) of simulation results for kinetic model of Rönsch, Gibbs reactor and experimental data for BOFG ($GHSV_{input}$=4000 h^{-1}) and BOFG-N_2 ($GHSV_{input}$= 3680 h^{-1}) at stoichiometric ratio (r_{H_2}=1) and P=4 bar

As shown in Figure 5-14, the experimental data are in good accordance with the obtained data from the Gibbs reactor model for all three reactor stages (R1-R3). Thus, it can be concluded that all three reactors are not kinetically limited. Furthermore, the outlet temperature above the catalyst bed is appropriate for the calculation of the thermodynamic equilibrium. This is plausible, since the equilibrium is most sensitive to and adjusts to the local operating temperature.

6 Discussion

6.1 Experimental results

Experimental tests have shown that complete conversion of the CO and CO_2 gases in the feed gas for the methanation is achieved, for gas compositions of two steel gases, BFG and BOFG, without the necessity of CO_2 separation from the steel gases. The first experimental series, with the variation of GHSV and pressure, demonstrated that high pressures result as expected in higher CO_x conversion, whereas the increase of the GHSV inhibits the conversion on account of the residence time.

With the variation of the H_2 surplus at GHSV=4000 h^{-1} and P=4 bar for BFG and BOFG with and without N_2, complete conversions of CO_x were already achieved with 5% H_2 surplus upwards for BFG and with 4% H_2 surplus upwards for BOFG, with and without N_2 in the feed gas, with three-stage methanation.

When outlining the difference between the CO and CO_2 methanation, the closer examination of the CO and CO_2 conversion showed that CO_2 conversion is inhibited by the CO methanation on account of faster adsorption.

The requirements of the methanation product gas quality depend on its application. When considering steel gases as a carbon source for the methanation, the product gas can be used within the steel production as lean gas, where the product gas is not subject to a specified quality. As shown in Table 6-1, the enrichment of the BFG and BOFG via methanation results in CH_4-rich product gases, with the potential for their utilisation in the integrated steel plant.

Table 6-1: Comparison of the higher heating values of the steel gases and enriched BFG and BOFG after the methanation

steel gases [12]			**after methanation**	
BFG	BOFG	COG	BFG	BOFG
			(r_{H_2}=1.09–1)	(r_{H_2}=1.09–1)
[MJ m^{-3}]	[MJ m^{-3}]	[MJ m^{-3}]	[MJ m^{-3}]	[MJ m^{-3}]
2.6–4.4	8.26	11–21	19.2–19.8	26.7–28.8

The resulting product gas from the BFG methanation obtained comparable higher heating values (19.2–19.8 MJ m^{-3}) to COG (21.0 MJ m^{-3}) and more than double that of the unrefined BOFG (8.26 MJ m^{-3}). In the case of BOFG, due to the lower amount of N_2 present in the feed gas (approximately 8%), the values were even higher (26.7–28.8 MJ m^{-3}).

However, for many technical applications it can be assumed that a natural gas substitute should be created in accordance with the applicable quality specification of the natural gas grid. Since the experimental tests were performed with and without N_2, the measured product

gas compositions were compared to the requirements of the Austrian ÖVGW guideline for the natural gas network ÖVGW G-31. Quality criteria such as gas composition regarding CH_4, CO_2 and H_2, higher heating value, Wobbe index and relative density are of great importance (Table 6-2).

Table 6-2: Gas specification according to ÖVGW G-31 [32]

Parameter	Unit	Specification
Wobbe Index	MJ Nm^{-3}	47.7–56.5
HHV	MJ Nm^{-3}	38.5–46.0
relative density	-	0.55–0.65
accompany gases		
O_2	mol.-%	≤ 0.5
CO_2	mol.-%	≤ 2.0
N_2	mol.-%	≤ 5
H_2	mol.-%	≤ 4

Although the CH_4 content is not specifically stated in the G-31 directive, the Austrian imported natural gas contains >98% of CH_4 and approximately 1% of higher hydrocarbons (up to C_6). [32]

As already shown with the conducted experiments, despite the higher CO_x conversions when surplus H_2 is applied, the amount of the unreacted H_2 lowers the HHV of the product gas. Therefore, the gas composition of the product gas for BFG and BOFG with and without N_2 for stoichiometric r_{H_2}=1 were compared to the G-31 guideline. The graphic representation of the calculated Wobbe index according to Eq. 6-1 as a correlation between the HHV (H_s) and relative density can be seen in Figure 6-1.

$$W_s = \frac{H_s}{\sqrt{d}} \qquad \text{(Eq. 6-1)}$$

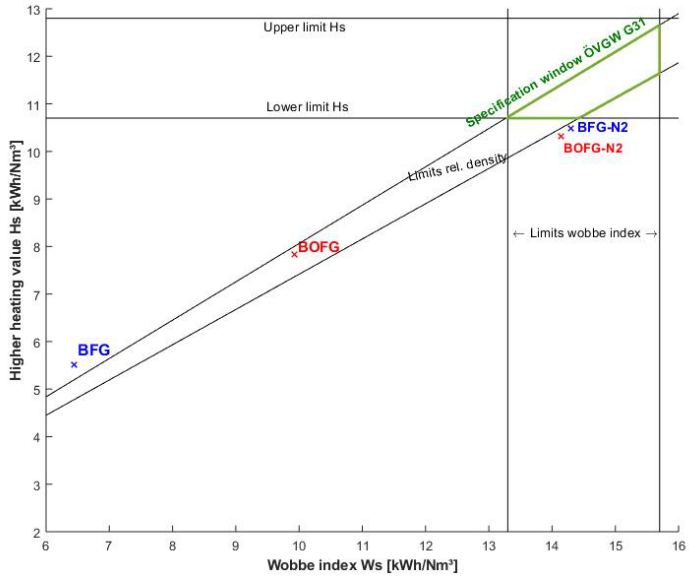

Figure 6-1: Requirements of the natural gas grid according to ÖVGW G-31

None of the four chosen product gases correspond to the specification window of the ÖVGW G-31 (green market area), in terms of HHV as well as gas composition when considering BFG and BOFG without N_2 (Figure 6-2). Therefore, without any further H_2 downstream removal, the requirements for the natural gas grid injection would not be met. On the other hand, revision of the ÖVGW G-31 in terms of allowed H_2 concentration (up to 10 mol.-% H_2) in the gas grid could be expected in the future. Thus, an increase in the permissible hydrogen feed-in capacity can be assumed, at least in some parts of the gas network. [146,147]

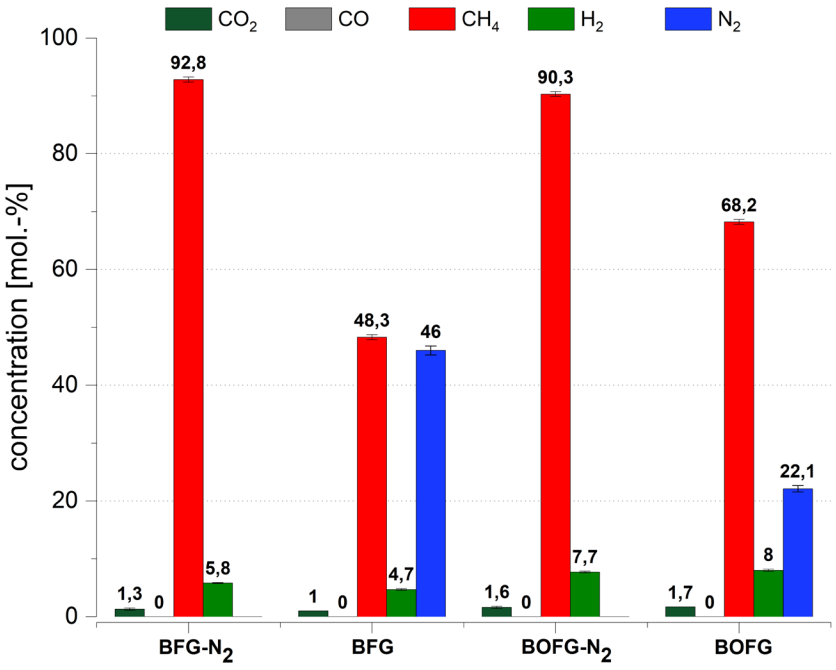

Figure 6-2: Gas composition of the product gas for methanation of BFG, BFG-N_2, BOFG and BOFG-N_2 at P= 4 bar and r_{H_2}=1

6.2 Simulation results

In the simulation modelling, three kinetic models from the open literature were chosen based on the type of the catalyst as well as the operating conditions. All three kinetic models consider CO_2 methanation as a linear combination of CO-methanation and WGSR, suitable when both CO and CO_2 gases are present in the methanation feed gas. The kinetic models from Kopyscinski and Xu/Froment, often used by various researchers in their simulation based evaluations, and the kinetic model from Rönsch et al. derived for dynamic methanation conditions were applied.

As expected, due to the origin of the kinetic model, which is valid for temperatures up to 350°C, the simulation results for kinetic model from Kopyscinski overestimated the conversion of CO and CO_2, showing that the predicted kinetics were simply too fast in the applied temperature range. For the applied temperatures in BFG and BOFG with and without N_2, especially in R1 (450-650°C), no reverse reaction (methane reforming) is applied in the kinetic model that occurs at high elevated temperatures.

In addition, the kinetic model from Xu/Froment did not provide satisfying results, with the overestimation of the CO and CO_2 conversions in R1 for all four gas compositions. Due to the origin of the developed kinetic model for methane steam reforming, inactivity of the model occurred at temperatures around 250°C as well as methane reforming domination at temperatures around 400°C.

However, a similar trend as in the experiments and good fit of the gas composition for each reactor stage was achieved with the kinetic model from Rönsch. For the high elevated temperatures in reactor R1 (maximal measured temperature 600 and 650°C), the domination of WGSR reaction, resulting in an increase of CO_2 concentration was in accordance with the experimental results. On the other hand, the kinetic model from Rönsch predicted no further conversions in R3. When comparing the simulation results of the kinetic model between BFG and BFG-N_2 as well as BOFG and BOFG-N_2 no substantial deviation can be seen. It can, therefore, be concluded that Rönsch reaction rates for CO methanation for a commercial catalyst with 18 wt.-% Ni (from Klose) predicts the conversions correctly, with and without present N_2 as well as over a wide temperature range between 250-650°C.

The slight deviations of the CO_2 concentration between the Rönsch kinetic model and experimental data, led to the assumption of thermodynamic limitations in R1. For the same feed gas concentrations a Gibbs free minimisation method was applied for R1-R3 at a defined reactor temperature and pressure. The applied arithmetic mean temperature and resulting simulation results of the catalyst bed, were not in correlation with measured data. The temperature variation and adapted temperature ($T_{adapted}$) for each reactor stage has shown a good correspondence for both gases in all three reactor stages R1-R3, with the measured temperature of the MTE on position 7. The MTE position 7 was in the inert bulk material, immediately after the catalyst bed. The deviations between the adapted temperature and the outlet temperature on the MTE position 7 can be caused due to the position of the multi-thermocouple, since the thermocouple was positioned 22 mm excentric from the reactors middle axis. Nevertheless, with the applied Gibbs reactors, a thermodynamically prevailing regime can be concluded in all three reactor stages. Additionally, it is obvious that the reactor outlet temperature determines the thermodynamic equilibrium.

7 Summary and Outlook

Steel production via the classic blast furnace/basic oxygen route (integrated steel plant) is a well established and extensively used process, but at the same time one of the largest CO_2 contributors to the global GHG emissions. In order to achieve the climate goals set in the Paris agreement, the integration of renewable energies as well as the reduction of the CO_2 emissions is one of the key points that have to be implemented in the existing steel production infrastructure. Due to their high CO, CO_2 and N_2 content and poor heating value, the by-product steel gases, especially BFG and BOFG show great potential for alternative re-utilisation as a carbon source for the catalytic methanation within a Power-to-Gas plant. To explore the possibility of avoiding the energy intensive step of CO_2 separation from the steel gases as well as retaining an additional carbon source in CO, the main focus in the present thesis was to determine the influence of the inert components, such as N_2, on the catalytic methanation of the two steel gases. The influence of the N_2 in the feed gas on the catalytic methanation was explored on a complementary basis using a simulation program and experimentally derived results.

The experimental work was carried out on a laboratory test plant for catalytic methanation with three fixed-bed reactors connected in series, using a commercial nickel-based bulk catalyst. The experimental setup with multi-thermocouple in each reactor provided an axial temperature profile of the catalyst bed. The optimal operating conditions for complete conversion of CO and CO_2 components of two steel gases compositions, BFG and BOFG, with and without N_2 in the feed gas, were determined with the variation of feed gas flow rate (GHSV) and pressure as well as the H_2 surplus. The first experimental series, with the variation of GHSV and pressure, demonstrated that high pressures result in higher CO_x conversions, whereas the increase of the GHSV inhibits the conversion on account of the residence time. With the variation of the H_2 surplus at a defined GHSV and pressure, with and without N_2, complete conversions of CO_x were already achieved with 5% H_2 surplus upwards for BFG and with 4% H_2 surplus upwards for BOFG, with three-stage methanation. The significant influence of the N_2 in the feed gas was only on account of the heating value of CH_4-rich product gas. The utilisation of the steel gases as energy carriers within the integrated steel plant is state-of-the-art, contributing to the steel plant´s energy demand, where the remaining part is provided by electrical energy and fossil fuels. As an outcome, the resulting enriched product gas after the methanation of BFG and BOFG, the lean gas, has potential for use directly in steel production and could substitute for fossil fuel – for example, natural gas – demand.

The obtained experimental data were afterwards compared with the simulation results, modelled with the simulation program Aspen Plus® V9. Three different kinetic models from the literature were chosen, corresponding to the process parameters used for the experimental tests of the BFG and BOFG gas compositions. Of the three kinetic models used, the kinetic model from Rönsch with the derived CO methanation rate for commercial 18 wt.-% nickel catalyst (Klose) showed a good fit at high elevated temperatures. The model predicted the trend of the conversions and yields correctly, with and without N_2 present, as

well as over a wide temperature range between 250-650°C. The slight deviations in the CO_2 concentration between the Rönsch kinetic model and experimental data led to the assumption of thermodynamic limitations at different reactor stages. The assumption was confirmed by the application of Gibbs reactors in the simulation. It is shown that an equilibrium based on the reactor outlet temperature described the experimental data well, thus confirming the thermodynamically dominated reactions.

In the case of the thermodynamic limitation, the output concentration is bound to its equilibrium at a certain temperature and pressure, as shown with the conducted simulation results. Depending on the feed gas composition, pressure and temperature, the equilibrium will be shifted towards products in case of elevated pressure, but the higher conversions will produce more reaction heat, resulting in higher temperatures. Most commonly for fixed-bed reactors, the modelling of the reactors is simplified to one-dimensional (1-D), with the consideration of the axial distribution of gas species and the temperature. Although the radial profiles are either neglected or assumed, the experimental and simulation results have shown that the latter is not trivial and needs more attention. The axial temperature profile was not sufficient for the determination of the exact reaction temperature. Therefore the next developing step on the VTiU experimental test plant is the expansion of the temperature measurements to radial and axial profile, as well as the screening of the catalyst temperatures, by applying the thermocouples directly to the catalyst bulk (Figure 7-1).

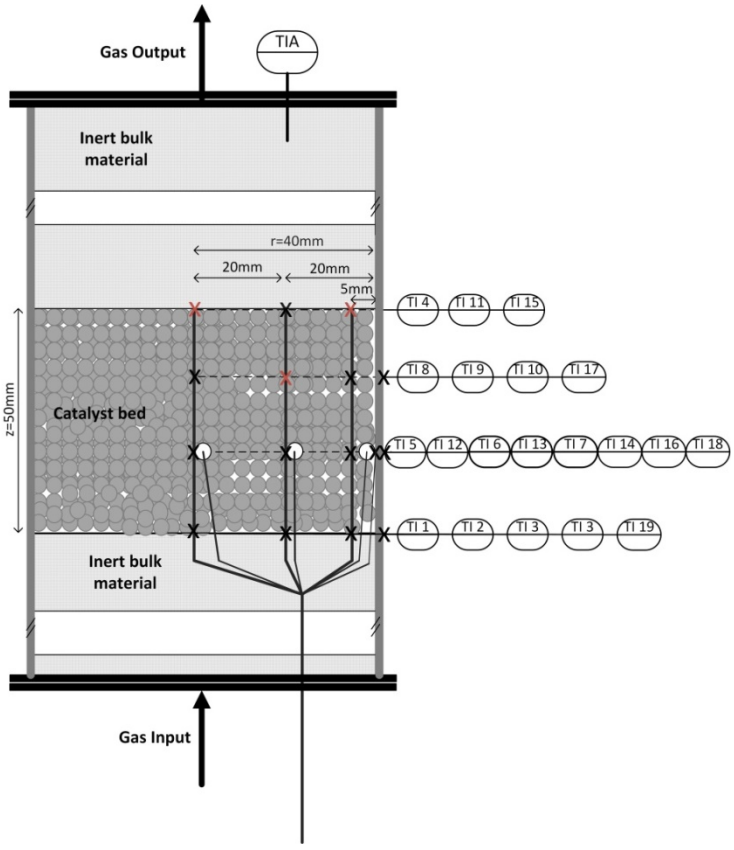

Figure 7-1: Experimental set-up for measuring radial and axial temperature profiles of the catalyst bed

8 Directory

8.1 List of Symbols

E_a	[KJ mol^{-1}]	activation energy
$T_{adapted}$	[°C]	adapted reactor temperature
$K_{CO}, K_{H2}, K_{CH4,}$	[Pa^{-1}]	adsorption constants
CBl	[-][	carbon atom balancing
UCO_x	[-]	conversion of CO_x
CF_v	[-]	correction factor
D_n	[kg m^{-3}]	density for calibration
y_{ji}	[-]	dry gas component
K_1, K_2, K_j	[-]	equilibrium constants
C_p	[J K^{-1}]	heat capacity
HHV_i	[MJ m^3]	higher heating value of component i
HBl	[-]	hydrogen atom balancing
LHV_i	[MJ m^3]	lower heating value of component i
T_{mean}	[°C]	mean reactor temperature
$\dot{n}_i$	[mol min^{-1}]	molar flow
n_{ij}	[mol]	molarity
OBl	[-]	oxygen atom balancing
p	[bar]	partial pressure
P	[bar]	pressure
k_1, k_2	[kmol kg$^{-1}_{cat.}$s^{-1}] or [kmol Pa^{0,5} kg$^{-1}_{cat.}$ s^{-1}]	rate coefficient
r_{H_2}	[-]	ratio H_2/CO_x
r	[kmol kg$^{-1}_{cat.}$s^{-1}bar^{-1}]	reaction rate

T_0	[K]	reference temperature
S_{CH_4}	[-]	selectivity
u_y	[%]	standard deviation of function y
T	[°C] or [K]	temperature
A, B, C, D	[-]	used supplied coefficients
V	[L]	volume
$\dot{V}$	[L min^{-1}]	volume flow
x_{ij}	[-]	wet gas component
Y_{CH_4}	[-]	yield

8.2 List of Abbreviations

AEC	Alkaline Electrolysis
BF	blast furnace
BFG	blast furnace gas
BFG-N_2	blast furnace gas without N_2
BOF	basic oxygen furnace
BOFG	basic oxygen furnace gas
BOFG-N_2	basic oxygen furnace gas without N_2
CCS	Carbon Capture and Storage/Sequestration
CCU	Carbon Capture and Usage/Utilisation
CNG	compressed natural gas
COG	coke oven gas
DAC	direct air capture
EAF	electric arc furnace
Eq	Equation
ESP	electrostatic precipitator
FFG	Austrian Research Promotion Agency
GHG	greenhouse gas

GHSV	gas hourly space velocity
LD	Linz-Donawitz
LHHW	Langmuir-Hinschelwood-Hougen-Watson
MFC	mass flow controller
MTE	multi-thermocouple
PCI	pulverised coal injection
PCS	process control system
PEMEC	Proton Exchange Membrane Electrolysis
PtG	Power-to-Gas
PtL	Power-to-Liquid
PtX	Power-to-X
R1, R2, R3	first, second, third reactor
RDS	rate determining step
RPlug	plug flow reactor
rWGSR	Reverse Water gas shift reaction
SOEC	Solid oxide Electrolysis
TRL	technology readiness level
W	heat exchanger

8.3 Indexes

i, j	component index
eq	equivalent
m	adsorption expression exponent
n	temperature exponent
abs	absolute
α, β, γ	concentration exponent
C	carbon
$meth$	methanation

$WGSR$ water gas shift reaction

8.4 List of Tables

8.5 List of Figures

8.6 References

[1] European Comission CA. Paris Agreement; Available from: https://ec.europa.eu/clima/policies/international/negotiations/paris_en (accessed on 1.10.2019).

[2] Our World in Data. Total greenhouse gas emissions; Available from: https://ourworldindata.org/greenhouse-gas-emissions (accessed on 2.11.2020).

[3] European Comission. Communication from the commission to the european parliament, the european council, the council, the european economic and social committee, the committee of the regions and the european investment bank: A Clean Planet for all A European strategic long-term vision for a prosperous, modern, competitive and climate neutral economy. COM/2018/773 final.

[4] Fischedick M, Görner K, Thomeczek M (eds.). CO_2: Abtrennung, Speicherung, Nutzung. Berlin, Heidelberg: Springer Berlin Heidelberg; 2015. doi:10.1007/978-3-642-19528-0.

[5] d'Amore F, Lovisotto L, Bezzo F. Introducing social acceptance into the design of CCS supply chains: A case study at a European level. Journal of Cleaner Production 2020;249:119337. doi:10.1016/j.jclepro.2019.119337.

[6] Schumann D. Public Perception of CO_2 Pipelines. Energy Procedia 2017;114:7356–66. doi:10.1016/j.egypro.2017.03.1867.

[7] RIS. Bundesgesetz, mit dem ein Bundesgesetz über das Verbot der geologischen Speicherung von Kohlenstoffdioxid erlassen wird und das Umweltverträglichkeitsprüfungsgesetz 2000, das Bundes-Umwelthaftungsgesetz, die Gewerbeordnung 1994 sowie das Mineralrohstoffgesetz geändert werden StF: BGBl. I Nr. 144/2011 (NR: GP XXIV RV 1387 AB 1572 S. 137. BR: 8615 AB 8651 S. 803.) [CELEX-Nr.: 32009L0031]: Verbot der geologischen Speicherung von Kohlenstoffdioxid.

[8] Umweltbundesamt GmbH. Klimaschutzbericht 2019: Analyse der Treibhausgas-Emissionen bis 2017; Available from: ISBN 978-3-99004-522-0.

[9] Umweltbundesamt GmbH. Klimaschutzbericht 2020; Available from: ISBN 978-3-99004-558-9.

[10] BP. Full report – BP Statistical Review of World Energy 2019: 68th Edition 2019.

[11] Blanco H, Faaij A. A review at the role of storage in energy systems with a focus on Power to Gas and long-term storage. Renewable and Sustainable Energy Reviews 2018;81:1049–86. doi:10.1016/j.rser.2017.07.062.

[12] European IPPC Bureau (ed.). Best Available Techniques (BAT) Reference Document for Iron and Steel Production: Industrial Emissions Directive 2010/75/EU (Integrated Pollution Prevention and Control); 2013. ISBN 978-92-79-26475-7 (pdf).

[13] Porzio GF, Nastasi G, Colla V, Vannucci M, Branca TA. Comparison of multi-objective optimization techniques applied to off-gas management within an integrated steelwork. Applied Energy 2014;136:1085–97. doi:10.1016/j.apenergy.2014.06.086.

[14] Vogl V, Åhman M, Nilsson LJ. Assessment of hydrogen direct reduction for fossil-free steelmaking. Journal of Cleaner Production 2018;203:736–45. doi:10.1016/j.jclepro.2018.08.279.

[15] Sterner Michael, Eckert Fabian, Thema Martin. Technologien für Nachhaltigkeit und Klimaschutz - chemische Prozesse und stoffliche Nutzung von CO_2: 2.1 Chemische

Energiespeicher. Frankfurt am Main: DECHEMA Gesellschaft für Chemische Technik und Biotechnologie e.V; 2017.

[16] Ortloff F, Graf F, Lubenau U. CO_2 aus dem Energieund Industriesektor zur Einkopplung in Power-to-Gas-Prozesse.

[17] Eurostat Statistics. 8-12022019-AP-EN; Available from: https://ec.europa.eu/eurostat/statistics-explained/index.php/Renewable_energy_statistics (accessed on 18.11.2019).

[18] Sterner M, Stadler I (eds.). Handbook of Energy Storage. Berlin, Heidelberg: Springer Berlin Heidelberg; 2019. doi:10.1007/978-3-662-55504-0.

[19] Lund PD, Lindgren J, Mikkola J, Salpakari J. Review of energy system flexibility measures to enable high levels of variable renewable electricity. Renewable and Sustainable Energy Reviews 2015;45:785–807.

[20] Thema M, Bauer F, Sterner M. Power-to-Gas: Electrolysis and methanation status review. Renewable and Sustainable Energy Reviews 2019;112:775–87. doi:10.1016/j.rser.2019.06.030.

[21] Wulf C, Linßen J, Zapp P. Review of Power-to-Gas Projects in Europe. Energy Procedia 2018;155:367–78. doi:10.1016/j.egypro.2018.11.041.

[22] Scarlat N, Dallemand J-F, Fahl F. Biogas: Developments and perspectives in Europe. Renewable Energy 2018;129:457–72. doi:10.1016/j.renene.2018.03.006.

[23] Napp TA, Gambhir A, Hills TP, Florin N, Fennell PS. A review of the technologies, economics and policy instruments for decarbonising energy-intensive manufacturing industries. Renewable and Sustainable Energy Reviews 2014;30:616–40. doi:10.1016/j.rser.2013.10.036.

[24] European Commission. A Clean Planet for all A European long-term strategic vision for a prosperous, modern, competitive and climate neutral economy: In-Depth Analysis in Support of the Commission Communication COM(2018)773. Brussels; 2018.

[25] Sterner M, Bauer F, Crotogino F, Eckert F, Olshausen C von, Teichmann D et al. (eds.). Energiespeicher: Bedarf, Technologien, Integration 2.Auflage. 8. Chemische Energiespeicher; 2017. 978-3-662-48892-8. doi:10.1007/978-3-662-48893-5_8.

[26] https://www.esrl.noaa.gov/gmd/ccgg/trends/global.html. (Accessed on 26.10.2020).

[27] Hashimoto K. Metastable metals for "green" materials for global atmosphere conservation and abundant energy supply. Materials Science and Engineering 1994(A179/A180):27–30. doi:10.1016/0921-5093(94)90158-9.

[28] Bailera M, Lisbona P, Romeo LM, Espatolero S. Power to Gas projects review: Lab, pilot and demo plants for storing renewable energy and CO_2. Renewable and Sustainable Energy Reviews 2017;69:292–312. doi:10.1016/j.rser.2016.11.130.

[29] Götz M, Lefebvre J, Mörs F, McDaniel Koch A, Graf F, Bajohr S et al. Renewable Power-to-Gas: A technological and economic review. Renewable Energy 2016;85:1371–90. doi:10.1016/j.renene.2015.07.066.

[30] Rönsch S, Schneider J, Matthischke S, Schlüter M, Götz M, Lefebvre J et al. Review on methanation – From fundamentals to current projects. Fuel 2016;166:276–96. doi:10.1016/j.fuel.2015.10.111.

[31] Ghaib K, Ben-Fares F-Z. Power-to-Methane: A state-of-the-art review. Renewable and Sustainable Energy Reviews 2018;81:433–46. doi:10.1016/j.rser.2017.08.004.

[32] Österreichische Vereinigung für das Gas- und Wasserfach. Erdgas in Österreich: Richtlinie G31; 2001.

[33] Thema Mea. Biological CO_2-Methanation: An Approach to Standardization. Energies 2019;12(9):1670. doi:10.3390/en12091670.
[34] Stolten D, Scherer V (eds.). Transition to Renewable Energy Systems. Weinheim, Germany: Wiley-VCH Verlag GmbH & Co. KGaA; 2013. doi:10.1002/9783527673872.
[35] Schweitzer D, Beirow M, Gredinger A, Armbrust N, Waizmann G, Dieter H et al. Pilot-Scale Demonstration of Oxy-SER steam Gasification: Production of Syngas with Pre-Combustion CO_2 Capture. Energy Procedia 2016;86:56–68. doi:10.1016/j.egypro.2016.01.007.
[36] Lehner M, Tichler R, Steinmüller H, Koppe M. Power-to-Gas: Technology and Buisiness Models; 2014. 978-3-319-03994-7.
[37] Buttler A, Spliethoff H. Current status of water electrolysis for energy storage, grid balancing and sector coupling via power-to-gas and power-to-liquids: A review. Renewable and Sustainable Energy Reviews 2018;82:2440–54. doi:10.1016/j.rser.2017.09.003.
[38] H2Future Project. https://www.h2future-project.eu/; Available from: https://www.h2future-project.eu/ (accessed on 21.11.2019).
[39] Lecker B, Illi L, Lemmer A, Oechsner H. Biological hydrogen methanation - A review. Bioresource technology 2017;245(Pt A):1220–8. doi:10.1016/j.biortech.2017.08.176.
[40] DVGW Deutscher Verein des Gas- und Wasserfaches e.V. Technisch-wissenschaftlicher Verein. Store&Go: Innovative large-scale energy storage technologies and Power-to-Gas concepts after optimisation: Roadmap for large-scale storage based PtG conversion in the EU up to 2050. 978th ed; 2019.
[41] DNV GL. Methanation: Technical Fundamentals and Market Overview. Report No:OAG.19.R.10157194; 2019.
[42] Graf F, Krajete A, Schmack U. Techno-ökonomische Studie zur biologischen Methanisierung bei Power-to-Gas-Konzepten: DVGW-1658 Abschlussbericht G 3-01-13; 2014.
[43] Doris Hafenbradl E. Power-to-Gas with Biological Methanation- an Industrial Application for Energy Storage and CO2 Reuse worldwide; Regatec Conference 2019, Malmö.
[44] Schwede S, Bruchmann F, Thorin E, Gerber M. Biological Syngas Methanation via Immobilized Methanogenic Archaea on Biochar. Energy Procedia 2017;105:823–9. doi:10.1016/j.egypro.2017.03.396.
[45] Blanco H, Nijs W, Ruf J, Faaij A. Potential of Power-to-Methane in the EU energy transition to a low carbon system using cost optimization. Applied Energy 2018;232:323–40. doi:10.1016/j.apenergy.2018.08.027.
[46] Misono M. Heterogeneous Catalysis of Mixed Oxides: Perovskite and heteropoly catalysts. Volume 176; 2013. 978-0-444-53833-8.
[47] Sabatier P, Senderens JB. New methane synthesis. Compt. Rend. Acad. Sci. 1902;134:514–6.
[48] Frontera P, Macario A, Ferraro M, Antonucci P. Supported Catalysts for CO2 Methanation: A Review. Catalysts 2017;7(12):59. doi:10.3390/catal7020059.
[49] Calvin H. Bartholomew. Mechanisms of catalyst deactivation. Applied Catalysis 2001(212):17.
[50] Argyle M, Bartholomew C. Heterogeneous Catalyst Deactivation and Regeneration: A Review. Catalysts 2015;5(1):145–269. doi:10.3390/catal5010145.
[51] C&CS catalysts &chemical specialities GWPmbH. Technical Information/Specification: Methanation Catalyst Meth134 (C13-4-04). Munich; 2013.

[52] Perry RH, Green DW, Maloney JO (eds.). Perry's chemical engineers' handbook. 7th ed. New York: McGraw-Hill; 1997.
[53] Gao J, Wang Y, Ping Y, Hu D, Xu G, Gu F et al. A thermodynamic analysis of methanation reactions of carbon oxides for the production of synthetic natural gas. RSC Adv. 2012;2(6):2358–68. doi:10.1039/c2ra00632d.
[54] Guy B. Marin, Gregory S. Yablonsky, Denis Constales. Kinetics of Chemical Reactions: Decoding Complexity. Second, Completely Revised and enlarged Edition; 2017. 978-3-527-34295-2.
[55] Fujita S-i, Nakamura M, Doi T, Takezawa N. Mechanisms of methanation of carbon dioxide and carbon monoxide over nickel/alumina catalysts. Applied Catalysis A: General 1993;104(1):87–100. doi:10.1016/0926-860X(93)80212-9.
[56] Dalmon JA, Martin GA. The kinetics and mechanism of carbon monoxide methanation over silica-supported nickel catalysts. Journal of Catalysis 1983;84(1):45–54. doi:10.1016/0021-9517(83)90084-2.
[57] Jan Kopyscinski. Production of synthetic natural gas in a fluidized bed reactor: Understanding the hydrodynamic, mass transfer and kinetic effects. Dissertation; 2010.
[58] Weatherbee GD, Bartholomew CH. Hydrogenation of CO_2 on group VIII metals II. Kinetics and mechanism of CO_2 hydrogenation on nickel. Journal of Catalysis 1982;77(2):460–72. doi:10.1016/0021-9517(82)90186-5.
[59] Koschany F, Schlereth D, Hinrichsen O. On the kinetics of the methanation of carbon dioxide on coprecipitated $NiAl(O)_x$. Applied Catalysis B: Environmental 2016;181:504–16. doi:10.1016/j.apcatb.2015.07.026.
[60] Miguel CV, Mendes A, Madeira LM. Intrinsic kinetics of CO_2 methanation over an industrial nickel-based catalyst. Journal of CO2 Utilization 2018;25:128–36. doi:10.1016/j.jcou.2018.03.011.
[61] Miao B, Ma SSK, Wang X, Su H, Chan SH. Catalysis mechanisms of CO_2 and CO methanation. Catal. Sci. Technol. 2016;6(12):4048–58. doi:10.1039/C6CY00478D.
[62] Baraj E, Vagaský S, Hlinčik T, Ciahotný K, Tekáč V. Reaction mechanisms of carbon dioxide methanation: review. Chemical Papers 2016;70(4):47. doi:10.1515/chempap-2015-0216.
[63] Mills GA, Steffgen FW. Catalytic Methanation. Catalysis Reviews 1974;8(1):159–210. doi:10.1080/01614947408071860.
[64] Marwood M, Doepper R, Renken A. In-situ surface and gas phase analysis for kinetic studies under transient conditions The catalytic hydrogenation of CO_2. Applied Catalysis A: General 1997;151(1):223–46. doi:10.1016/S0926-860X(96)00267-0.
[65] Pan Q, Peng J, Wang S, Wang S. In situ FTIR spectroscopic study of the CO_2 methanation mechanism on $Ni/Ce_{0.5}Zr_{0.5}O_2$. Catal. Sci. Technol. 2014;4(2):502–9. doi:10.1039/C3CY00868A.
[66] Ibraeva ZA, Nekrasov NV, Gudkov BS, Yakerson VI, Beisembaeva ZT, Golosman EZ et al. Kinetics of methanation of carbon dioxide on a nickel catalyst. Theor Exp Chem 1991;26(5):584–8. doi:10.1007/BF00531916.
[67] van Herwijnen T, Doesburg H, Jong WA de. Kinetics of the methanation of CO and CO_2 on a nickel catalyst. Journal of Catalysis 1973;28(3):391–402. doi:10.1016/0021-9517(73)90132-2.
[68] Sehested J, Dahl S, Jacobsen J, Rostrup-Nielsen JR. Methanation of CO over nickel: Mechanism and kinetics at high H_2/CO ratios. The journal of physical chemistry. B 2005;109(6):2432–8. doi:10.1021/jp040239s.

[69] Schoubye P. Methanation of CO on some Ni catalysts. Journal of Catalysis 1969;14(3):238–46. doi:10.1016/0021-9517(69)90431-X.
[70] van Meerten RZC, Vollenbroek JG, Croon MHJM de, van Nisselrooy PFMT, Coenen JWE. The kinetics and mechanism of the methanation of carbon monoxide on a nickel-silica catalyst. Applied Catalysis 1982;3(1):29–56. doi:10.1016/0166-9834(82)80221-2.
[71] Klose J, Baerns M. Kinetics of the methanation of carbon monoxide on an alumina-supported nickel catalyst. Journal of Catalysis 1984;85(1):105–16. doi:10.1016/0021-9517(84)90114-3.
[72] Sughrue EL, Bartholomew CH. Kinetics of carbon monoxide methanation on nickel monolithic catalysts. Applied Catalysis 1982;2(4-5):239–56. doi:10.1016/0166-9834(82)80071-7.
[73] Inoue H, Funakoshi M. Kinetics of methanation of carbon monoxide and carbon dioxide. J. Chem. Eng. Japan / JCEJ 1984;17(6):602–10. doi:10.1252/jcej.17.602.
[74] Kai T, Furusaki S, Yamamoto K. Methanation of carbon monoxide by a fluidized catalyst bed. J. Chem. Eng. Japan / JCEJ 1984;17(3):280–5. doi:10.1252/jcej.17.280.
[75] R.E.Hayes, W.J.Thomas, K.E.Hayes. A study of the nickel-catalyzed methanation reaction. Journal of Catalysis 1985;92(2):312–26. doi:10.1016/0021-9517(85)90266-0.
[76] Zhang J, Fatah N, Capela S, Kara Y, Guerrini O, Khodakov AY. Kinetic investigation of carbon monoxide hydrogenation under realistic conditions of methanation of biomass derived syngas. Fuel 2013;111:845–54. doi:10.1016/j.fuel.2013.04.057.
[77] Kopyscinski J, Schildhauer TJ, Biollaz SMA. Methanation in a fluidized bed reactor with high initial CO partial pressure: Part I—Experimental investigation of hydrodynamics, mass transfer effects, and carbon deposition. Chemical Engineering Science 2011;66(5):924–34. doi:10.1016/j.ces.2010.11.042.
[78] Kopyscinski J, Schildhauer TJ, Biollaz SMA. Methanation in a fluidized bed reactor with high initial CO partial pressure: Part II— Modeling and sensitivity study. Chemical Engineering Science 2011;66(8):1612–21. doi:10.1016/j.ces.2010.12.029.
[79] Kaltenmeier Klaus. Untersuchungen zur Kinetik der Methanisierung von CO_2-reichen Gasen bei höheren Drücken. Karlsruhe; 1988.
[80] Xu J, Froment GF. Methane steam reforming, methanation and water-gas shift: I. Intrinsic kinetics. AIChE J. 1989;35(1):88–96. doi:10.1002/aic.690350109.
[81] Kai T, Furusaki S. Methanation of carbon dioxide and fluidization quality in a fluid bed reactor—the influence of a decrease in gas volume. Chemical Engineering Science 1987;42(2):335–9. doi:10.1016/0009-2509(87)85063-7.
[82] Rönsch S, Köchermann J, Schneider J, Matthischke S. Global Reaction Kinetics of CO and CO_2 Methanation for Dynamic Process Modeling. Chem. Eng. Technol. 2016;39(2):208–18. doi:10.1002/ceat.201500327.
[83] Kopyscinski J, Schildhauer TJ, Biollaz SMA. Fluidized-Bed Methanation: Interaction between Kinetics and Mass Transfer. Ind. Eng. Chem. Res. 2011;50(5):2781–90. doi:10.1021/ie100629k.
[84] Kopyscinski J, Schildhauer TJ, Biollaz SMA. Production of synthetic natural gas (SNG) from coal and dry biomass – A technology review from 1950 to 2009. Fuel 2010;89(8):1763–83. doi:10.1016/j.fuel.2010.01.027.
[85] Perry M, Eliason D. CO_2 Recovery and Sequestration at Dakota Gasification Company 2004.

[86] Haldor Topsoe. Methanation Catalysts: https://www.topsoe.com/processes/sng/methanation (accessed on 19.6.2020).
[87] Götz M. Methanisierung im Dreiphasen-Reaktor: Dissertation. Karlsruhe; 2014.
[88] Lefebvre J. Three-phase CO_2 methanation: methanation reaction kinetics and transient behavior of a slurry bubble column reactor. Dissertation; 2019.
[89] Neubert M. Adapting catalytic methanation to small- and mid-scale SNG production. Doktorarbeit. FAU Erlangen-Nürnberg; 2019.
[90] Neubert M, Hauser A, Pourhossein B, Dillig M, Karl J. Experimental evaluation of a heat pipe cooled structured reactor as part of a two-stage catalytic methanation process in power-to-gas applications. Applied Energy 2018;229:289–98. doi:10.1016/j.apenergy.2018.08.002.
[91] Biegger P, Kirchbacher F, Medved A, Miltner M, Lehner M, Harasek M. Development of Honeycomb Methanation Catalyst and Its Application in Power to Gas Systems. Energies 2018;11(7). doi:10.3390/en11071679.
[92] Biegger P. Keramische Wabenkatalysatoren zur chemischen Methanisierung von CO_2. Doktorarbeit. Leoben; 2017.
[93] The AISE Steel Foundation (ed.). The Making, Shaping and Treating of Steel: Steelmaking and Refining Volume. 11th Edition. 11th ed. Pittsburgh, PA: Association of Iron and Steel Engineers; 1998. 0-930767-02-0.
[94] de stahl; Available from: https://en.stahl-online.de/index.php/topics/technology/steelmaking/ (accessed on 25.11.2019).
[95] Worldsteel association. World steel in figures 2019: Steel statistical yearbook.
[96] The AISE Steel Foundation (ed.). The Making, Shaping and Treating of Steel: Ironmaking Volume. 11th Edition. Pittsburgh, PA: Association of Iron and Steel Engineers; 1999. 0-930767-09-9.
[97] Gara S, Schrimpf S. Behandlung von Reststoffen und Abfällen in der Eisen- und Stahlindustrie: Monographien, Band 92. Wien: Bundesministerium für Umwelt, Jugend und Familie; 1998. 3-85457-394-4.
[98] Babich A, Senk D (eds.). The Coal Handbook: Towards Cleaner Production: Chapter 12- Coal use in iron and steel metallurgy. Coal Utilisation; 2013. doi:10.1533/9781782421177.3.267.
[99] Rummer B, Thaler C, Feilmayr C. The Long Way to PCI in Linz – First Operation Experience. BHM Berg- und Hüttenmännische Monatshefte 2016;162(1):34–40. doi:10.1007/s00501-016-0557-4.
[100] Maarten Geerdes, Rénard Chaigneau, Ivan Kurunov, Oscar Lingiardi, John Ricketts. Modern Blast Furnace Ironmaking: An Introduction; 2015. 978-1-61499-499-2. doi:10.3233/978-1-61499-499-2-i.
[101] Doschek K, Ponak C (eds.). Prozessintegrierter Umweltschutz: 580017. Leoben; 2017.
[102] Arvola J, Harkonen J, Mottonen M, Haapasalo H, Tervonen P. Combining Steel and Chemical Production to Reduce CO_2 Emissions. LCE 2011;02(03):115–22. doi:10.4236/lce.2011.23015.
[103] Frey A, Goeke V, Voss C. Steel Gases as Ancient and Modern Challenging Resource; Historical Review, Description of the Present, and a Daring Vision. Chemie Ingenieur Technik 2018;90(10):1384–91. doi:10.1002/cite.201800046.
[104] Schöß MA, Redenius A, Turek T, Güttel R. Chemische Speicherung regenerativer elektrischer Energie durch Methanisierung von Prozessgasen aus der Stahlindustrie. Chemie Ingenieur Technik 2014;86(5):734–9. doi:10.1002/cite.201300086.

[105] Otto A, Robinius M, Grube T, Schiebahn S, Praktiknjo A, Stolten D. Power-to-Steel: Reducing CO_2 through the Integration of Renewable Energy and Hydrogen into the German Steel Industry. Energies 2017;10(4):451. doi:10.3390/en10040451.
[106] Harp G, Tran KC, Sigurbjornsson O, Bergins C. 2. Application of Power to Methanol Technology to Integrated Steelworks for Profitability, Conversion Efficiency, and CO_2 2015(Conference Paper: 2nd European Steel Technology and Application Days).
[107] Uribe-Soto W, Portha J-F, Commenge J-M, Falk L. A review of thermochemical processes and technologies to use steelworks off-gases. Renewable and Sustainable Energy Reviews 2017;74:809–23. doi:10.1016/j.rser.2017.03.008.
[108] Carbon2Chem project; Available from: https://www.thyssenkrupp.com/en/company/innovation/technologies-for-the-energy-transition/carbon2chem.html (accessed on 5.10.2019).
[109] Deerberg G, Oles M, Schlögl R. The Project Carbon2Chem®. Chemie Ingenieur Technik 2018;90(10):1365–8. doi:10.1002/cite.201800060.
[110] Thonemann N, Maga D, Petermann C. Handling of Multi-Functionality in Life Cycle Assessments for Steel Mill Gas Based Chemical Production. Chemie Ingenieur Technik 2018;90(10):1576–86. doi:10.1002/cite.201800025.
[111] Schlüter S, Hennig T. Modeling the Catalytic Conversion of Steel Mill Gases Using the Example of Methanol Synthesis. Chemie Ingenieur Technik 2018;90(10):1541–58. doi:10.1002/cite.201800021.
[112] Girod K., Breitkreuz K., Hennig T., Lohmann H., Kaluza S., Schluter S. Steel Mills as Syngas Source for Methanol Synthesis: Simulation and Practical Performance Investigations. Chemical Engineering Transactions 2019(74):475–80. doi:10.3303/CET1974080.
[113] Yildirim Ö, Nölker K, Büker K, Kleinschmidt R. Chemical Conversion of Steel Mill Gases to Urea: An Analysis of Plant Capacity. Chemie Ingenieur Technik 2018;90(10):1529–35. doi:10.1002/cite.201800019.
[114] Stießel S, Berger A, Fernández Sanchis EM, Ziegmann M. Methodology for the Evaluation of CO_2 -Based Syntheses by Coupling Steel Industry with Chemical Industry. Chemie Ingenieur Technik 2018;90(10):1392–408. doi:10.1002/cite.201800030.
[115] Bundesministerium für Bildung und Forschung. Karliczek: Innovationen ermöglichen klimaneutrale Industrie: Bundesforschungsministerin eröffnet Carbon2Chem-Konferenz in Berlin. Nr. 160/2020; 2020.
[116] Project: i3-upgrade; Available from: https://www.i3upgrade.eu/ (accessed on 9.1.2020).
[117] Wolf-Zöllner, P., Krammer, A., Medved, A., Salbrechter, K., Lehner, M. Dynamic methanation of by-product gases from integrated steelworks. In: International Conference on Polygeneration Strategies, Vienna, 18.-19.11.2019.
[118] Hauser, A., Weitzer, M., Gunsch, S., Neubert, M., Karl, J. Dynamic methanation of by-product gases from the steel industry in the scope of the project i³upgrade. In: International Conference on Polygeneration Strategies, Vienna, 18.-19.11.2019.
[119] Steelanol project; Available from: http://www.steelanol.eu/en (accessed on 20.11.2019).
[120] STEELANOL, Production of sustainable, advanced bio-ethANOL through an innovative gas-fermentation process using exhaust gases emitted in the STEEL industry; Available from: https://ec.europa.eu/inea/en/horizon-2020/projects/h2020-energy/biofuels/steelanol (accessed on 10.11.2020).

[121] Ana Roza Medved, Philipp Biegger ML. Integration einer Power-to-Gas Anlage in ein integriertes Stahlwerk. In: Technische Universität Graz, editor. 15. Symposium Energieinnovation. Graz; 2018. 978-3-85125-586-7. doi:10.3217/978-3-85125-586-7.
[122] Rosenfeld DC, Böhm H, Lindorfer J, Lehner M. Scenario analysis of implementing a power-to-gas and biomass gasification system in an integrated steel plant: A techno-economic and environmental study. Renewable Energy 2020;147:1511–24. doi:10.1016/j.renene.2019.09.053.
[123] RenewableSteelGases: Einbindung erneuerbarer Energie in die Stahlproduktion zur Energieeffizienzsteigerung und Reduktion der CO_2-Emissionen: Publizierbarer Endbericht. Projektnummer: 858776; 2020.
[124] Fuchs J, Schmid J.C., Müller S, Hofbauer H. Dual fluidized bed gasification of biomass with selective carbon dioxide removal and limestone as bed material: A review. Renewable and Sustainable Energy Reviews 2019(107):212–31. doi:10.1016/j.rser.2019.03.013.
[125] Hammerschmid M, Müller S, Fuchs J, Hofbauer H. Evaluation of biomass-based production of below zero emission reducing gas for the iron and steel industry. Biomass Conv. Bioref. 2020;55:537. doi:10.1007/s13399-020-00939-z.
[126] Aaron H. Felder. Detailplanung eines Laborversuchstandes zur katalytischen Methanisierung von CO_2: Masterarbeit. Leoben; 2013.
[127] BHDT GmbH. product specification; Available from: https://www.bhdt.at/Category/Connectors/BestLoc-R-Compact-Flange-Norsok (accessed on 15.10.2019).
[128] RVT Process Equipment GmbH. HiDur stoneware balls: Technical Information/Specification; 2009.
[129] Bronkhorst. Fluidat®: https://www.fluidat.com/default.asp (accessed on 17.1.2020).
[130] Harald Winkler. Implementierung und experimentelle Untersuchung von Festbettreaktoren für die CO- und CO2-Methanisierung: Masterarbeit. Leoben; 2018.
[131] Binderbauer P. Dokumentation des Prozessleisystems der Versuchsanlage zur chemischen Methanisierung: Bachelorarbeit; 2017.
[132] Jens Hagen. Chemiereaktoren: Auslegung und Simulation; 2004. 3-527-30827-X.
[133] Manuel Jakubith. Grundoperationen und chemische Reaktionstechnik: Einführung in die Technische Chemie; 1998. 3-527-28870-8. doi:10.1002/3527603212.
[134] National Institute of Standards and Technology (ed.). CRC Handbook of Chemistry and Physics: 97th edition. 2016-2017; 2017. 978-1-4987-5429-3.
[135] Hertwig K, Martens L. Chemische Verfahrenstechnik: Berechnung, Auslegung und Betrieb chemischer Reaktoren. München; 2007. 978-3-486-57798-3.
[136] Fuchs J, Schmid JC, Müller S, Mauerhofer AM, Benedikt F, Hofbauer H. The impact of gasification temperature on the process characteristics of sorption enhanced reforming of biomass. Biomass Conv. Bioref. 2019;31:205. doi:10.1007/s13399-019-00439-9.
[137] Abdulrazzaq S. Abdullah. Modeling and Simulation of Methanation Catalytic Reactor in Ammonia Plant. International Journal of Advanced Research in Chemical Science (IJARCS) 2015(Volume 2, Issue 10):80–4.
[138] Neubert M, Widzgowski J, Rönsch S, Treiber P, Dillig M, Karl J. Simulation-Based Evaluation of a Two-Stage Small-Scale Methanation Unit for Decentralized Applications. Energy Fuels 2017;31(2):2076–86. doi:10.1021/acs.energyfuels.6b02793.

[139] David Schlereth. Kinetic and Reactor Modeling for the Methanation of Carbon Dioxide: Dissertation. TU München; 2015.
[140] Kayvan Khorsand ea. Modeling and simulation of methanation catalytic reactor in ammonia unit. Petroleum & Coal 2007(49 (1)):46–53.
[141] Er-rbib Hanaa BC. Modelling and Simulation of Methanation Catalytic Reactor for Renewable Electricity Storage 2013;vol. 35, 2013:541–6.
[142] Jürgensen L, Ehimen EA, Born J, Holm-Nielsen JB. Dynamic biogas upgrading based on the Sabatier process: thermodynamic and dynamic process simulation. Bioresource technology 2015;178:323–9. doi:10.1016/j.biortech.2014.10.069.
[143] Elnashaie, S S.E.H. E, S S. Modelling, simulation and optimization of industrial fixed bed catalytic reactors. Topics in chemical engineering 1993(Volume 7).
[144] Karim Khodier. Experimentelle Untersuchung und Simulation der Methanisierung von Kuppelgasen aus integrierten Hüttenwerk: Masterarbeit. Leoben; 2016.
[145] Er-rbib H, Bouallou C. Modeling and simulation of CO methanation process for renewable electricity storage. Energy 2014;75:81–8. doi:10.1016/j.energy.2014.05.115.
[146] RAG, MUL, Verbund, EI-JKU, Axiom, BOKU. Underground Sun.Storage - Publizierbarer Endbericht - 3.1; 2017.
[147] Energieinstitut an der Johannes Kepler Universität Linz et al. (ed.). Power to Gas - eine Systemanalyse. Endbericht 2014; 2014.

Appendices

A: Detailed drawing of the pressure reactor (BHDT GmbH)

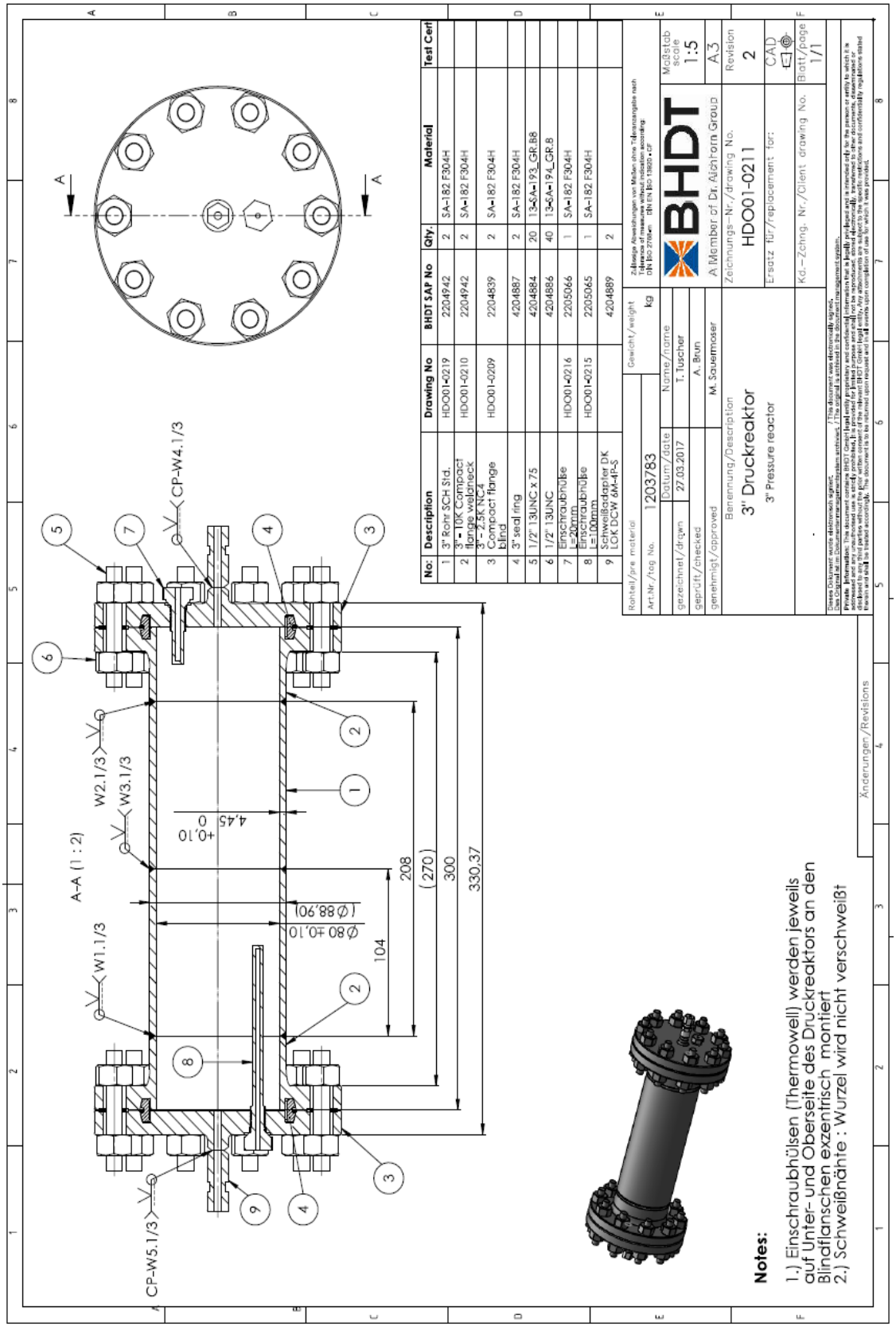

B: detailed drawing of the pressure vessel (BHDT GmbH)

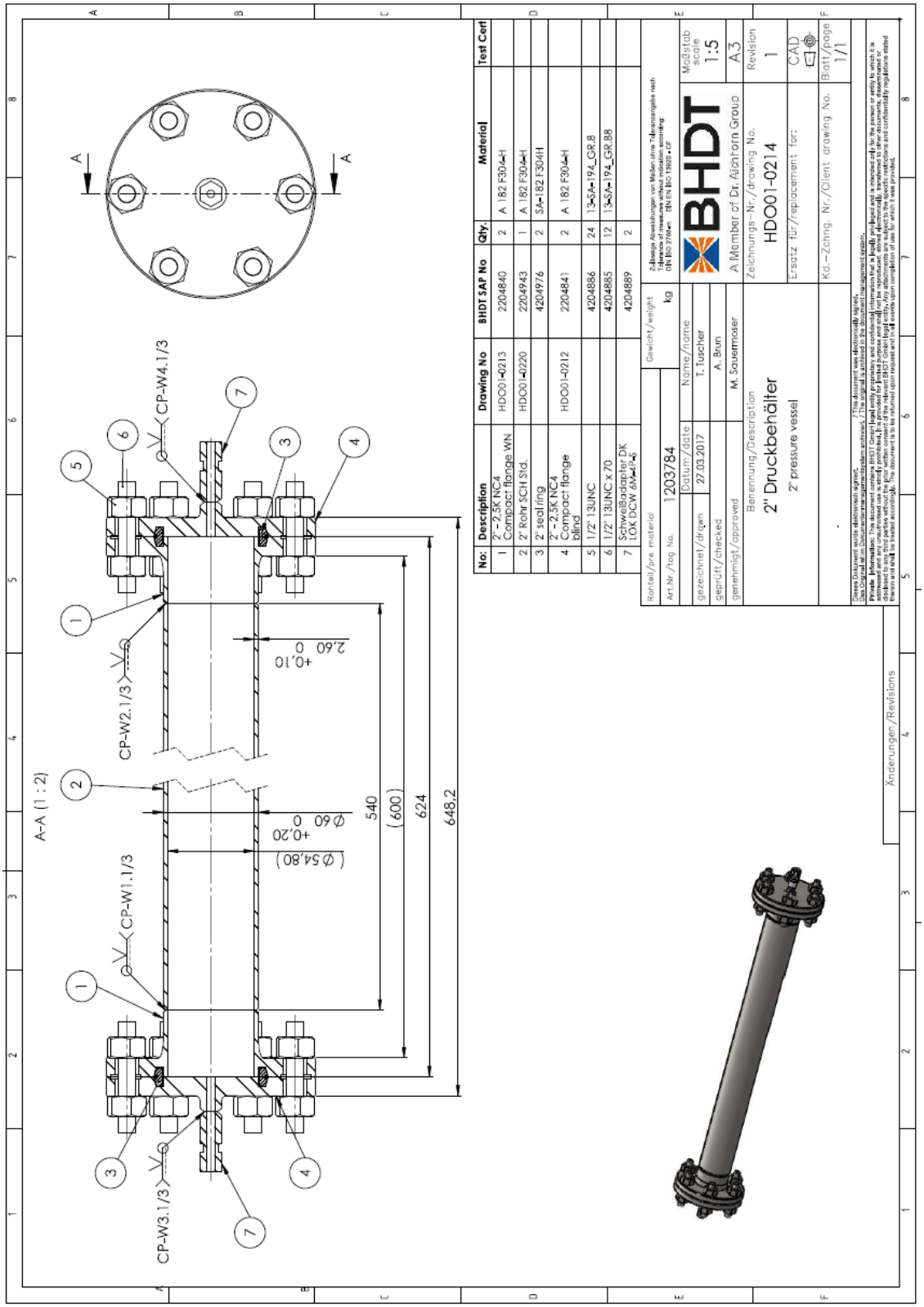

No:	Description	Drawing No	BHDT SAP No	Qty.	Material	Test Cert
1	2" - 2.5K NC4 Compact flange WN	HD001-0213	2204840	2	A 182 F304-H	
2	2" Rohr SCH Std.	HD001-0220	2204943	1	A 182 F304-H	
3	2" sealring		4204976	2	SA-182 F304H	
4	2" - 2.5K NC4 Compact flange blind	HD001-0212	2204841	2	A 182 F304-H	
5	1/2" 13UNC		4204886	24	13SA-194_GR.8	
6	1/2" 13UNC x 70		4204885	12	13SA-194_GR.B8	
7	Schweißadapter DK LOK DCW 6MoHP-6		4204889	2		

Rohteil/pre material
Art.Nr./Itag No. 1203784
Gewicht/weight kg

	Name/name	Datum/date
gezeichnet/drawn	T. Tuscher	27.03.2017
geprüft/checked	A. Brun	
genehmigt/approved	M. Sauermoser	

Zulässige Abweichungen von Maßen ohne Toleranzangabe nach Toleranzklasse mittel nach DIN ISO 2768-1 ersetzt durch DIN EN ISO 13920 - CF

BHDT
A Member of Dr. Ahlhorn Group

Benennung/Description
2" Druckbehälter
2" pressure vessel

Zeichnungs-Nr./drawing No.
HD001-0214

Ersatz für/replacement for:

Kd.-Zchng. Nr./Client drawing No.

Maßstab scale 1:5
A3
Revision 1
CAD
Blatt/page 1/1

Änderungen/Revisions

C: Wolfram Mathematica program code

Methanisierung CO+CO2+H2+N2

Standarddruck 1 bar, ideales Gas

Dateneingabe

```
ClearAll["Global`*"]
Get["Properties.m"]
```

Meldung: R,T0,TS,Ptot sind in diesem file geschützt für
R = 8314 J/Kmol.K, T0 = 273.15 K, TS = 298.15 K

```
da = Import["Excel-file.xlsx", {Dta", 5];
```

Berechnung

```
z = 21;

(* Anzahl Proben eingeben *)
j = 1;
ii = z * 2 + 6;

Do[Do[
  TC = da[[i + n, 17]];
  S1 = da[[i + n, 19]]; (* Molenstrom Eduktgase *)
  (* x = Gaszusammensetzung feucht; y = Gaszusammensetzung trocken *)
  y1CO2 = da[[i, 21]];
  y1M = da[[i, 23]];
  y1CO = da[[i, 22]];
  y1N2 = da[[i, 25]];
  y1H2 = da[[i, 24]];
  y2CO2 = da[[i + n, 21]];
  y2M = da[[i + n, 23]];
  y2CO = da[[i + n, 22]];
  y2N2 = da[[i + n, 25]];
  y2H2 = da[[i + n, 24]];
  x1CO2 := y1CO2;
  x1CO := y1CO;
  x1M := y1M;
  x1H2 := y1H2;
  x1N2 := y1N2;
  x1H2O = 0;
  x2CO2 := y2CO2 (1 - x2H2O);
  x2CO := y2CO (1 - x2H2O);
  x2M := y2M (1 - x2H2O);
  x2H2 := y2H2 (1 - x2H2O);
  x2N2 := y2N2 (1 - x2H2O);
  (* Summationsbedingungen *)
```



```
  Sum1 = x1CO2 + x1CO + x1H2 + x1M + x1N2 == 1;
  Sum2 = x2CO2 + x2CO + x2H2 + x2H2O + x2M + x2N2 == 1;
  (* Atombilanzen *)
  CB1 := S1 (x1CO2 + x1CO + x1M) == S2 (x2CO2 + x2CO + x2M) + S3;
  (* S4 = C-Korrektur; höhere KWs oder C-Ablagerungen *)
  HB1 := S1 (x1H2 * 2 + x1H2O * 2 + x1M * 4) == S2 (x2H2 * 2 + x2H2O * 2 + x2M * 4);
  OB1 := S1 (x1CO2 * 2 + x1CO + x1H2O) == S2 (x2CO2 * 2 + x2CO + x2H2O);
  lsg = Flatten[Solve[{Sum1, Sum2, CB1, HB1, OB1}]];
  (* Gesamtumsatz an COx *)
  UCOx := ((S1 * (x1CO2 + x1CO) - S2 * (x2CO2 + x2CO)) / (S1 * (x1CO2 + x1CO))) /. lsg;
  UCO2 := ((S1 * (x1CO2) - S2 * (x2CO2)) / (S1 * (x1CO2 + x1CO))) /. lsg;
  UCO := ((S1 * (x1CO) - S2 * (x2CO)) / (S1 * (x1CO))) /. lsg;

  (* Ausbeute für ganze Anlage *)
  AusbeuteC = (S2 * x2M / (S1 * (x1CO2 + x1CO))) /. lsg;
  (* Selektivität bezogen auf Methan; ganze Anlage *)
  SelektivitätM = (S2 * x2M / (S1 * (x1CO2 + x1CO) - S2 * (x2CO2 + x2CO))) /. lsg;

  (*Auswertung vom Gleichgewichtzusammensetzung*)

  TR = da[[i + n, 17]]; (* Reaktionstemperatur, °C *)
  Pges = da[[i + n, 18]];
  P0 = 1 ;      (* Gesamtdruck, bar *)
  n0CH4 = 0 ;      (* Anfangsmole Methan *);
  n0H2O := 0 ; (* Anfangsmole Wasserdampf *);
  n0CO = S1 (x1CO);
  n0CO2 = S1 (x1CO2);
  n0H2 = S1 (x1H2);
  n0N2 = S1 (x1N2);

  reaction1 = H2Og + CH4g - 3 H2g - COg;
  reaction2 = H2g + CO2g - COg - H2Og;
  (* Standardbildungsenthalpien bei 298,15 K, kJ/kmol *)
  gB1 = reaction1[[3]] * 1000;
  gB2 = reaction2[[3]] * 1000;
  hB1 = reaction1[[2]] * 1000;
  hB2 = reaction2[[2]] * 1000;
  cpR1 := reaction1[[7]];
  cpR2 := reaction2[[7]];
  (* Gleichgewichtskonstanten bei 298,15 K *)
  K01 = Exp[-gB1 / (R / 1000 * TS)];
  K02 = Exp[-gB2 / (R / 1000 * TS)];
  (* Temperatur abhängige Reaktionswärme, kJ/kmol *)
  hR1[TK_] := hB1 + Integrate[cpR1, {T, TS, TK}];
  hR2[TK_] := hB2 + ∫_TS^TK cpR2 dT;
```

```
(* Temperatur abhängige Gleichgewichtskonstanten *)
K1[TKelvin_] := Exp[Log[K01] + ∫_TS^TKelvin hR1[TT] / (R/1000 * TT^2) dTT];

K2[TKelvin_] := Exp[Log[K02] + ∫_TS^TKelvin hR2[TT] / (R/1000 * TT^2) dTT];

(* Gleichgewichtskonstanten für Reaktion 1 und 2 bei Reaktionstemperatur *)
KR1 = K1[TR + T0];
KR2 = K2[TR + T0];
relax[{Methan_, Wasserdampf_, Kohlenmonoxid_, Kohlendioxid_, Wasserstoff_}] :=
 Module[{nCH4, nH2O, nCO, nCO2, nH2, dn1, dn2, lsg1, lsg2}(* lokale Variable *),
  (* Übergabewerte, immer Anfangswerte *)
  nCH4 = Methan;
  nH2O = Wasserdampf;
  nCO = Kohlenmonoxid;
  nCO2 = Kohlendioxid;
  nH2 = Wasserstoff;
  (* Reaktion 1 *)
  lsg1 = Flatten[Solve[ (nCH4 + dn1) * (nH2O + dn1) / (nCO - dn1) * (nH2 - 3 dn1)^3 *
       (Pges^2 / (nCO + nCO2 + nH2 + nCH4 + nH2O - 2 dn1)^2) == KR1]];
  (* Auswahl der richtigen Lösung *)
  iter1 = 1;
  While[Length[Select[{nCH4 + dn1, nH2O + dn1, nCO - dn1, nH2 - 3 dn1} /. lsg1[[iter1]],
      NonNegative]] < 4, iter1++];
  (* Zuweisen der richtigen Lösung *)
  Δn1 = dn1 /. lsg1[[iter1]];
  (* Zuweisen der Konzentrationen nach Reaktion 1 = vor Reaktion 2 *)
  nCH4 = nCH4 + Δn1; nH2O = nH2O + Δn1; nCO = nCO - Δn1; nH2 = nH2 - 3 Δn1;

  (* Reaktion 2 *)
  lsg2 = Flatten[Solve[ (nCO2 + dn2) (nH2 + dn2) / (nCO - dn2) (nH2O - dn2) == KR2]];
  (* Auswahl der richtigen Lösung *)
  iter2 = 1;
  While[Length[Select[{nCO2 + dn2, nH2 + dn2, nCO - dn2, nH2O - dn2} /. lsg2[[iter2]],
      NonNegative]] < 4, iter2++];
  (* Zuweisen der richtigen Lösung *)
  Δn2 = dn2 /. lsg2[[iter2]];
  (* Zuweisen der Konzentrationen nach Reaktion 2 = vor Reaktion 1 *)
  nCO2 = nCO2 + Δn2; nH2 = nH2 + Δn2; nCO = nCO - Δn2; nH2O = nH2O - Δn2;
  (* Ergebnis *)
  Molges = Total[{nCH4, nH2O, nCO, nCO2, nH2}];
  werte = {nCH4, nH2O, nCO, nCO2, nH2}];
(* Iteration bis FixedPoint *)
sol = FixedPoint[relax, {n0CH4, n0H2O, n0CO, n0CO2, n0H2}];
(*Versuche mit N2*)
Molges1 = Molges + n0N2;
werte1 = Insert[werte, n0N2, -1];

tabexp[j] = {{UCOx, UCO, UCO2, AusbeuteC, SelektivitätM, S2, x2CO2, x2CO, x2H2, x2H2O,
    x2M, werte1, werte1/Molges1}} /. lsg (*{werte1,werte1/Molges1}*);
j = j + 1, {n, 3}], {i, 8, ii, 4}] (*TC,werte1,werte1/Molges1,*)
```


Ergebnis

```
ExportTabelle = Flatten[Table[tabexp[k], {k, z}], 1];
(* Formatierung der Tabelle für Export *)
Export["\\Export data-Mathematica.xlsx", ExportTabelle]
```

D: Matlab program script (DI Martin Peham)

```
%% Fehlerrechnung Datenauswertung

clear all;
close all;

%% Fehlerrechnung Inputströme:
% Methanisierung:
uLimitCH4 = 10; %Nl/min
uLimitCO2 = 10; %Nl/min
uLimitCO = 10; %Nl/min
uLimitH2O = 0; %Nl/min
uLimitH2 = 40; %Nl/min
uLimitN2 = 50; %Nl/min

dyn = 1/187.5; % Dynamik

% Unteres Limit
lLimitCH4 = uLimitCH4*dyn; %Nl/min
lLimitH2O = uLimitH2O*dyn; %Nl/min
lLimitH2 = uLimitH2*dyn; %Nl/min
lLimitCO2 = uLimitCO2*dyn; %Nl/min
lLimitN2 = uLimitN2*dyn; %Nl/min
lLimitCO = uLimitCO*dyn; %Nl/min

%% Fehlerrechnung Gasanalytik:

% Fehler in der Mischung:
NVdot = 16.7; %Nl/min
xCH4 = 0.0; %
xCO = 0.157;
xCO2 = 0.066;
xH2O= 0.0;
xH2 = 0.705;
xN2 = 0.07;

nin = NVdot/60/22.4; %mol/s

NVdotCH4 = NVdot*xCH4; %Nl/min
NVdotH2O = NVdot*xH2O; %Nl/min
NVdotH2 = NVdot*xH2; %Nl/min
NVdotN2 = NVdot*xN2; %Nl/min
NVdotCO = NVdot*xCO; %Nl/min
NVdotCO2 = NVdot*xCO2; %Nl/min

if NVdotCH4 == 0;
    u_CH4 = 0; %Nl/min
else
    u_CH4 = NVdotCH4*0.005+uLimitCH4*0.001; %Nl/min
end

if NVdotH2O == 0;
    u_H2O = 0; %Nl/min
else
    u_H2O = NVdotH2O*0.005+uLimitH2O*0.001; %Nl/min
end
```

```
if NVdotH2 == 0;
    u_H2 = 0; %Nl/min
else
    u_H2 = NVdotH2*0.005+uLimitH2*0.001; %Nl/min
end

if NVdotCO == 0;
    u_CO = 0; %Nl/min
else
    u_CO = NVdotCO*0.005+uLimitCO*0.001; %Nl/min
end

if NVdotCO2 == 0;
    u_CO2 = 0; %Nl/min
else
    u_CO2 = NVdotCO2*0.005+uLimitCO2*0.001; %Nl/min
end

if NVdotN2 == 0;
    u_N2 = 0; %Nl/min
else
    u_N2 = NVdotN2*0.005+uLimitN2*0.001; %Nl/min
end


us = [u_CH4 u_CO u_CO2 u_H2O u_H2 u_N2;
    u_CO u_CO2 u_H2O u_H2 u_N2 u_CH4;
    u_CO2 u_H2O u_H2 u_N2 u_CH4 u_CO;
    u_H2O u_H2 u_N2 u_CH4 u_CO u_CO2;
    u_H2 u_N2 u_CH4 u_CO u_CO2 u_H2O;
    u_N2 u_CH4 u_CO u_CO2 u_H2O u_H2;
    u_N2 u_CH4 u_CO u_CO2 u_H2O u_H2];

epsilon_CH4 = u_CH4/NVdotCH4; %%
epsilon_H2O = u_H2O/NVdotH2O; %%
epsilon_H2 = u_H2/NVdotH2; %%
epsilon_CO = u_CO/NVdotCO; %%
epsilon_CO2 = u_CO2/NVdotCO2; %%
epsilon_N2 = u_N2/NVdotN2; %%

% Gaußsche Fehlerfortpflanzung für die Anteile:
NVdots = [NVdotCH4 NVdotCO NVdotCO2 NVdotH2O NVdotH2 NVdotN2;
    NVdotCO NVdotCO2 NVdotH2O NVdotH2 NVdotN2 NVdotCH4;
    NVdotCO2 NVdotH2O NVdotH2 NVdotN2 NVdotCH4 NVdotCO;
    NVdotH2O NVdotH2 NVdotN2 NVdotCH4 NVdotCO NVdotCO2;
    NVdotH2 NVdotN2 NVdotCH4 NVdotCO NVdotCO2 NVdotH2O;
    NVdotN2 NVdotCH4 NVdotCO NVdotCO2 NVdotH2O NVdotH2];
uxs = zeros(6,1);
syms fFraction(x1,x2,x3,x4,x5,x6)
fFraction(x1,x2,x3,x4,x5,x6) = x1/(x1+x2+x3+x4+x5+x6);
dFractiondx1 = diff(fFraction,x1);
dFractiondx2 = diff(fFraction,x2);
dFractiondx3 = diff(fFraction,x3);
dFractiondx4 = diff(fFraction,x4);
```

```
dFractiondx5 = diff(fFraction,x5);
dFractiondx6 = diff(fFraction,x6);

for i=1:6
    x1 = NVdots(i,1);
    x2 = NVdots(i,2);
    x3 = NVdots(i,3);
    x4 = NVdots(i,4);
    x5 = NVdots(i,5);
    x6 = NVdots(i,6);
    dFractiondx1eval = double(subs(dFractiondx1));
    dFractiondx2eval = double(subs(dFractiondx2));
    dFractiondx3eval = double(subs(dFractiondx3));
    dFractiondx4eval = double(subs(dFractiondx4));
    dFractiondx5eval = double(subs(dFractiondx5));
    dFractiondx6eval = double(subs(dFractiondx6));
  uxs(i) = sqrt(dFractiondx1eval^2*us(i,1)^2+dFractiondx2eval^2*us(i,2)^2+
       dFractiondx3eval^2*us(i,3)^2+dFractiondx4eval^2*us(i,4)^2+ ...
       dFractiondx5eval^2*us(i,5)^2+dFractiondx6eval^2*us(i,6)^2);
end

% Absolute Fehler der Gasanalytik
uxCH4Dry = 0.005;
uxH2Dry = 0.005;
uxCODry = 0.005;
uxCO2Dry = 0.005;

%% Fehlerrechnungstickstoff
syms sxCH4Dry sxH2Dry sxCODry sxCO2Dry sxN2Dry
sxN2Dry = 1 - (sxCH4Dry+sxH2Dry+sxCODry+sxCO2Dry);
dGN2 = gradient(sxN2Dry);
uxN2Dry = double(sqrt(dGN2(1)^2*uxCH4Dry^2+dGN2(2)^2*uxCO2Dry^2+dGN2(3)↙
^2*uxCODry^2+dGN2(4)^2*uxH2Dry^2));

% Gleichungssystem aufstellen und lösen
% nin = 1; %mol/s
% xCH4Dry = 0.305;
% xH2Dry = 0.267;
% xCODry = 0.013;
% xCO2Dry = 0.062;
% xN2Dry = 0.353;
%
% xCH4in = 0.0;
% xH2in = 0;
% xCOin = 0;
% xCO2in = 0;
% xN2in = 0;
% xH2Oin = 0;

syms xCH4out xH2out xCOout xCO2out xH2Oout xN2out
syms nout nC
syms xCH4Dry xH2Dry xCODry xCO2Dry xN2Dry
syms xCH4in xH2in xCOin xCO2in xH2Oin xN2in
syms nin
```

```
G1 = xCH4out == xCH4Dry * (1 - xH2Oout);
G2 = xH2out == xH2Dry * (1 - xH2Oout);
G3 = xCOout == xCODry * (1 - xH2Oout);
G4 = xCO2out == xCO2Dry * (1 - xH2Oout);
G5 = xN2out == xN2Dry * (1 - xH2Oout);

SumOut = xCH4out + xH2out + xCOout + xCO2out + xH2Oout + xN2out == 1;

HBil = nin * (xH2in*2 + xCH4in*4  + xH2Oin*2) == nout * (xH2out*2 + xCH4out*4  +↙
xH2Oout*2);
CBil = nin * (xCOin + xCO2in + xCH4in) == nout * (xCOout + xCO2out + xCH4out) + nC;
OBil = nin * (xCOin + xCO2in*2 + xH2Oin) == nout * (xCOout + xCO2out*2 + xH2Oout);

[xCH4out, xH2out, xCOout, xCO2out, xH2Oout, xN2out, nout, nC] = solve([G1, G2, G3, G4,↙
G5, HBil, CBil, OBil], [xCH4out xH2out xCOout xCO2out xH2Oout xN2out nout nC]);

ctrlxsumout = xCH4out+xH2out+xCOout+xCO2out+xH2Oout;

fxCH4out = xCH4out % xCH4Dry xCH4in xCOin xCO2in xCODry xCO2Dry xH2Oin
fxH2out = xH2out;
fxCOout = xCOout;
fxH2Oout = xH2Oout;
fxCO2out = xCO2out;
fxN2out = xN2out;

dfxH2out1 = diff(fxH2out, xCH4Dry);
dfxH2out2 = diff(fxH2out, xCH4in);
dfxH2out3 = diff(fxH2out, xCODry);
dfxH2out4 = diff(fxH2out, xCOin);
dfxH2out5 = diff(fxH2out, xCO2Dry);
dfxH2out6 = diff(fxH2out, xCO2in);
dfxH2out7 = diff(fxH2out, xH2Dry);
dfxH2out8 = diff(fxH2out, xH2in);
dfxH2out9 = diff(fxH2out, xN2Dry);
dfxH2out10 = diff(fxH2out, xN2in);
dfxH2out11 = diff(fxH2out, xH2Oin);
dfxH2out12 = diff(fxH2out, nin);

dfxCH4out1 = diff(fxCH4out, xCH4Dry);
dfxCH4out2 = diff(fxCH4out, xCH4in);
dfxCH4out3 = diff(fxCH4out, xCODry);
dfxCH4out4 = diff(fxCH4out, xCOin);
dfxCH4out5 = diff(fxCH4out, xCO2Dry);
dfxCH4out6 = diff(fxCH4out, xCO2in);
dfxCH4out7 = diff(fxCH4out, xH2Dry);
dfxCH4out8 = diff(fxCH4out, xH2in);
dfxCH4out9 = diff(fxCH4out, xN2Dry);
dfxCH4out10 = diff(fxCH4out, xN2in);
dfxCH4out11 = diff(fxCH4out, xH2Oin);
dfxCH4out12 = diff(fxCH4out, nin);

dfxH2Oout1 = diff(fxH2Oout, xCH4Dry);
dfxH2Oout2 = diff(fxH2Oout, xCH4in);
dfxH2Oout3 = diff(fxH2Oout, xCODry);
dfxH2Oout4 = diff(fxH2Oout, xCOin);
```

```
dfxH2Oout5 = diff(fxH2Oout, xCO2Dry);
dfxH2Oout6 = diff(fxH2Oout, xCO2in);
dfxH2Oout7 = diff(fxH2Oout, xH2Dry);
dfxH2Oout8 = diff(fxH2Oout, xH2in);
dfxH2Oout9 = diff(fxH2Oout, xN2Dry);
dfxH2Oout10 = diff(fxH2Oout, xN2in);
dfxH2Oout11 = diff(fxH2Oout, xH2Oin);
dfxH2Oout12 = diff(fxH2Oout, nin);

dfxCOout1 = diff(fxCOout, xCH4Dry);
dfxCOout2 = diff(fxCOout, xCH4in);
dfxCOout3 = diff(fxCOout, xCODry);
dfxCOout4 = diff(fxCOout, xCOin);
dfxCOout5 = diff(fxCOout, xCO2Dry);
dfxCOout6 = diff(fxCOout, xCO2in);
dfxCOout7 = diff(fxCOout, xH2Dry);
dfxCOout8 = diff(fxCOout, xH2in);
dfxCOout9 = diff(fxCOout, xN2Dry);
dfxCOout10 = diff(fxCOout, xN2in);
dfxCOout11 = diff(fxCOout, xH2Oin);
dfxCOout12 = diff(fxCOout, nin);

dfxCO2out1 = diff(fxCO2out, xCH4Dry);
dfxCO2out2 = diff(fxCO2out, xCH4in);
dfxCO2out3 = diff(fxCO2out, xCODry);
dfxCO2out4 = diff(fxCO2out, xCOin);
dfxCO2out5 = diff(fxCO2out, xCO2Dry);
dfxCO2out6 = diff(fxCO2out, xCO2in);
dfxCO2out7 = diff(fxCO2out, xH2Dry);
dfxCO2out8 = diff(fxCO2out, xH2in);
dfxCO2out9 = diff(fxCO2out, xN2Dry);
dfxCO2out10 = diff(fxCO2out, xN2in);
dfxCO2out11 = diff(fxCO2out, xH2Oin);
dfxCO2out12 = diff(fxCO2out, nin);

dfxN2out1 = diff(fxN2out, xCH4Dry);
dfxN2out2 = diff(fxN2out, xCH4in);
dfxN2out3 = diff(fxN2out, xCODry);
dfxN2out4 = diff(fxN2out, xCOin);
dfxN2out5 = diff(fxN2out, xCO2Dry);
dfxN2out6 = diff(fxN2out, xCO2in);
dfxN2out7 = diff(fxN2out, xH2Dry);
dfxN2out8 = diff(fxN2out, xH2in);
dfxN2out9 = diff(fxN2out, xN2Dry);
dfxN2out10 = diff(fxN2out, xN2in);
dfxN2out11 = diff(fxN2out, xH2Oin);
dfxN2out12 = diff(fxN2out, nin);

%COx-Umsatz
COxUmsatz = ((nin*(xCO2in + xCOin + xCH4in) - nout*(xCO2out + xCOout))/(nin*(xCO2in +↙
xCOin + xCH4in)));
fCOxUmsatz = COxUmsatz;
dfCOxUmsatz1 = diff(fCOxUmsatz, xCH4Dry);
dfCOxUmsatz2 = diff(fCOxUmsatz, xCH4in);
dfCOxUmsatz3 = diff(fCOxUmsatz, xCODry);
dfCOxUmsatz4 = diff(fCOxUmsatz, xCOin);
dfCOxUmsatz5 = diff(fCOxUmsatz, xCO2Dry);
dfCOxUmsatz6 = diff(fCOxUmsatz, xCO2in);
dfCOxUmsatz7 = diff(fCOxUmsatz, xH2Dry);
dfCOxUmsatz8 = diff(fCOxUmsatz, xH2in);
dfCOxUmsatz9 = diff(fCOxUmsatz, xN2Dry);
dfCOxUmsatz10 = diff(fCOxUmsatz, xN2in);
dfCOxUmsatz11 = diff(fCOxUmsatz, xH2Oin);
dfCOxUmsatz12 = diff(fCOxUmsatz, nin);

nin = NVdot/60/22.4; %mol/s
xCH4Dry = 0.682;
xH2Dry = 0.08;
xCODry = 0.0;
xCO2Dry = 0.017;
xN2Dry = 0.221;

xCH4in = xCH4;
xH2in = xH2;
xCOin = xCO;
xCO2in = xCO2;
xN2in = xN2;
xH2Oin = xH2O;

uxCH4in = uxs(1);
uxCOin = uxs(2);
uxCO2in = uxs(3);
uxH2in = uxs(4);
uxH2Oin = uxs(5);
uxN2in = uxs(6);
unin = sqrt(us(1)^2+us(2)^2+us(3)^2+us(4)^2+us(5)^2+us(6)^2)/60/22.4; %mol/s

% dfxCH4eval1 = double(subs(dfxCH4out(1)));
% dfxCHeval2 = double(subs(dfxCH4out(2)));
% dfxCH4eval3 = double(subs(dfxCH4out(3)));
% dfxCH4eval4 = double(subs(dfxCH4out(4)));
% dfxCH4eval5 = double(subs(dfxCH4out(5)));
% dfxCH4eval6 = double(subs(dfxCH4out(6)));
% dfxCH4eval7 = double(subs(dfxCH4out(7)));

uxH2out = double(subs(sqrt↙
(dfxH2out1^2*uxCH4Dry^2+dfxH2out2^2*uxCH4in^2+dfxH2out3^2*uxCODry^2+...
    dfxH2out4^2*uxCOin^2+dfxH2out5^2*uxCO2Dry^2+dfxH2out6^2*uxCO2in^2+...
    dfxH2out7^2*uxH2Dry^2+dfxH2out8^2*uxH2in^2+dfxH2out9^2*uxN2Dry^2+...
    +dfxH2out10^2*uxN2in^2+dfxH2out11^2*uxH2Oin^2+dfxH2out12^2*unin^2)));

uxCH4out = double(subs(sqrt↙
(dfxCH4out1^2*uxCH4Dry^2+dfxCH4out2^2*uxCH4in^2+dfxCH4out3^2*uxCODry^2+...
    dfxCH4out4^2*uxCOin^2+dfxCH4out5^2*uxCO2Dry^2+dfxCH4out6^2*uxCO2in^2+...
    dfxCH4out7^2*uxH2Dry^2+dfxCH4out8^2*uxH2in^2+dfxCH4out9^2*uxN2Dry^2+...
    +dfxCH4out10^2*uxN2in^2+dfxCH4out11^2*uxH2Oin^2+dfxCH4out12^2*unin^2)));

uxH2Oout = double(subs(sqrt↙
(dfxH2Oout1^2*uxCH4Dry^2+dfxH2Oout2^2*uxCH4in^2+dfxH2Oout3^2*uxCODry^2+...
    dfxH2Oout4^2*uxCOin^2+dfxH2Oout5^2*uxCO2Dry^2+dfxH2Oout6^2*uxCO2in^2+...
```

```
    dfxH2Oout7^2*uxH2Dry^2+dfxH2Oout8^2*uxH2in^2+dfxH2Oout9^2*uxN2Dry^2+...
    +dfxH2Oout10^2*uxN2in^2+dfxH2Oout11^2*uxH2Oin^2+dfxH2Oout12^2*unin^2)));

uxCOout = double(subs(sqrt(
(dfxCOout1^2*uxCH4Dry^2+dfxCOout2^2*uxCH4in^2+dfxCOout3^2*uxCODry^2+...
    dfxCOout4^2*uxCOin^2+dfxCOout5^2*uxCO2Dry^2+dfxCOout6^2*uxCO2in^2+...
    dfxCOout7^2*uxH2Dry^2+dfxCOout8^2*uxH2in^2+dfxCOout9^2*uxN2Dry^2+...
    +dfxCOout10^2*uxN2in^2+dfxCOout11^2*uxH2Oin^2+dfxCOout12^2*unin^2)));

uxCO2out = double(subs(sqrt(
(dfxCO2out1^2*uxCH4Dry^2+dfxCO2out2^2*uxCH4in^2+dfxCO2out3^2*uxCODry^2+...
    dfxCO2out4^2*uxCOin^2+dfxCO2out5^2*uxCO2Dry^2+dfxCO2out6^2*uxCO2in^2+...
    dfxCO2out7^2*uxH2Dry^2+dfxCO2out8^2*uxH2in^2+dfxCO2out9^2*uxN2Dry^2+...
    +dfxCO2out10^2*uxN2in^2+dfxCO2out11^2*uxH2Oin^2+dfxCO2out12^2*unin^2)));

uxN2out = double(subs(sqrt(
(dfxN2out1^2*uxCH4Dry^2+dfxN2out2^2*uxCH4in^2+dfxN2out3^2*uxCODry^2+...
    dfxN2out4^2*uxCOin^2+dfxN2out5^2*uxCO2Dry^2+dfxN2out6^2*uxCO2in^2+...
    dfxN2out7^2*uxH2Dry^2+dfxN2out8^2*uxH2in^2+dfxN2out9^2*uxN2Dry^2+...
    +dfxN2out10^2*uxN2in^2+dfxN2out11^2*uxH2Oin^2+dfxN2out12^2*unin^2)));

uCOxUmsatz = double(subs(sqrt(
(dfCOxUmsatz1^2*uxCH4Dry^2+dfCOxUmsatz2^2*uxCH4in^2+dfCOxUmsatz3^2*uxCODry^2+...
    dfCOxUmsatz4^2*uxCOin^2+dfCOxUmsatz5^2*uxCO2Dry^2+dfCOxUmsatz6^2*uxCO2in^2+...
    dfCOxUmsatz7^2*uxH2Dry^2+dfCOxUmsatz8^2*uxH2in^2+dfCOxUmsatz9^2*uxN2Dry^2+...
    +dfCOxUmsatz10^2*uxN2in^2+dfCOxUmsatz11^2*uxH2Oin^2+dfCOxUmsatz12^2*unin^2)));

xCH4out = double(subs(xCH4out));
xH2out = double(subs(xH2out));
xCOout = double(subs(xCOout));
xCO2out = double(subs(xCO2out));
xH2Oout = double(subs(xH2Oout));
xN2out = double(subs(xN2out));
nout = double(subs(nout));
nC = double(subs(nC));
COxUmsatz = double(subs(COxUmsatz));
ctrlxsumout = double(subs(ctrlxsumout));

% Plotten der Anteile mit Standardabweichung
figure;
hold on
bar(1,xCH4out);
bar(2,xCOout);
bar(3,xCO2out);
bar(4,xH2Oout);
bar(5,xH2out);
bar(6,xN2out);
% errorbar(X,Y,E);
% er.Color = [0 0 0];
% er.LineStyle = 'none';
er1 = errorbar(1,xCH4out,uxCH4out);
er1.Color = [0 0 0];
% er12 = errorbar(1,xCH4,uxs2sigma(1));
% er12.Color = [1 0 0];
er2 = errorbar(2,xCOout,uxCOout);
```

```
er2.Color = [0 0 0];
% er22 = errorbar(2,xCO,uxs2sigma(2));
% er22.Color = [1 0 0];
er3 = errorbar(3,xCO2out,uxCO2out);
er3.Color = [0 0 0];
% er32 = errorbar(3,xCO2,uxs2sigma(3));
% er32.Color = [1 0 0];
er4 = errorbar(4,xH2Oout,uxH2Oout);
er4.Color = [0 0 0];
% er42 = errorbar(4,xH2O,uxs2sigma(4));
% er42.Color = [1 0 0];
er5 = errorbar(5,xH2out,uxH2out);
er5.Color = [0 0 0];
% er52 = errorbar(5,xH2,uxs2sigma(5));
% er52.Color = [1 0 0];
er6 = errorbar(6,xN2out,uxN2out);
er6.Color = [0 0 0];
% er72 = errorbar(7,xN2,uxs2sigma(7));
% er72.Color = [1 0 0];
legend('CH4','CO','CO2','H2O','H2','N2','\sigma-CH4','\sigma-CO','\sigma-CO2','\sigma-
H2O','\sigma-H2','\sigma-N2');

%% COx-Umsatz
COxUmsatz = ((nin*(xCO2in + xCOin + xCH4in) - nout*(xCO2out + xCOout))/(nin*(xCO2in +
xCOin + xCH4in)));
```